2.32 Fe is Translocated directly from DC or/and Roots to the Youngest Leaf via Phloem in Graminaceous Plants

T. Tsukamoto*, H. Nakanishi*, H. Uchida**, S. Watanabe***,
N. S. Ishioka***, S. Fujimaki***, K. Sakamoto***,
S. Matsuhashi***, T. Sekine***, T. Kume***, K. Arakawa***,
N. K. Nishizawa* and S. Mori*
Faculty of Agricultural and Life Sciences, The University of Tokyo*,
Central Research Laboratory, Hamamatsu Photonics K.K. **,
Department of Ion-Beam-applied Biology, JAERI***

1. Introduction

Iron (Fe) is required for many functions in plants, including heme and chlorophyll biosynthesis, photosynthesis, and as a component of Fe-S cluster containing enzymes. Although abundant in soils, Fe forms highly insoluble ferric-hydroxide precipitates under oxidative or alkaline conditions that limit its availability for plants. Therefore, plants have evolved the mechanism to solubilize and efficiently take up soil-Fe. Graminaceous plants release mugineic acid family phytosiderophores (MAs) into the rhizosphere that bind Fe(III) ion and taken up into the roots. Then, Fe has been thought to be translocated to the shoot via xylem stream driven by transpiration and root pressure, and then unloaded to the leaf cells. However, the precise mechanism of Fe translocation in the intact plants is still unclear.

Last year, we showed that Fe is translocated to the youngest leaf without transpiration stream. The fact suggested that Fe might be translocated to the youngest leaf via phloem. In this study, we compared the real time ^{52}Fe translocation in the intact barley plants by a Positron-Emitting Tracer Imaging System (PETIS) after blocking phloem transport in the leaves by heating the leaf tissue.

2. Materials and methods

2.1 Plant material and culture conditions

Barley (*Hordeum vulgare* L. cv. Ehimehadaka no.1) seeds were germinated at room temperature (ca 24°C) on paper towels soaked with distilled water. After germination, the plantlets were transferred to a plastic net floating on water in a growth chamber under a mixture of incandescent and fluorescent lamps with a 14 h light (20 °C)/10 h dark (15 °C) regime and a photon flux density of 320 μmol m^{-2} s^{-1}. After two days, the plants were transferred to modified Kasugai's medium: 0.7 mM K_2SO_4, 0.1 mM KCl, 0.1 mM KH_2PO_4, 2.0 mM $Ca(NO_3)_2$, 0.5 mM $MgSO_4$, 10 μM H_3BO_3, 0.5 μM $MnSO_4$, 0.2 μM $CuSO_4$, 0.5 μM $ZnSO_4$, 0.01 μM $(NH_4)Mo_6O_{24}$, 0.1 μM Fe-EDTA. The pH was adjusted daily to 5.5 with 1 N HCl or NaOH, and the nutrient solution was renewed once a week. For Fe deficiency, the plants were transferred to the culture solution without Fe one week before the beginning of the PETIS experiments. The absorption experiments were performed at about 3 weeks after germination.

2.2 Production of ^{52}Fe

^{52}Fe (half life: 8.27 h) was produced by the ^{52}Cr(α, 4n)^{52}Fe reaction by bombarding a 1.5 mm thick Cr foil (natural isotopic

composition, 99.9% purity, Goodfellow Metals Ltd.) with a 100-MeV α beam from the TIARA AVF cyclotron. Using a beam current of 3 μA for 2 hours, about 1 MBq of ^{52}Fe was produced. The radiochemical separation of the ^{52}Fe from the target was carried out with a method described by Watanabe et al. (2002)[1]. After pH adjustment of the $^{52}Fe^{3+}$ solution without cold Fe to about pH 3 with 1 M KOH, the $^{52}Fe^{3+}$ was chelated with 197.4 μmol of deoxymugineic acid (DMA) in the dark for one hour.

2.3 Experimental setting up

^{11}C-photoassimilates by heat-girdling

A part of the second youngest leaf of a barley plant was heated by hot steam generated by a soldering iron ("heat-girdling"). The heated regions were about 1 cm long. Another barely plant was not treated. $^{11}CO_2$ (50 MBq) was supplied from the second youngest leaves of barley plants for 5 min. After 90 min of PETIS analysis, BAS image analysis was performed (Fig1).

^{52}Fe Translocation from the roots to the leaf

A part of the expanded leaf (3-leaf) and the youngest leaf (4-leaf) of Fe deficient barley were treated with heat as previously described. Another Fe-deficient barely plant was not treated. $^{52}Fe^{3+}$-deoxymugineic acid (DMA) (0.28 MBq, 19.9 fmol) was supplied from roots of both plants. After 4 h absorption, BAS image analysis was performed. The upper portion and the lower portion from the heated area of the youngest leaf and the expanded leaf were analyzed for absolute amount of radioactivity by Gamma-ray spectrometry.

3. Results and discussion

To examine the effects of phloem transport on Fe translocation, we selectively blocked phloem transport in leaf by "heat-girdling". In the untreated plant, ^{11}C-photoassimilates were translocated from the leaf to leaf sheaths, roots, and the youngest leaves (Fig. 1B). However, ^{11}C-photoassimilates were not translocated to any where from the treated leaf (Fig. 1A). This result clearly shows that heat-girdling effectively inhibit phloem transport in the leaf.

In the untreated plant, ^{52}Fe was translocated to all parts of the plant (Fig. 2B). ^{52}Fe translocation to the upper regions of the youngest leaf was severely suppressed in the treated plant, whereas it was not affected in the expanded leaf (Fig. 2A). In the youngest leaf (4th-leaf), the ^{52}Fe ratio of the upper portion and the lower portion was suppressed to about 25 % by heat-girdling (Fig. 2C). However, the ratio was unaffected in the expanded leaf (3th-leaf). In addition, translocation to the 2th-leaf was also unaffected by heat-girdling (data not shown). These results demonstrated that Fe is translocated to the youngest leaf mainly via phloem and partly via xylem, but to the older leaves via xylem.

Zhang et al. (1995)[2] reported that Fe may be translocated to the apex via phloem only after remobilization from older leaves in French bean. However, in our experiment, ^{52}Fe has arrived at the youngest leaf of Fe deficient barley only 45 min after supplying $^{52}Fe^{3+}$-DMA to the roots. 45 min is too short for ^{52}Fe to be translocated from older leaves to the youngest leaf. Therefore, Fe may be transferred from xylem to phloem in DC(discrimination center) or/and roots, but not in the leaves. We reported that DC may play an important role in the regulation of

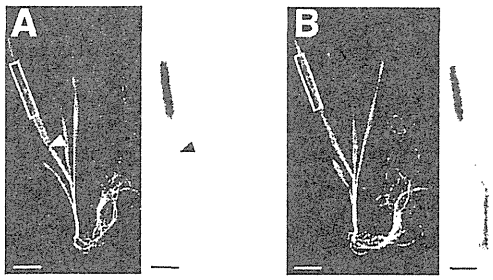

Figure 1. BAS images of ^{11}C-photoassimilate translocation from the part of the second youngest leaf (square) in barley treated with heat-girdling (arrowhead) (A) and the untreated plant (B). Bar = 4 cm.

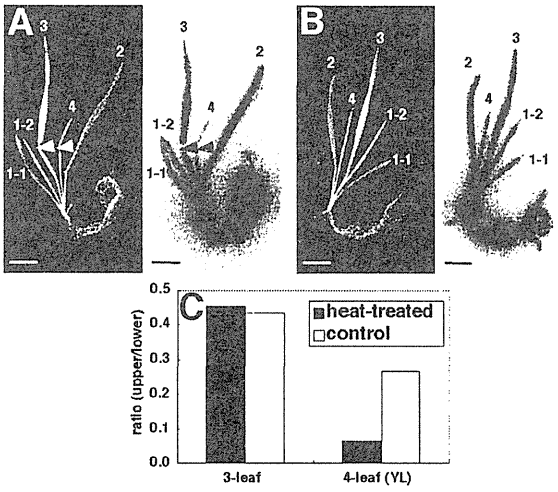

Figure 2. Effect of heat-girdling on ^{52}Fe translocation from the roots to the shoots in Fe-deficient barley. BAS image of the ^{52}Fe translocation in Fe-deficient barley treated with heat-girdling (arrowhead) (A) and the untreated plant (B). Bar = 4 cm. C, The ratio of the ^{52}Fe concentration of the upper region to the lower region.

distribution of minerals and metabolites in graminaceous plants [3)-7)].

Based on the above results we propose a novel model as shown in Fig. 3. a) Fe^{3+}-MAs is absorbed from the Fe^{3+}-MAs transporter 'YS1'. b) Fe is translocated via xylem to the older leaves. c) Fe is directly transferred from xylem to phloem mainly in DC or/and roots, then, translocated mainly via phloem and partly via xylem to the

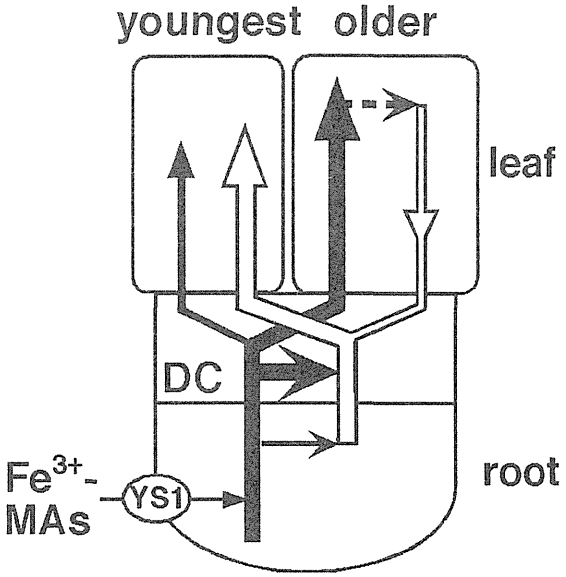

Figure 3. A schematic model of direct phloem transport of Fe from the DC or/and the roots to the sink tissue in barley. Black arrow indicates xylem transport, and white arrow indicates phloem transport.

youngest leaf. When Fe depletion in a plant body is perceived by the plant, Fe may be retranslocated from older leaves to the youngest leaf via phloem after remobilization from older leaves.

References

1) S. Watanabe et al., *Radiochimica Acta* 89: 853-858 (2001)
2) C. Zhang et al., *J. Plant Nutr.* 18: 2049-2058
3) S. Kiyomiya et al., *Physiologia Plantarum* 13: 359-367 (2001)
4) H. Nakanishi et al., *J. Exp. Bot.* 50: 637-643(1999)
5) S. Kiyomiya et al., *Plant Physiology* 125: 1743-1753(2001)
6) S. Mori et al., *Soil Sci. Plant Nutr.* 46:975-979(2000)
7) H Nakanishi et al., *Soil Sci. Plant Nutr.* 48: 759-762(2002)

2.33 Retention of Cd at the Leaf Sheathes and Nodes after Absorption by Rice Plants Detected by using ^{105}Cd and ^{107}Cd as a Tracer

H. Hayashi*, N. Suzui*, N.S. Ishioka**, S. Fujimaki**, K. Sakamoto**
T. Watanabe**, S. Matsuhashi**, K. Arakawa** and T. Kume**
Department of Applied Biological Chemistry, Univ. Tokyo*,
Department of Ion-Beam-Applied Biology, JAERI**

1. Introduction

Cadmium (Cd) is the heavy metal which is accumulated in rice grain. Now the big discussions concerning the reduction of maximum level of Cd in rice grain is on going, which may cause difficulty in cultivating rice in some area of Japan.

Cd is thought to be transported to grains through sieve tubes when rice plants grew on Cd contaminated soils and absorbed Cd[1]. To understand the mechanisms of internal translocation of Cd in rice plants may offer a way to reduce Cd accumulation in grains.

To know the distribution of Cd in rice plants after absorption, we have established the experiments for detailed analysis of Cd transport by a positron-emitting tracer imaging system (PETIS) and BAS system. We produced ^{105}Cd and ^{107}Cd for the application to rice roots and the detection of Cd transport in rice plants.

2. Experiments

Rice plants (*Oryza sativa* L. var. Kantou) were grown in a complete nutrient solution for a month. The plants at 9th-leaf stage were used for the experiments. Cd was applied to rice roots at the concentration of 1μM in the nutrient solution for 1 day before experiments.

^{105}Cd ($^{107}Ag(p,3n)^{105}Cd$; 9.37 MBq) and ^{107}Cd ($^{109}Ag(p,3n)^{107}Cd$; 224 MBq) was applied to the nutrient solution for absorption by roots. Cd distribution to shoots was detected by PETIS for 18 hrs, followed by BAS after separation of plant body into each leaf.

3. Results and discussion

Figure1-B and C show the PETIS images of the translocation of ^{105}Cd+^{107}Cd after 12 hrs absorption and the accumulation patterns Cd of each part of leaves labeled on figure1-B, respectively. The absorbed Cd was distributed only to old leaves not to the leaves which transpire actively. Accumulation of Cd at the lower part of leaves started at two hours after application, and increased gradually.

To know the position of Cd accumulation in leaves, rice plant after absorption were separated into each leaf and Cd accumulation was detected by BAS (figure 2 A). Cd was accumulated at the basal part of each leaf sheath and not transported to leaf blade, irrespective of leaf age. Growing point and nodes (arrow) showed the heaviest accumulation.

We recently analyzed the Cd concentrations in both xylem exudate and phloem sap of rice plants treated with 10 and 100 μM Cd for 3days. From analysis of both phloem sap and xylem exudates, Cd concentration in the phloem sap

was significantly lower than that in the xylem exudates, indicating that Cd is not concentrated during the transfer from xylem to phloem (Tanaka et al. 2003). Our present results is consistent with the analysis of sap above, namely that the Cd transported through xylem vessels are thought to be precipitated at the lower part of leaf sheath and nodes, and lower concentration of Cd in xylem vessels are moved to leaf blade where Cd may be transferred to phloem. Alternatively, Cd after precipitated at the lower part of leaf sheath and node directly move to phloem there. In rice plants, most of Cd absorbed from roots was accumulated in root and only small parts of Cd in roots were transported to shoots, indicating the existence of a barrier between root and shoot. In shoots, Cd translocation was inhibited at the lower part of leaf blade and the nodes, suggesting that these parts are also barriers for the translocation of Cd, possibly for xylem to phloem transport.

References

1) Tanaka K, et al. Soil Sci. Plant Nutr. 49:311-313(2003)

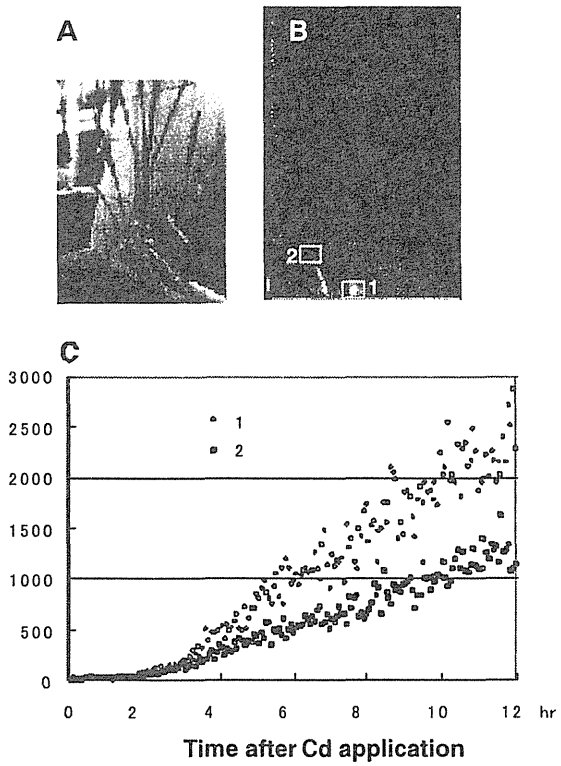

Figure1 Cd accumulation in rice plant
A: Picture of rice plant set in PETIS system.
B: PETIS image of 105+107Cd accumulation after 12 hrs absorption. C: Cd accumumulation at positions of 1 and 2 marked in B

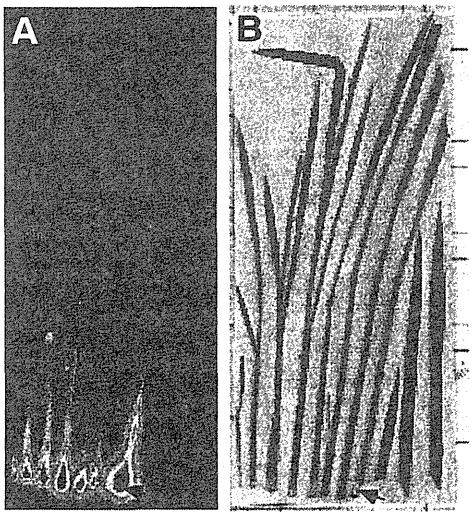

Figure2 Cd accumulation in rice plant detected by BAS
A:BAS image of Cd accumulation after 12 hrs absorption and separation of plant body. B:Picture of plant body separated into each leaf which absorbed Cd tracers for BAS. Nodes and growing point are indicated by arrow.

2.34 Ammonium Uptake and Assimilation in Rice

J. Yamaguchi*, Y. Sonoda*, A. Iwata*, A. Ikeda*, T. Tsutsui*,
C. Morita-Yamamuro*, S.-G. Yao, S. Matsuhashi**, S. Fujimaki**,
K. Sakamoto**, K. Arakawa** and T. Kume**
Division of Biological Sciences, Graduate School of Science, Hokkaido University*
Department of Ion-Beam-Applied Biology, JAERI**

1. Introduction

More than 70% of the world's rice is produced in intensively cultivated, irrigated paddy fields. In flooded paddy fields, the bulk of the soil is hypoxic or anaerobic and the major form of nitrogen available to plants is ammonium. Rice plants evolutionally acquired the ability to be resistant to these conditions[1]. This is in marked contrast to most well-aerated agricultural soils in which nitrate is the predominant inorganic nitrogen species. Ammonium is the preferred nitrogen species taken up by rice and it is superior to nitrate in terms of fertilizer efficiency in paddy fields[2]. It has been demonstrated that influx of ammonium into rice roots gradually increased between $2x10^{-6}$ and $1x10^{-3}$ M external ammonium[3], indicating that rice plants may acclimate to the external ammonium supply by altering properties of their ammonium transport systems.

To study the regulation of ammonium uptake into rice roots, three ammonium transporter genes (*OsAMT1;1*, *1;2* and *1;3*; *Oryza sativa ammonium transporter*) were isolated and examined[4,5]. OsAMT1s belong to AMT1 family, containing 11 putative transmembrane-spanning domains. Southern blot analysis and screening of the rice genome database confirmed that with *OsAMT1;1-1;3* the complete AMT1 family of rice had been isolated. Heterologous expression of *OsAMT1s* in the yeast *Saccharomyces cerevisiae* mutant 31019b showed that all three OsAMT1s exhibit ammonium transport activity. Northern blot analysis showed a distinct expression in shoots and roots for *OsAMT1;1*, root-specific and ammonium-inducible expression for *OsAMT1;2*, and root-specific and nitrogen-derepressible expression for *OsAMT1;3*.

Real time monitoring of ammonium translocation in rice by PETIS (positron emitting tracer imaging system) demonstrated an active uptake and movement of ammonium[6]. Here we show the attempt of real time monitoring of ammonium translocation using rice for wild-type and transgenic plant constitutively expressing *OsAMT1;2* gene.

2. Experimental procedures

2.1 Transgenic Rice

The 35S promoter of cauliflower mosaic virus (CaMV) from pBI221 was connected with ORF of *OsAMT1;2* cDNA. Rice was transformed by the procedure described by Hiei et al.[7]. Transformants of rice were grown in greenhouse. Hygromycin resistance of rice seedlings was assayed and screened. Homozygous plants for the transgene were used in the experiments.

2.2 Plant Materials and Growth Conditions

Rice (*Oryza sativa* L) seeds were sterilized and then thoroughly rinsed in water. Seedlings were grown hydroponically first in tap water for a week, and then in nitrogen-free nutrient solution, which is described in the reference[5].

2.3 $^{13}NH_4^+$ Synthesis

The radiotracer ^{13}N (half-life = 9.96 min) was

produced in the cyclotron at TIARA by proton irradiation of water. This procedure was described in detail [6].

2.4 Ammonium translocation activity measurement by PETIS

To study $^{13}NH_4^+$ uptake and translocation from roots to whole plant, the roots of a single plant were placed in a 16 cm height glass test tube that contained 20 mL of culture solution with nitrogen source (0.015 mM $(NH_4)_2SO_4$). $^{13}NH_4^+$ (50 MBq, carrier-free in 6 mL) was added to the culture solution after synthesis with gentle aeration for immediate mixing. The light intensity was 500 μmol $m^{-2}s^{-1}$ unless otherwise described. The PETIS analysis performed under ambient conditions described in detail[6]. For nitrogen-deficiency treatment, plants were transferred to culture solution without nitrogen source for 3 days.

2.5 Ammonium and amino acid determination by capillary electrophoresis

NH_4^+ and amino acids were grinding root tissues in 0.01 N HCl at 4°C. Further procedures are described in the reference[6].

3. Results and Discussion

We succeeded in production of the transgenic rice expressing *OsAMT1;2* ORF under constitutive promoter of CaMV 35S, designated as *OsAMT1;2* sense rice. Two transgenic lines were established, which called S1 and S2. Quantitative RT-PCR analysis revealed that transcript for *OsAMT1;2* is much accumulated in the S2 plant compared to that in the S1 (data not shown).

To evaluate the ability of uptake and assimilation of ammonium in the *OsAMT1;2* sense rice, quantitation of ammonium and glutamine in roots after ammonium treatment was examined (Fig. 1). Level of ammonium in

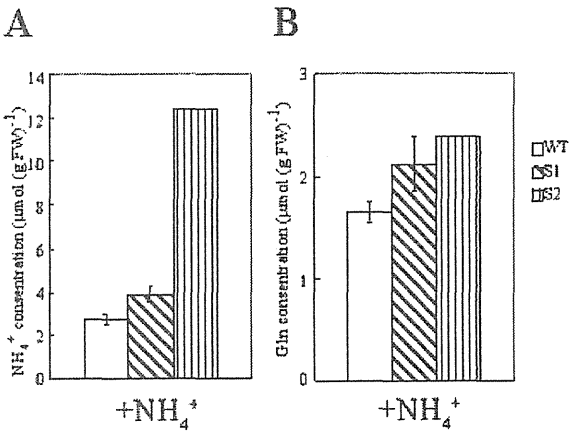

Fig. 1 Levels of ammonium and glutamine in roots quantified by capillary electrophoresis after ammonium treatment. Nitrogen-deprived plants (wild-type, WT; S1 and S2) was treated with 0.15 mM $(NH_4)_2SO_4$ for 4 hr and subjected to the quantitation.

roots of the S1 and S2 plants was approximately 1.4-fold and 4.5-fold higher than that in the wild-type (Fig. 1A), while glutamine was also accumulated in 1.4-fold in both S1 and S2 plants (Fig. 1B), indicating that Overexpression of ammonium transporter gene leads to efficient uptake of ammonium in rice plant.

To confirm the ability of the *OsAMT1;2* sense rice having efficient uptake of ammonium, shoot translocation of $^{13}NH_4^+$ from roots was performed by the PETIS analysis (Fig. 2). Nitrogen-deprived S1 and wild-type plants were transferred to 0.015 mM $(NH_4)_2SO_4$ for 30 min and then subjected to the radioactive $^{13}NH_4^+$. At 45 min after the radioactive ammonium treatment, ^{13}N signal was detected at the basement of leaf sheath in the wild-type (Fig. 2B and 2C), whereas the signal was detectable in most parts of the S1 plant (Fig. 2E and 2F). Accumulation of the signal at the leaf sheath was remarkably enhanced in the S1 compared to that in the wild-type (Fig. 2G). These results indicate that over expression of the *OsAMT1;2* results in enhanced ability for uptake and translocation of ammonium from roots.

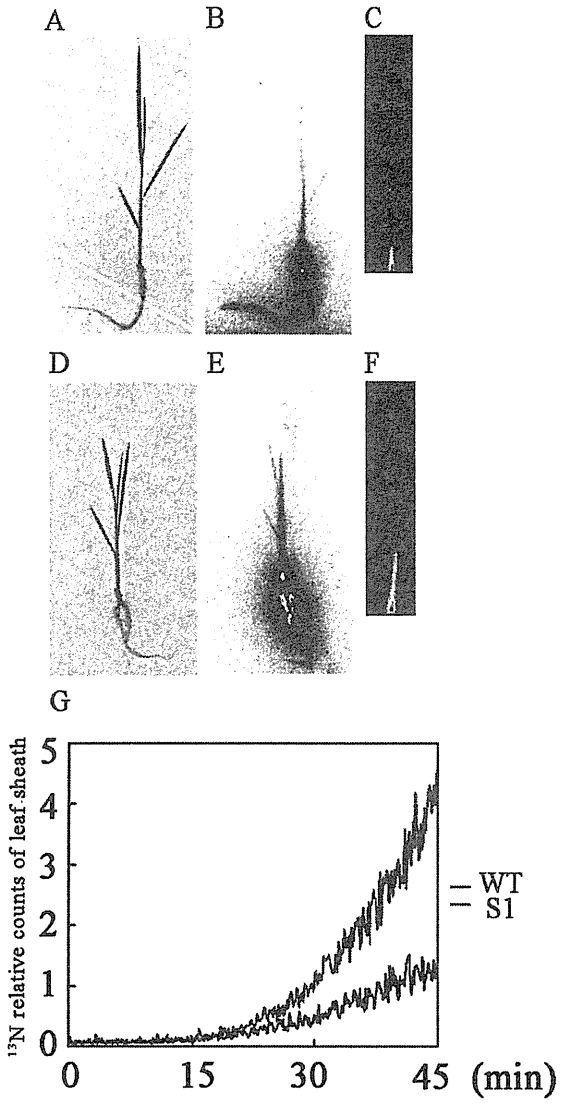

Fig. 2 Uptake and translocation of $^{13}NH_4^+$ from roots to shoot (A to F) and time-course study of translocation of $^{13}NH_4^+$ into leaf sheath (G) in *OsAMT1;2* sense rice. A to C, wild-type; D to F, S1 plant. A and D, photo; B and E, radioactive imaging by BAS1500; C and F PETIS ^{13}N-imaging.

We focused on the initial steps of ammonium uptake and translocation in roots in this study. However, the ammonium translocation would be also regulated by the nitrogen status via a consequence of internal nitrogen cycling and remobilization. Further studies will be needed to evaluate the idea.

References

1) L. Guglielminetti, J. Yamaguchi, P. Perata, A. Alpi, Plant Physiology 109 (1995) 1069-1076.
2) S. Yoshida, Fundamentals of Rice Crop Science. International Rice Research Institute, Manila, Philippines.
3) M.Y. Wang, Y. Siddiqi, T.J. Ruth, A.D.M. Glass, Plant Physiology 103 (1993) 1249-1258.
4) Y. Sonoda, A. Ikeda, S. Saiki, N. Von Wiren, T. Yamaya, J. Yamaguchi Plant Cell Physiology 44 (2003) 726-734.
5) Y. Sonoda, A. Ikeda, S. Saiki, T. Yamaya, J. Yamaguchi Plant Cell Physiology 44 (2003) 1396-1402.
6) S. Kiyomiya, H. Nakanishi, H. Uchida, A. Tsuji, S. Nishiyama, M. Futatsubashi, H. Tsukada, N. S. Ishioka, S. Watanabe, T. Ito, C. Mizuniwa, A. Osa, S. Matsuhashi, S. Hashimoto, T. Sekine, S. Mori, Plant Physiology 125 (2001) 1743-1754.
7) Y. Hiei, S. Ohta, T. Komari, T. Kumashiro, Plant Journal 6 (1994) 271-282

2.35 Visualization of Sink Activity of a Root Parasite, Broomrape, for Translocating Nitrate in the Host Plant

H. Sekimoto*, R. Matsuki*, Y. Kobayashi*, D. Sato**, K. Yoneyama**, Y. Takeuchi**, S. Matsuhashi***, S.Fujimaki***, K. Sakamoto***, N. S. Ishioka***, S. Watanabe***, K. Arakawa*** and T. Kume***
Faculty of Agriculture, Utsunomiya University *
Center for Research on Wild Plants, Utsunomiya University**
Department of Ion-Beam-Applied Biology, JAERI***

1. Introduction

Broomrapes (*Orobanche* spp), root holoparasites, can cause enormous damage before their scapes appear above ground, because their infestation occurs underground. As a consequence, efficient control is extremely difficult and infestation frequently results in a severe reduction of crop yields.

Generally nitrogen fertilizer application reduced the crop damage caused by these root parasites[1,2]. Ammonium affects stimulant production by host plants, seed germination and shoot growth of parasites as well as attachment to the host roots[2,3]. The toxicity or inhibitory effect of ammonium was ascribed to the low activity of glutamine synthetase in root parasites[4,5]. On the contrary, it is known that nitrate markedly promoted stimulant production in the host roots[6].

Broomrapes are efficient sinks for host-derived solutes. A Previous study[7] reported that net carbon fixation was 20% higher in infected host plants, *Nicotiana*, compared with controls. Broomrapes caused a 84% increase in net carbon flux moving downward from the host shoot, and 73% of this carbon was intercepted by the parasite, almost entirely through the phloem. Further the parasite also exerted a large impact on nitrogen status of plants, notably nitrate uptake was stimulated and the amino acid content of xylem sap was lower. They noted that only 1.4% of absorbed N through the xylem from host roots and 41% of N through the phloem from host shoots would be intercepted by broomrapes.

Then, translocation of ^{13}N-nitrate or ^{13}N-ammonium in the root systems of red clover (*Trifolium pratense* L.) infected by broomrapes (*Orobanche minor* Sm.) by a positron emitting tracer imaging system (PETIS) was examined.

2. Materials and methods

2.1 Plant material

To make root systems of red clover infected by broomrapes on one side, broomrape seeds were sown in the soil mixed with vermiculite diagonally under from red clover seeds. After 4 or 5 months, when broomrapes have infected enough and formed tubers, red clover plants with broomrapes were transplanted to the culture solution[8]. They were grown in a growth chamber (14 hours light 350 μmol $m^{-2}s^{-1}$ at 23℃, 10 hours dark at 18℃) for 7 days.

2.2 Experimental set up for ^{13}N-nitrate translocation in the plant root system

Red clover roots were divided into two bundles with or without a tuber of broomrape, and fixed between two acrylic boards and placed midway between a pair of PETIS detectors. The end of the roots which hanged out of the boards was soaked with 20 mL of

the culture solution. About 100 MBq of ^{13}N-nitrate or ^{13}N-ammonium were added to the culture solution to feed them from each bundles of roots, and ^{13}N translocation in the root and shoot of host plant (red clover) and a broomrape tuber was monitored using PETIS for 60 min.

3. Results and discussions

Monitored points in the plant and the pattern of translocation of ^{13}N were shown in Fig. 1. As feeding ^{13}N from root bundle with broomrape tuber, translocation of ^{13}N to broomrape tuber (B) was clearly observed. And translocation of ^{13}N-ammonium to broomrape inclined to increase slightly compared with that of ^{13}N-nitrate, indicating that nitrate would pass easier through broomrape tuber than ammonium.

The pattern of ^{13}N-ammonium translocation to basal shoot (A) from root bundle with broomrape the same as that of ^{13}N-nitrate. Also the pattern of translocation of ^{13}N-nitrate to basal shoot (A) from root bundles with or without broomrape tuber was the same, so that it is not clarified that broomrape inhibited the translocation ^{13}N to basal shoot of host plant. However, the translocation of ^{13}N-nitrate to shoot (D, E) from root bundle with broomrape tuber was less than that without broomrape tuber, suggesting that broomrape would inhibit translocation ^{13}N to host shoots.

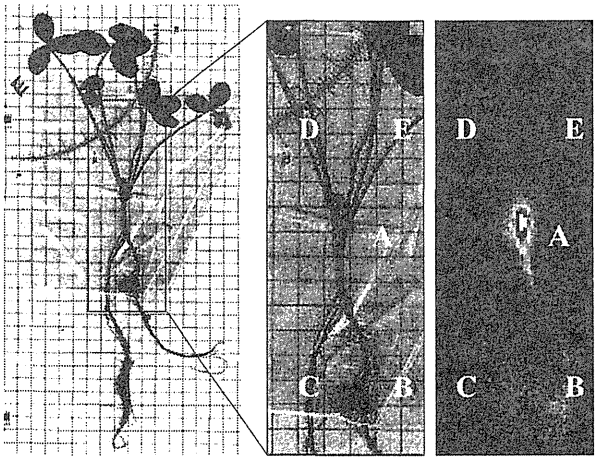

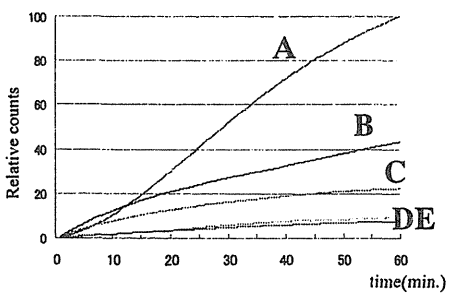

(i) Feeding $^{13}NO_3^-$ from root bundle with brroomrape

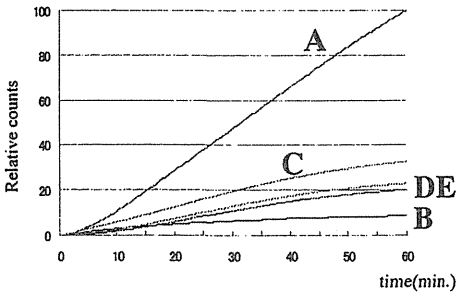

(ii) Feeding $^{13}NO_3^-$ from root bundle without brroomrape

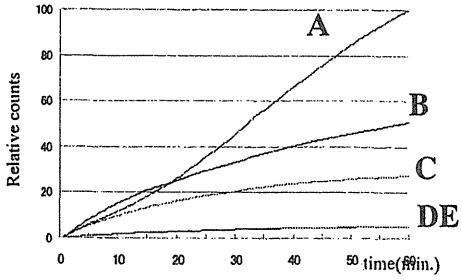

(iii) Feeding $^{13}NH_4^+$ from root bundle with brroomrape

Fig. 1 Monitored points in the plant and the pattern of translocation of ^{13}N

References

1) B.E. Abu-Irmaileh, Weed Sci. 42 (1994) 57-60
2) G.N. Dhanapal, P.C. Struik, M. Udayakumar and P.C.J.M. Timmermans, Agron. Crop. Sci. 176 (1996) 335-359.
3) R. Jain and C.L. Foy, Weed Technol. 6 (1992) 269-275
4) S.F. McNally, B. Hirel, P. Gadal, A.F. Mann and G.R. Stewart, Plant Physiol. 72 (1983) 22-25
5) S.F. McNally, T.O. Orebamjo, B. Hirel and G.R. Stewart, J. Exp. Bot. 34 (1983) 610-619
6) K. Yoneyama, Y. Takeuchi amd T. Yokota, Physiol.Plant.112 (2001) 25-30.
7) J.M. Hibberd, W.P. Quick, M.C. Press, J.D. Scholes and W.D. Jeschke, Plant cell Env. 22 (1999) 937-947
8) T. Tadano and A. Tanaka, Jpn. J. Soil Sci. Plant Nutr. 51 (1980) 399-404

2.36 A Study on Signal Transduction Mechanism Accompanied with Molecular Translocation in Higher Plant

T. Furuichi*, S. Matsuhashi***, N. S. Ishioka***, S. Fujimaki***,
K. Sakamoto**, K. Arakawa**, T. Kume***, M. Sokabe* and S. Muto**
Graduate School of Medicine, Nagoya University *
Nagoya University Bioscience Center, Nagoya University**
Department of Ion-beam-applied Biology, JAERI***

1. Introduction

In planta, photosynthesized sugars are utilized not only as carbon sources but also as signal molecules for growth and development. We have shown that sucrose fed to the root of an autotrophically grown *A. thaliana* intact whole plant containing aequorin in its cytosol caused weak luminescence moving from the lower to the upper leaves.[1] Previously, we have established a simultaneous real time imaging system for movements of sugar molecules and aequorin luminescence in *A. thaliana* mature plants, which consists of a PETIS (positron emitting tracer imaging system) for measuring radioactivity of ^{18}F-deoxyglucose (^{18}FDG) and a VIM-camera system (a CCD camera equipped with an intensifier) for detecting aequorin luminescence, and the time course of ^{18}FDG translocation in leaf was roughly comparable to aequorin luminescence reflecting an increase in $[Ca^{2+}]_{cyt}$.[2] In the present study, we tried to confirm the results with several trials using the established PETIS/VIM-camera dual monitoring system. And we also tried to define some part of the key molecules for the sugar-induced $[Ca^{2+}]_{cyt}$ (cytoplasmic Ca^{2+} concentration) increase and the source / sink conversion mechanism.

2. Experimental procedure

2.1. Plant material

Seeds of *A. thaliana* (cv. Wassilewskija) expressing apoaequorin were sown on 0.3% gellan gum plate containing GM medium[3] with 1% sucrose (GM+Suc medium) and grown at 22.C under continuous light at 4,000 lux with day-light fluorescent lamps. Two-week-old intact plants were transplanted onto fresh plates containing GM medium deficient of sucrose (GM-Suc medium) and grown further 3 - 4 weeks under the same condition. In order to reconstitute aequorin, the roots of intact plants were washed with liquid GM+Suc or GM-Suc medium, and immersed in the same medium containing 2.5 μM coelenterazine overnight in the dark.[1]

2.3. Dual monitoring of the translocation of ^{18}FDG and the $[Ca^{2+}]_{cyt}$ increase in plants

The dual monitoring system constructed by previous work[1] was used for analysis. The roots of a single plant were placed in a bottle containing 10 ml of the culture medium without sucrose. To maintain geometry, the stem and the canline leaves were settled onto a flexible net fixed by acrylic frames, and centered between the PETIS detectors[5]. To start monitoring, 5 ml of the medium was replaced with equal volume of flesh media containing 100 mM glucose and ^{18}FDG.

2.4. Identification of the genes specifically expressed in leaves with the sugar-induced $[Ca^{2+}]_{cyt}$ increase

To identify these genes, mRNA level of ca.

8600 genes in the leaves of both GM+Suc and GM-Suc plants were analyzed with DNA microarray analysis. InteliGene II Arabidopsis CHIP I and II (Takara Inc., Otsu, Japan) were used for this analysis. Total RNA, isolated from leaves of *A. thaliana* with a FastRNA® Kit-GREEN using FastPREP machine (Bio 101., Carlsbad, CA, U.S.A.) according to the manufacturer's protocol, and quantified spectrophotometrically, was labeled with Cy3 and Cy5 fluorescence dye and used as probes for analysis.

3. Results and discussion

Using the PETIS/VIM-camera dual monitoring system, the movement of sugar molecules and the aequorin luminescence in leaves were simultaneously analyzed. As shown in Fig. 1, ^{18}FDG was gradually taken up from root to upper part through the stem. As reported in previous report[2], the uptake rate in the lowest pert (ROI-1) clearly oscillated with periodicity. In this plant, the intensities of the oscillation were gradually decreased from lower part to upper part. This tendency was well conserved in several trials, it seems to be supported our hypothesis, the knot part has the buffering capacity for sugars and minerals translocating in the plant, and regulates supply of solutes to the developing part. Unfortunately the intensity of aequorin luminescence reflecting an increase in $[Ca^{2+}]_{cyt}$ was too weak to visualize, but it was well comparable and conserved in each plants.

Previously, we reported that AtSUC1 and AtSUC2, sucrose/H^+ cotransporters and AtTPC1, the voltage dependent Ca^{2+} permeable channel are the key molecule for the sugar-induced $[Ca^{2+}]_{cyt}$ increase.[6] Though it is well known that a lot of genes are regulated its transcription level by sugar-signaling, the molecular determinants for this response and sink/source conversion mechanism are still unclear. To clarify this question, mRNA level of 8600 genes expressing in the leaves were analyzed by DNA microarray methods. As a results, 200-300 genes which encoding various proteins (Pectinesterase, acetyl-CoA:benzylalcohol acetyltranferase, myo-inositol-1-phosphate synthase -like protein and so on). As further experiments, the expression level of some of these genes in single leaf with/without an increase in $[Ca^{2+}]_{cyt}$ should be analyzed.

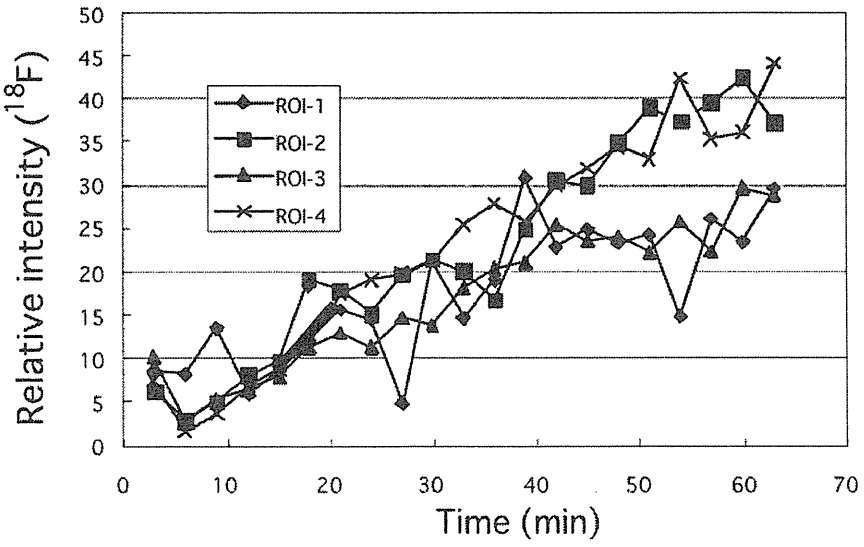

Fig. 1 Time-course study of the translocation of ^{18}FDG into the stem of *A. thaliana* mature plant. Radioactivity curves at the numbered positions which settled from lower to upper part. Squared areas were; ROI-1 and 3; stem, ROI-2 and 4; knot.

References

1) Furuichi, T., Mori, I. C., Takahashi K. and Muto, S. (2001b) Plant Cell Physiology 42, 1149-1155.

2) Furuichi, T., Matsuhashi, S., Ishioka, N., Fujimaki, S., Ohtsuki, S., Sekine, T., Kume, T. and Muto, S. (2003) TIARA Report, 12(2002), 129-131

3) Valvekens, D., Van Montagu, M. and Van Lijsebettens, M. (1988) *Proceeding of the National Academy of Science of the United States of America* 85: 5536-5540.

4) Hmmacher, K., Coenen, H. H. and Stoucklin, G. (1986) *J. Nucl. Med.*, 27, 235-238

5) Kiyomiya, S., Nakanishi, H., Uchida, H., Tsuji, A., Nishiyama, S., Futatsubashi, M., Tsukada, H., Ishioka, N., Watanabe, S., Ito, T., Mizuniwa, C., Osa, A., Matsuhashi, S., Hashimoto, S., Sekine, T. and Mori, S. (2001) *Plant Physiology* 125, 1743-1754

6) Furuichi, T., Cunningham, K.W. and Muto, S., *Plant Cell Pyisiol.*42 (9), 900-905 (2001a)

3. Radiation Chemistry / Organic Materials

This is a blank page.

3.1 Preparation of Hybrid Membranes Consisting of Polymer Membranes and Nanowires using Ion Beam Irradiation

H. Koshikawa, Y. Maekawa and M. Yoshida
Department of Material Development, JAERI

1. Introduction

When polymeric membranes are irradiated by heavy ion beams, each single heavy ion particle deposits its energy to a substrate in a region of less than 10 nm in diameter along the ion-path through membranes. The damaged region is susceptible to a proper etchant, resulting in the formation of through-holes with nanoscopic diameters, which are called "ion track membrane"(Fig.1a).[1] We have developed the ion track membranes made of thermally and mechanically stable polymers such as poly(ethylene terephthalate) (PET) and polyimide (PI), which can be applied to nanoscopic electronic devices such as anisotropic conductive films and field emitters through hybridization with conducting metals and semiconducting alloys by electroplating. (Fig.1b).[2-4]

The anisotropically conducting films, which consist of a insulating polymer with cylindrical conductive copper wires, have been used as conductive adhesive films in manufactures of printed circuits and multi-tip modules. These pores have been prepared by laser beam ablation, which has resolution limitation of several microns in diameter due to surface roughness caused by heat damages. Since, smaller size pores with smoother surfaces are required for manufacturing high-density and high-capacity electronic devices, we report herein the application of the ion track membranes to the fabrication of anisotropically conducting films consisting of copper wires of a diameter which is 40 times smaller than those of commercially available films.

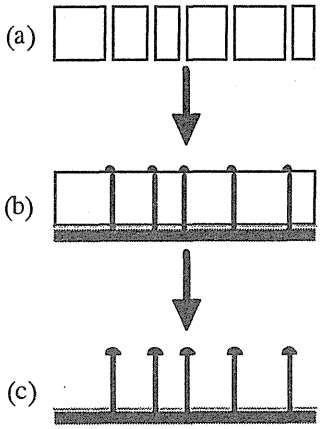

Fig. 1 The fabrication of conductive and insulating hybrid membranes consisting of wires in ion track membranes.

2. Copper wires - PET ion track membranes

Commercial PET films with 12 μm in thickness were irradiated by $^{129}Xe^{23+}$ (450 MeV) beams with a fluence of 3.0×10^8 ions/cm^2. The irradiated films were etched in 0.2 M NaOH aqueous solution at 60 °C for 10.5 h. As shown in Fig. 2(a), the clear hole patterns with 260 nm in diameter were observed in the SEM image of the surface of the PET ion track membrane.

Successive layers of gold (25 nm) and copper (20 μm) were coated at one side of the PET ion track membranes as a cathode. Then, the copper wires were deposited within the pores of ion track membranes onto the copper cathode by electrochemical plating in pH1 aqueous solution of 1.3M copper sulfate ($CuSO_4$) with periodic potential modulation (-0.2V; 6sec, 0.2V; 1sec).

In order to observe the copper wires which grew into the pores of the ion track membranes,

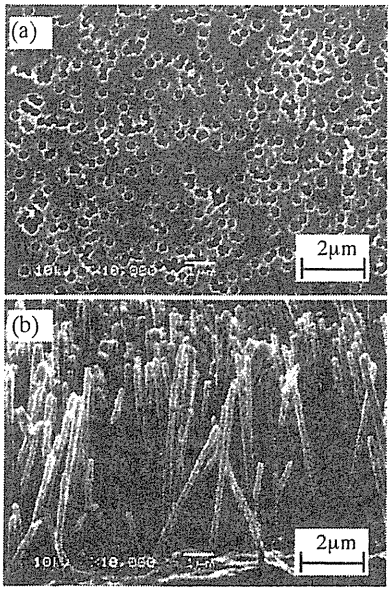

Fig. 2 (a) The PET ion track membrane; 260 nm in diameter. (b) The copper nanowires; 260 nm in diameter, 12 μm in height.

PET films must be removed from the copper electrode. Only PET films were swelled with partial dissolution and totally removed without the damage of the copper wires when the hybrid membranes were soaked in 10 M KOH/ethanol (3:7 w/w) at 70 °C for 30 minute (Fig. 1c). As shown in Figure 2b, the geometry of the copper wires was observed by SEM and was found to be 260 nm in diameter and 6.3 μm in height, which were in good agreement with the size of the pores.

Next, we evaluated the conductivity of the membranes consisting of PET film and perpendicularly aligned cylindrical copper wires with 12 μm in height and 200 nm in diameter by the measurement of the membrane resistance in the directions perpendicular and parallel to the surfaces by four terminal resistance method. The membrane showed the resistances perpendicular to the surfaces in the ranges from 1.5 x 10^{-7} to 1.5 x 10^{-8} Ω/cm^2 and the average resistance is estimated to be 6.9 ± 3.7 x 10^{-7} Ω/cm^2. This average resistance of the membrane is about three times higher than the theoretical resistance (2.1 x 10^{-7} Ω/cm^2) estimated using following equations;

$$R_t = 1/S = \rho L/(\pi(r/2)^2 F) \qquad (1)$$

where ρ is copper resistivity (1.67 x 10^{-6} Ωcm), L is wire length (1.2 x 10^{-3} cm), r is cross-sectional diameter of copper wires (0.2 x 10^{-4} cm), and F is an ion flux (the number of pores 3.0 x 10^7 ions/cm^2). Such lower conductivity of the PET/Cu hybrid membranes compared with the calculated value is likely to result from the defects in copper wires during the electroplating preparations, influence of the interfaces between copper wires and the pore surfaces of PET, and/ or the contact resistances between the needle probe and the top of copper wires.

3. Copper wires - PI ion track membranes

Commercial PI (Kapton, thickness 12 μm) was irradiated by $^{129}Xe^{23+}$ (450 MeV) ion with a fluence of 3x10^8 ions/cm^2. The PI ion track membranes with cylindrical pores were prepared by etching in pH9 sodium hypochlorite (NaClO) at 60 °C. The clear pores with 200 nm in diameter were observed in the SEM image of the surface, as shown in Fig. 3a.

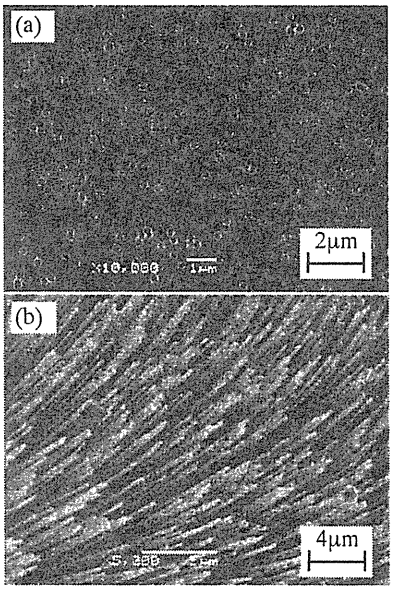

Fig. 3 (a) The PI ion track membrane; 200 nm in diameter. (b) The copper nanowires; 200 nm in diameter, 12 μm in height.

Successive layers of gold (25 nm) and copper (20 μm) were coated at one side of the PI ion track membranes as a cathode. Then, the copper wires were deposited within the pores of ion track membranes onto the copper cathode by electrochemical plating in pH1 aqueous solution of 1.3M copper sulfate ($CuSO_4$) with periodic potential modulation (-0.2V; 6sec, 0.2V; 1sec). The PI film was removed from the copper electrode with copper wires using a NaClO at 60 °C for 30 min; then, the geometry of copper wires on copper electrode were estimated by SEM measurement (Fig. 3b).

4. Cadmium sulfide wires - PET ion track membranes

For another application of ion track membranes to an electroluminescence device, we utilize cadmium sulfide (CdS), which was a semiconductor and can be deposited into the pores of the ion track membranes by electroplating method as mentioned above.

The PET membranes (12μm) with a pore size of 160 nm were used. On the one side of the membranes was coated platinum (25 nm), and was deposited copper (20 μm) as a cathode. Then, the CdS wires were deposited within the pores of ion track membranes onto the copper cathode by electrochemical plating in dimethyl sulfoxide solution of 0.05M cadmium chloride and 0.19M sulfur with constant potential (-4V). The deposited wires were confirmed to be CdS crystals but not metal Cd with X-ray diffraction of the deposition films; where the peak at 28.4° assigning to CdS (101) reflection without any peaks assigning to Cd crystals. The geometry of the CdS wires, which was observed with SEM, was found to be 160 nm in diameter, which were in good agreement with the size of the pores. Further studies are currently underway in applying the etching and plating methods to prepare hybrid films having CdS nanowires with a diameter of less than 50 nm in PET and PI matrix to develop light emitting devices.

Reference

1) C. Trautmann, W. Brüchle, R. Spohr, J. Vetter, and N. Angert, NIM B 111 (1996) 70.
2) T. Molares, V. Buschmann, D. Dobrev, R. Neumann, R. Scholz, I. U. Schuchert, and J. Vetter, Adv. Matter., 13 (2001) 62.
3) Y. Maekawa, H. Koshikawa, and M. Yoshida, Polymer, 45 (2004) 2291.
4) Z. Zhu, Y. Maekawa, H. Koshikawa, Y. Suzuki, N. Yonezawa, and M. Yoshida, NIM B 217 (2004) 449.

3.2 Study on Track-etched Pores in γ-Irradiated PET Films

A. Hiroki, M. Asano, T. Yamaki and M. Yoshida
Department of Material Development, JAERI

1. Introduction

Swift heavy ion bombardment produces a cylindrical damage along the incident axis in polymer. Such localized damage called a latent track is preferentially dissolved during the chemical etching to give functional film materials with uniform pores in the nanometer range[1]. The track-etched membranes have wide applications in industry as well as in high technology area[2,3].

The evolution of the tracks during the etching is monitored by the conductometric method that is suitable for the observation of the size and morphology of latent tracks in a polymer[4]. Scanning electron microscopy (SEM) is also used to observe the track-etched pores on the surface of polymer films. Such observations of the track-etched pores would be of great importance.

It is known that ultraviolet (UV) irradiation and soaking in a special solvent as a pre-treatment of etching process are useful method for sensitizing the ion tracks[5,6]. The additional UV irradiation in the presence of oxygen induces the modification of gel-like layer structure formed in the track, resulting in the acceleration of an alkaline etching of latent tracks[7]. Since changes in chemical structure of polymer induced by γ-irradiation occur in the more interior polymer films compared to UV irradiation, the formation of track-etched pores would be affected more effectively by γ-irradiation.

In the present work we investigated the effect of γ-irradiation on the formation of track-etched pores in polyethylene terephthalate (PET) films, compared with the results of SEM observations and conductometry.

2. Experimental

PET films with thickness of 38 μm (Hoechst JAPAN) were irradiated with $^{129}Xe^{23+}$ ions of 3.5 MeV/n (3.0×10^6 ions/cm^2) at the TIARA, JAERI (Takasaki, Japan). The irradiated films were exposed to γ-rays with a dose of up to 160 kGy in vacuo at room temperature. The etching was carried out in a 0.2 M NaOH aqueous solution at 70°C. Track etching was performed by mounting an irradiated film as dividing wall into a conductometric cell made of Teflon. During etching process, the electrical resistance, R, of the cell was monitored as a function of etching time. Assuming cylindrical geometry, the effective pore diameter, d_2, at a given time can be calculated by

$$d_2 = (4l/\pi kNR)^{1/2} \qquad (1)$$

where l is the sample thickness, k is the specific conductivity of the etchant, and N is the number of tracks in the sample. The pore diameter was also observed by using SEM.

3. Results and discussion

The pore diameter of the PET films etched for 6 hours in the 0.2 M NaOH aqueous solution at 70°C and the bulk etch rate estimated from the change of thickness for PET films are plotted as a function of irradiation doses in Fig. 1. The pore diameters of the PET films determined by the SEM observation gradually decreased with increasing the γ-irradiation doses. As the irradiation doses reached 160 kGy, it was

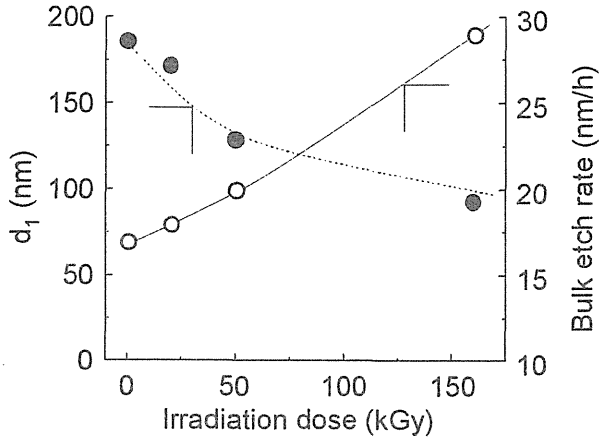

Fig. 1 Effect of γ-irradiation dose on the pore diameter (d_1) and bulk etch rate for PET films. The pore diameter in this figure determined by SEM after 6-hour etching in a 0.2 M NaOH solution at 70°C.

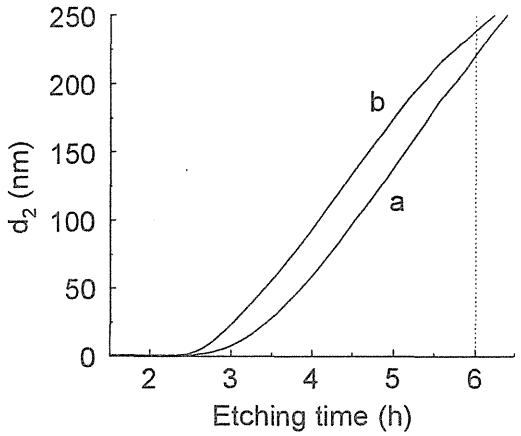

Fig. 2 Effective pore diameter (d_2) calculated from electric conductance as a function of etching time in a 0.2 M NaOH solution at 70°C. The PET films were γ-irradiated with doses of (a) 0 and (b) 160 kGy after ^{129}Xe ion irradiation (3.5 MeV/n).

approximately half of the pore diameter of the non-irradiated PET films, as shown in Fig. 1. On the other hand, the bulk etch rate of the PET films increased with increasing the γ-irradiation dose. This is considered to be due to the degradation of PET induced by γ-irradiation from the fact that PET is known as a polymer decomposed by ionizing radiation.

Fig. 2 plots the effective pore diameters calculated by equation (1) as a function of the etching time. The effective pore diameter of the PET film irradiated with the doses of 160 kGy was larger than that of the non-irradiated one. For example, the effective pore diameter of PET film irradiated with the doses of (a) 0 kGy and (b) 160 kGy reached about 220 nm and 240 nm after 6-hour etching, respectively. The pore diameters of PET film with 0 kGy obtained between the SEM observation and conductometry were almost same within an experimental error. However, as irradiated with γ-ray, the effective pore diameter calculated by conductometry was in complete disagreement with that obtained by the SEM observation, especially in γ-irradiation with 160 kGy. The effective pore diameter was determined by Eq. (1) based on the assumption that the pores are cylindrical and the specific conductivity of the etchant in the pores is equal to that in a bulk solution. In these experiments, since the track to bulk etch rate ratio was more than 100, the above assumption would be justified. It is suggested, therefore, that there is some reason for generating the difference of pore diameter obtained between the SEM observation and conductometry.

We consider an existence of the swollen state during the etching process. Recently, it was indicated that the etching process consisted of the several stages: 1) the electrolyte penetration into the track, 2) the removal of radiolysis products, 3) the swelling of polymer areas around the track, 4) the removal to the swollen polymer, and 5) the formation of the track-etched pore[7,8]. On the third stage, the crosslinking structure formed around the tracks causes the swollen polymer by absorbing an etchant to give a gel layer.

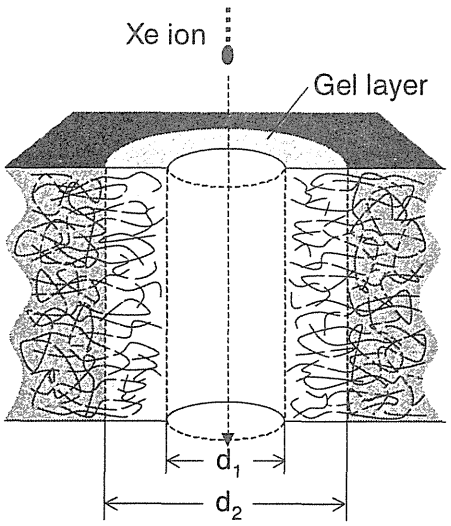

Fig. 3 Proposed model for explaining the difference in pore diameter obtained between the SEM (d_1) and electric conductometry (d_2).

As illustrated in Fig. 3, we proposed the model for explaining the difference in pore diameter obtained between the SEM observation (d_1) and electric conductometry (d_2). It is guessed that the electrical current passes through the gel layer swollen by absorbing the etchant as well as a bulk solution. Consequently, the gel layer must be considered as an ion transportable region in the conductometric method. Actually in our experiments, the effective pore diameter (d_2) obtained by conductometry exhibited the larger than that from SEM observation. Furthermore, the difference of pore diameter obtained between SEM observation and conductometry increased with increasing the irradiation doses, as shown in Figs. 1 and 2. The formation of crosslinked polymer network around the track was promoted by the γ-irradiation to prevent the removal of the polymer chain. As a result, the thickness of gel layer increased, followed by the decrease of the removal rate of polymer from the PET film. For instance, the thickness of the gel layer (= $(d_2-d_1)/2$) of the PET film irradiated 160 kGy at 6-hour etching was estimated to be about 75 nm. Thus the changes in the thickness of the gel layer with γ-irradiation have never been reported in the previous papers, regarding other pre-treatments such as UV irradiation and organic solvent soaking.

4. Conclusions

PET films bombarded with ^{129}Xe ions (3.5 MeV/n) were irradiated with γ-rays and then etched in NaOH aqueous solutions to prepare the track-etched membrane. The difference between the pore diameter obtained by the SEM observation and the electrical conductometry increased with increasing γ-irradiation doses. The formation of the crosslinked region around the track was produced effectively by γ-irradiation, resulting in the increase of the gel layer swollen by absorbing the etchant.

References

1) P. Y. Apel, *Radiat. Meas.*, **34**, 559 (2001)
2) R. Spohr, Ion Tracks in Microtechnology. Principles and Applications. Vieweg Verlag, Braunschweig, 1990.
3) B. V. Mchedlishvili, V. V. Beryozkin, V. A. Oleinikov, A. I. Vilensky, and A. B. Vasilyev, *J. Membrane Sci.*, **79**, 285 (1993).
4) P. Y. Apel, I. V. Blonskaya, V. R. Oganessian, O. L. Orelovitch, C. Trautmann, *Nucl. Instr. and Meth. B* **185**, 216 (2001).
5) P. Y. Apel, *Radiat. Meas.*, **25**, 667 (1995).
6) Z. Zhu, Y. Maekawa, H. Koshikawa, Y. Suzuki, N. Yonezawa, M. Yoshida, *Nucl. Instr. and Meth. B* **217**, 449 (2004).
7) A. I. Vilensky, A. L. Tolstikhina, *Russ. Chem. Bull.*, **48**, 1100 (1999).
8) A. I. Vilensky and G. S. Zhdanov, *High Energy Chem.*, **32**, 88 (1998).

3.3 Yield of OH Radicals in Water under Heavy Ion Radiolysis

M. Taguchi and T. Kojima
Department of Material Development, JAERI

1. Introduction

The heavy ion-induced chemical reactions in aqueous solutions are strongly dependent on concentrations and spatial distribution of OH radicals from water molecules. Clarifying of reaction mechanisms of OH radicals is very important point both in radiation chemistry and radiation biology. The heavy ion deposits densely its kinetic energy around the trajectory. The initial spatial distribution of OH radicals is the same as that of energy deposition along the trajectory. OH radicals, however, disperse time by time within their life, and relevant chemical reactions attributed to OH radicals are very complicated. Therefore, neither 'average LET' nor 'average yield' is suitable parameter for detailed investigation at irradiation effects. The purpose of this study is to understand chemical reactions on the basis of physical track structure theory.

We investigated OH radicals yields, which change with the specific energy in water, at specified reaction times just after the irradiation of several ten MeV/n C ions.

2. Experimental

Water containing phenol at 0.5-100 mM was saturated with oxygen to dissolve by 30-minute bubbling. The solution was put into an aluminum irradiation cell with a magnetic stirrer chip. The cell has an aluminum window of 15-μm thickness and 40-mm diameter which makes C ion pass through the water sample.

Heavy ion used in this study was 220-MeV $^{12}C^{5+}$ provided from an AVF cyclotron in TIARA facility. Fluence rate was about 5×10^{8} ions/cm^2/s at the surface of the sample solution.

The aqueous solutions irradiated were analyzed by High Performance Liquid Chromatography (HPLC) with a reversed phase column (Shodex, Rspak DE-613) at 40 ℃. Acetonitrile mixed with 70-%(v/v) aqueous H_3PO_4 solution (0.01 M) was used as an eluent at a flow rate of 1.0 mL/minute. The irradiations and the data analyses were performed as described in the previous papers.[1,2)]

3. Results and discussion

Hydroquinone, resorcinol and catechol were identified on the HPLC chromatogram as irradiation products, which are induced by addition of one OH radical to *p*-, *m*- and *o*-position of phenyl ring. The number of oxidized products per a single C ion (N), which is integration over entire trajectory, increased super-linearly with an incident energy of C ion. The values of the differential G-value (G'-value) are estimated by differentiating N with a third order function of the energy. The G'-values of the oxidized products were in the range of 1/10 to 1/2 of the G-values obtained for ^{60}Co γ-ray irradiation. In the case of γ-ray irradiation, total G-value of the whole oxidized products is larger than 90 % of the G-value of OH radical. The G'-values of OH radicals were estimated using following equation;

$$G'(\mathrm{OH}) = \frac{\Sigma G'(\mathrm{product})}{\Sigma G(\mathrm{product})} \times G(\mathrm{OH}) \quad (1)$$

The estimated G'-values of OH radicals were plotted against specific energy of C ion (Figure

1). The *G*'-values of OH radicals increase monotonously with the specific energy. The *G*'-values will approach to the constant value (2.7) which is obtained for ^{60}Co γ-rays.

The mean value of the reaction time of the OH radical with phenol is regarded as $(k_{OH}[\text{phenol}])^{-1}$, where k_{OH} and [phenol] are the rate constant of OH radicals with phenol and the concentration of phenol, respectively. Accordingly, the *G*'-values obtained for the phenol concentrations of 0.5, 10, and 100mM are the mean value of the reaction time of about 1.5, 15 and 300 ns, respectively. The *G*'-values are relatively large at the primary stage and decrease with time after the end of irradiation (the reaction time). The decreases of the *G*-values with the reaction time are generally observed for γ-ray and electron beam irradiation. OH radicals are consumed in consequence of the reactions with hydrogen and hydrated electron produced by the irradiation.

The result suggests that the study with consideration of reaction time by changing concentration of solute is important to establish a chemical track model on the basis of physical track structure. We investigate the *G*'-value for the other ions taking into account of difference in the reaction time.

References

1) M. Taguchi, et al., *Radiat. Phys. Chem.*, **60**, 263 (2001).
2) M. Taguchi, et al., *JAERI-Review*, **2003-033**, 141 (2003).

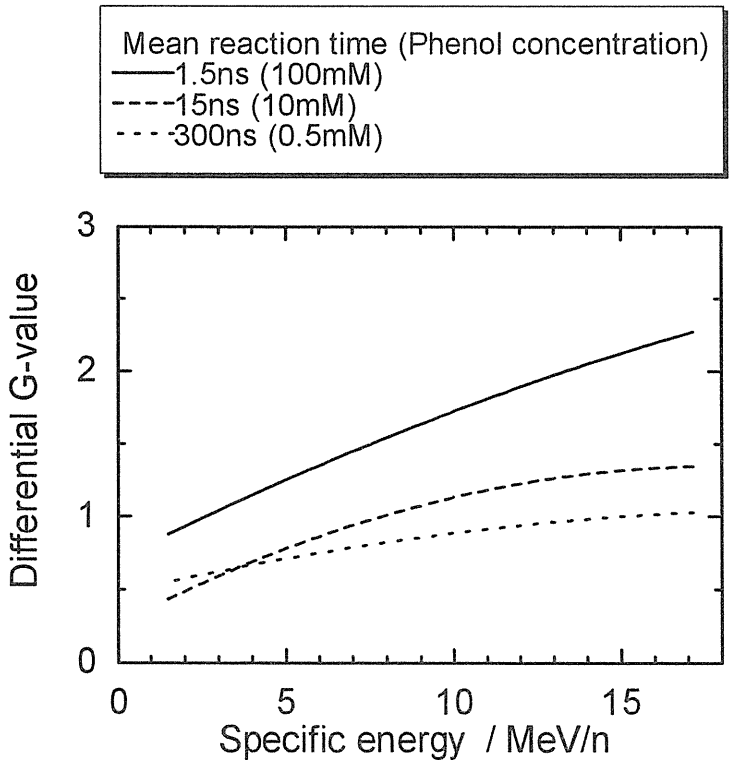

Figure 1 Differential G-value of OH radicals depending on the time after the irradiation.

3.4 Development of Light Absorbance Measurement System under Heavy Ion Irradiation Based on the Photon-counting Method

M. Taguchi and T. Kojima
Department of Material Development, JAERI

1. Introduction

High energy heavy ions deposit their kinetic energy in the narrow concentric region with several tens nm radius around the trajectory. The spatial energy distributions in water are characterized by the atomic number and specific energy (energy per nucleon). Investigations of transient species produced in water about their yields, behaviors and chemical reactions are very important in order to understand the irradiation effects of heavy ions.

The present study is aiming to understand heavy ion induced chemical reactions by analyzing time-behavior of transient species just after the single heavy ion irradiation. We developed the light absorbance measurement system for measuring transient species based on the photon-counting method from the viewpoint of energy deposition theory that heavy ions densely deposit their kinetic energy along the trajectory.

2. Apparatus

In the case of conventional pulse radiolysis system using high energetic electrons, optical measurement system is easily constructed under the atmospheric pressure to observe reactions of radicals in water.

There are many difficulties for constructing the heavy ion pulse radiolysis system as follows; 1) heavy ions have extremely short penetration range in air and samples, and system is required to be constructed in vacuum, 2) yield of radicals are considered to be low because heavy ions deposit densely their kinetic energy and free radicals recombine each other in the track, 3) high time resolution (1 ns) is needed for prompt reaction analysis for observing the recombination process, and 4) high accuracy of positions of irradiation and observation is needed because one pulse of the ion includes less than 10 ions.

We designed the new optical measurement system under heavy ion irradiation for resolving above four difficulties. Figure 1 shows schematic diagram of the light absorbance measurement system having the irradiation cell, optical analysis parts (light source and detectors). Scintillator with 20-μm thickness was set just over the surface of the sample water in the cell for emitting the light, which is used for analyzing the chemical reactions induced by the heavy ions. The analysis-light, which provides information about transient species, was measured from the downstream of the ion beam.

Intensity of the light shows the maximum just after the timing of the heavy ion passing through the scintillator and decays with time. The heavy ion passed through the scintillator enters into the aqueous solution and produces transient species, e.g. OH radicals and hydrated electrons. These transient species react with solute, and their products absorb the light at the specific wavelength. The absorbance change in the sample solution as the function of time after irradiation was obtained using pure water sample as reference.

3. Results and discussion

Heavy ions used in this study were 220 MeV $^{12}C^{5+}$ ions provided from an AVF cyclotron in TIARA facility. C ions have a relatively long

penetration range at about 1mm in water. Repetition rate of C ion pulses was about 20 MHz. Sintered alumina plate (Al_2O_3, Desmarquest AF995R), which gives a short lifetime light less than 1ns, was irradiated in order to evaluate the time resolution of the constructed the light absorbance measurement system preliminary. Photons from the alumina plate were detected through an interference filter at 330 nm by a photomultiplier tube (PMT). The PMT is a head-on type with a quartz window. Signals from the PMT were amplified by the preamplifier and fed into the constant fraction discriminator. The zero timing signal was derived from the cyclotron and adjusted with the gate and delay generator. The time between the zero timing signal and the timing signal of the light was obtained by the TAC (Time-to-Amplitude Converter) with 500 ns full scale and counted by the MCA (multi-channel analyzer). The time profile of light from the alumina plate irradiated with C ions was recorded. Observed pulses of the light were 3 ns FWHM and 20 MHz repetition. Therefore, pulse width of C ion from the cyclotron was about 3 ns and time resolution of the light absorbance measurement system is considered to be less than 1 ns. Since interval of C ion pulses (about 50 ns) is too short to observe the chemical reactions throughout in water, the frequency of the ion pulsed reduced at 3MHz by a sinusoidal chopper (S-chopper) installed just after the beam emitting gate of the cyclotron.

Figure 2 shows the time profiles of light from the scintillator observed directly (I_0) and through aqueous KSCN solution (I) at 480 nm. Large peak observed at 0 ns was X-ray noise. Difference between the time profiles of I_0 and I was observed in the range of 20 to 60 ns.

Water without solute is almost transparent at 480 nm even after the irradiation. $(SCN)_2^-$ radical in consequence of the reaction of OH radicals with SCN^- has strong absorbance at 480 nm. Therefore, the reduction of the light intensity should be ascribed to the absorbance of $(SCN)_2^-$ radical. Radical concentration (C_r) can be estimated by the following equation;

$C_r = \log(I_0/I)/\varepsilon/l$).

where ε and l are the molar extinction coefficient and the range of C ion in water, respectively.

Our light absorbance measurement system developed based on the photon counting method should be useful to observe the behavior of the short lived free radicals under heavy ions irradiation.

Acknowledgement

The present work was supported by the REIMEI Research Resources of Japan Atomic Energy Research Institute in 2003.

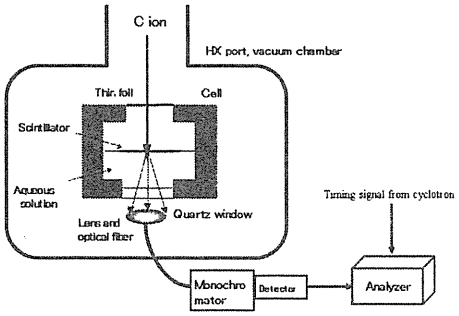

Figure 1 Light absorbance measurement system for heavy ions.

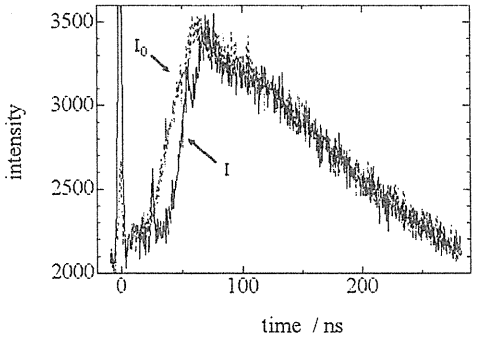

Figure 2 Time profiles of light from the scintillator observed directly (I_0) and through aqueous KSCN solution (I) at 480 nm.

3.5 Primary Process of Radiation Chemistry Studied by Ion Pulse Radiolysis

Y. Yoshida*, J. Yang*, S. Seki*, S. Tagawa*, H. Shibata**, M. Taguchi***, T. Kojima*** and H. Nanba****

ISIR, Osaka University*

Faculty of Engineering, Kyoto University**

Department of Radiation Research for Environment and Resources, JAERI***

Department of Material Development, JAERI****

1. Introduction

Radiation effect of high energy and high LET ion beams on the material is very interesting and was investigated by many researchers, because the highlly-densed irradiation makes the different effect from that by low-LET radiation, such as γ rays. We have studied the primary process of the ion beam-induced radiation chemistry by using the technique of ion beam pulse radiolysis for emission spectroscopy.[1-3)]

The LET effect on the time-dependent emission could be discovered by using the ion beam pulse radiolysis of the polystyrene. However, the whole mechanism of LET effect can not be elucidated, because the information on the other important short–lived species, such as electron and cation radical, can not be obtained by the emission spectroscopy. The behavior of other short-lived species can be detected by using absorption spectroscopy. However, there are many difficulties to the absorption spectroscopy, such as the ion beam intensity, the penetration of the ion beam into material, the light source, and so on.

A new idea on the absorption spectroscopy system is proposed to overcome the difficulties. The points of the system are the production and the detection of the analyzing. The preliminary time-dependent absorption data have been obtained.

2. Experimental

Figure 1 shows the system for ion beam pulse radiolysis for absorption spectroscopy. A liquid sample is irradiated by 220MeV C^{5+} pulsed ion beam from the AVF cyclotron. A thin scintillator floats on the liquid sample. The pulsed ion beam produces the emission through the scintillator, which is used as analyzing light. The analyzing light is introduced to an optical detection system through a lens and an optical fiber. The single photon counting technique is used in the optical detection system, because the ion beam intensity is very small.

BGO (Bismuth Germanate; $Bi_4Ge_3O_{12}$) was used as the scintillator. The lifetime and band of the emission are 300 ns and 480 nm, respectively.

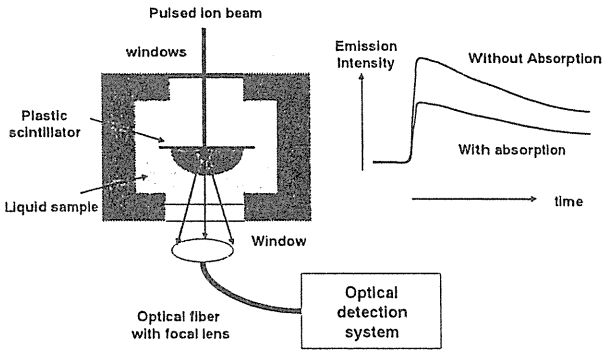

Fig. 1 Absorption spectroscopy system for ion beam pulse radiolysis

3. Results and Discussion

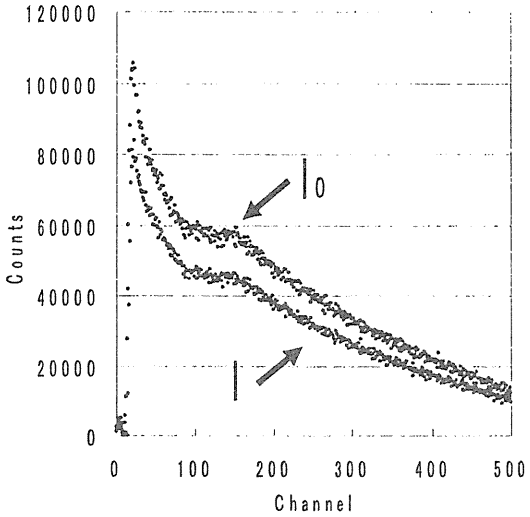

Fig. 2 Time-dependent behavior of analyzing light of I and I_0 obtained in 220 MeV C^{5+} pulse radiolysis of water monitored at 500 nm

To obtain the optical density, OD, in the pulse radiolysis, both the analyzing light intensity with the beams, I, and that without the beam, I_0, have been measured. In this system, it is difficulty to measure I_0 because the analyzing light is produce by the ion beam. To avoid the problem, I_0 was measured by using empty cell.

Figure 2 shows the typical outputs, I and I_0 from the photon counting system obtained in the 220MeV C^{5+} ion beam pulse radiolysis of water. Both data were measured in the same condition of the ion beam intensity and the measuring time. The intensities at time=0 (around 20 ch) did not agree. That was caused by that the optical measuring system of the empty cell was not the same as that of the cell containing the water. Therefore, OD is calculated as follows.

$$O.D. = \log \frac{I_0 \times A}{I} = \log \frac{I_0}{I} + \log A$$

Where A is a factor which is caused by the disagreement of the analyzing light intensity at time = 0. The value of the factor A could not be determined in the experiment. This means that the zero position of the optical density can not be decided.

Although the transient absorption contains the problem on the absolute value, the trend of the time-dependent behavior can be discussed, because the factor A should not be so large. Figure 3 shows the time-dependent optical absorption of the hydrated electron obtained in the 220MeV C^{5+} ion beam pulse radiolysis of water monitored at 480 nm. The raise of the absorption was 20 ns, which was equal to the time resolution of the system. The decay consisted of two components, very rapid decay with the lifetime of about 10 ns, and a slow component. The similar result was reported by W. G. Burns et al.[4] The kinetics is very different from that observed in the case of low LET radiation. Two-component decay is often observed in the ion beam pulse radiolysis for emission spectroscopy. The rapid decay is caused by highly-densed excitation of the ion beam.

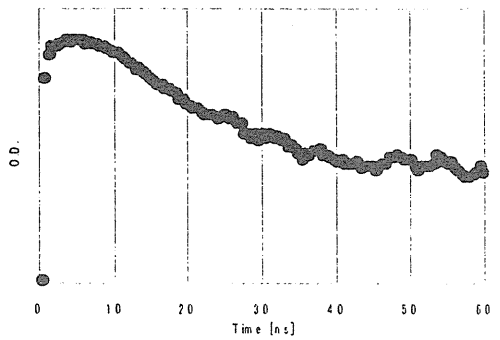

Fig. 3 Time-dependent behavior of hydrated electron obtained in 220 MeV C^{5+} pulse radiolysis of water monitored at 600 nm

References

1) H. Shibata et al., Nucl. Instrum. Meth., A327, 53, 1993
2) Y. Yoshida et al., Nucl. Instrum. Meth, A327,41, 1993
3) H. Shibata et al., Nucl. Instrum. Meth.,B105,42,1995
4) W. G. Burns et al., Faraday Diss. Chem. Soc. 63 (1977) 47

3.6 Properties of Nanowires Formed by Single Ion Hitting to Si-based Polymers

S. Seki*, S. Tsukuda*, S. Tagawa*, M. Sugimoto** and S. Tanaka**
The Institute of Scientific and Industrial Research, Osaka University*
Department of Material Development, JAERI**

1. Introduction

Nanostructure materials have attracted much attention due to their unique electronic and extraordinary mechanical properties.[1-3] Various synthesis procedures for the nanotubes have been suggested, however, it is difficult to control their size, spatial distribution, and structure.

Polysilane derivatives are themselves one-dimensional semiconducting wires, considering their highly developed σ-conjugated system along a Si backbone, and exhibit interesting physical properties.[4-7] The manipulation of a single polysilane molecule has also been successfully performed to observe directly the structure of a Si skeleton, and the electronic properties of a single chain has been estimated.[8]

Recently, we developed crosslinked polysilane nanowires with an entirely new synthesis method (single ion hitting method).[9] Nanowires consisting of crosslinked polysilane derivatives are therefore expected to be applied in new molecular photoelectronic devices.[9,10] The highly efficient electroluminescence (EL) characteristic is one of the most attractive features of the polysilane derivatives,[11] and the nanofabrication technique of the polymer materials will make it possible to use them not only as light emitting devices with quantum size effects but also as candidates for optoelectronic nanodevices including optical fibers and lasing materials. In the present paper we demonstrate not only the direct formation of the nanowires by single ion hitting but also the electronic properties of a nanowire produced by precisely fabricating electrodes with a "nanogap". The adhesion control of the nanowires by surface treatment of substrates is also discussed as a key technique for the fabrication of the electrodes and the characterization of the nanowires.[12]

2. Experimental

Poly(methylphenylsilane) (PMPS) was synthesized by the Kipping reaction.[13] The PMPS was fractionated by separatory precipitation, resulting in PS1 (Mn = 1.5 ~ 1.1 x 10^5), PS2 (Mn = 2.6 ~ 2.1 x 10^4), PS3 (Mn = 1.1 x 10^4~ 9.0 x 10^3), and PS4 (Mn = 5.0 ~ 3.9 x 10^3), with a small dispersion of less than 1.5.

The polymers were spin-coated on substrates, and irradiation was carried out by using Ar, Kr, Xe, and Au ions from the "TIARA" cyclotron accelerator at the Japan Atomic Energy Research Institute, Takasaki Radiation Chemistry Research Establishment. After irradiation, the samples were adequately developed in ether and benzene. The observation of the nanowires was carried out by using Seiko Instruments Inc.(SII) SPI-3800 atomic force microscope (AFM) and a JEOL JSM-6335F scanning electron microscope (SEM). The ultraviolet-visible (UV-vis) absorption and photoluminescence spectra of the nanowires were recorded using a Shimadzu UV-3100PC and Perkin-Elmer LS-50B.

Platinum electrodes were fabricated by a liftoff method on the substrates after the formation of nanowires (Fig. 1). The electron beam (EB) resist (ZEP 520-22, Nippon Zeon Co.) was *overcoated* on the substrates with adhered nanowires. The positive patterns were prepared by EB lithography, with an ELC-7700 EB writing system of Elionix

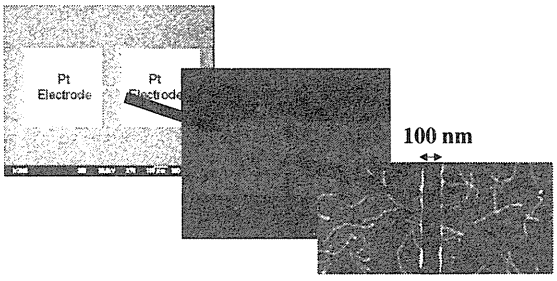

FIG. 1 SEM images of fabricated Pt nanogap electrodes

Inc. Platinum (Pt) electrodes were deposited through the resist mask patterns by a sputter-evaporation technique. The mask patterns were removed by organic solvents after the evaporation. I-V measurement and in situ observation by AFM were carried out by using a SII SPI-4000 scanning probe microscope system with an electrometer.

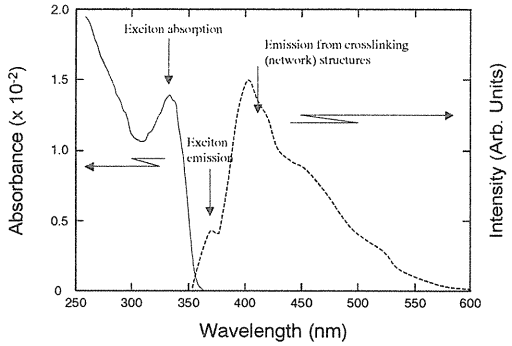

FIG. 2 Absorption and photoluminescence spectra of polysilane nanowires isolated on $SiO_{2\text{-}KOH}$. The nanowires were formed by 450 MeV Xe ion irradiation to PS1 film (250 nm thick) at 9.6 x 10^9 ions/cm^2. The irradiated specimen was developed by benzene, and re-washed at least 3 times by immersion into benzene. The photoluminescence spectrum was recorded at the excitation wavelength of 340 nm.

3. Results and Discussion

A heavy ion particle impinging on target polymers can release intermediates of high density within a limited area along the ion projectile. Its irradiation to a silicon backbone polymer causes a cross-linked reaction in an ion track and forms one cylinder-like structure (nanowire) along the single ion projectile.[9] On the basis of the LET characteristic of incident ions, a cylindrical distribution of deposited energy density ($\rho(r)$) around an ion trajectory was suggested to be given by the following formula as a function of coaxial distance from the trajectory (r),[17]

$$\rho(r) = LET_{eff}\left[\pi r^2\right]^{-1}$$
$$LET_{eff} \equiv LET\left[\ln\left(e^{1/2} r_p / r_c\right)\right]^{-1} \qquad (1)$$

where e is an exponential factor, and r_c and r_p are the radii of core and penumbra areas, respectively. The core radius is governed by the Bohr adiabatic conditions,[14] and the energy of the incident ion is mainly deposited by direct electronic excitation of the target media. Table 1 summarizes the radii of nanowires observed for a variety of molecular weights and incident ions. The radii of nanowires gradually increase with an increase in the values of LET_{eff}. Based on eq. (1), this clearly indicates that high LET values of incident ions elongate the coaxial distance at which the deposited energy density ($\rho(r)$) satisfies the threshold density required for the crosslinking reaction. Thus the single ion hitting against polysilane thin films provides the technique for producing nanowires of which the length and thickness are completely and continuously controlled.

Fig. 2 shows the absorption and photoluminescence spectra of nanowires adhered on the SiO_2 substrate. The absorption maximum at 337 nm is attributed to the transition of the exciton state in the Si backbone, clearly suggesting that σ-conjugated segments in the polysilane backbones are still present to some extent in the nanowires even after ion beam irradiation. The photoluminescence spectrum also indicates the emission from the backbone exciton states observed at 360-370 nm. The broad and intense emission band in the visible region can be assigned to the emission from the branching and/or network structure of the Si skeleton.[15-19] After the pre-formation of nanowires, the electrodes are fabricated by Pt evaporation and resist-liftoff method on the substrate over the nanowires. To

Table 1. Radii of nanowire cross section.

Ion beam	LET [eV/nm]	LET_{eff} [eV/nm]	r^a [nm]			
			PS1	PS2	PS3	PS4
500 MeV $^{197}Au^{31+}$	11600	1750	19.4	16.2	12.5	10.7
450 MeV $^{129}Xe^{23+}$	8500	1230	10.5	-	-	6.9
520 MeV $^{84}Kr^{20+}$	4100	550	9.2	-	-	6.1
175 MeV $^{40}Ar^{8+}$	2200	310	5.6	-	-	4.0

a r denotes the radius of the cross section of the nanowire formed by each ion beam. The values are estimated by sizing the half band width of the nanowire cross section.

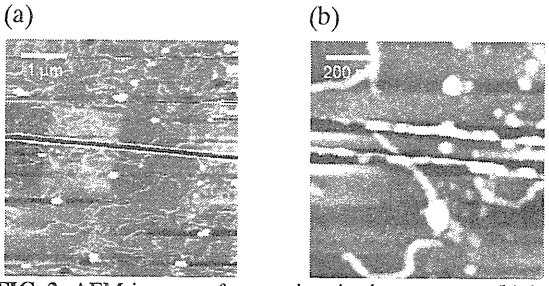

FIG. 3. AFM images of nanowires in the nanogap. (b) is an enlarged view of Fig. (a).

observe the nanowires, the thickness of electrodes is set at 20 nm. The width of the gap is clearly observed as 100 nm with high uniformity. Fig. 3 shows an AFM image of the electrode and the inside gap. Bridged nanowires were observed in the nanogap, as shown Fig. 2(b). It was confirmed that the nanowires were not severed during the liftoff process. The AFM observation also reveals the number of bridged nanowires in the entire area of the nanogap as being less than 20.

Fig. 4 shows the current-voltage (I-V) analysis of PMPS-based nanowires between the nanogap electrodes, before SEM and AFM observations. The dashed line shows the I-V curve of a nanogap with no bridged nanowire. No current is observed in the range of applied voltage, suggesting the insulating characteristics of the nanogap without bridged nanowires. The I-V curve of a Pt electrode bridged by Pt is also shown in the figure as a control. The I-V analysis of the nanowires in the gap clearly indicates intrinsic semiconductive features with the band gap of ~4.5 eV by neglecting the charge injection barriers. The band gap of polysilanes depends on the substitution patterns, and reported to be ~3.5 – 4 eV.[20,21] The

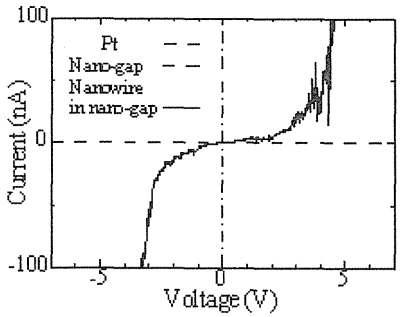

FIG. 4. Current-voltage (I-V) characteristics of PMPS based nanowires between nanogap electrodes. The nanowires were formed by 500 MeV Au ion irradiation to PS2 thin film of 400 nm thickness. The fluence of ions was 1.0×10^9 cm^{-2}.

present results are also consistent with the ion beam induced enhancement of charge transport properties.

4. Conclusion

Surface treatment of a substrate can completely control the adhesion of the nanowires. It is possible to pattern a nanowire distribution on the substrate. Nanogap platinum electrodes with 100 nm gap width are fabricated on a nanowire dispersed SiO_2 substrate by a lift-off method with electron beam lithography techniques. Both ends of the nanowire are connected to electrodes and thus the nanowires form bridges between electrodes. I-V analysis of the nanowires in the gap clearly reveals intrinsic semiconductive features based on crosslinked polysilanes.

References

1) S. Iijima: Nature 354 (1991) 56.
2) S. J. Tans, et al., Nature 386 (1997) 474.
3) M. Bockrath, et al., Science 275 (1997) 1922.
4) L. A. Harrah and J. M. Zeigler: J. Polym. Sci., Polym. Lett. Ed. 23 (1985) 209.
5) F. Kazjar, et al., J. Appl. Phys. 60 (1986) 3040.
6) R. G. Kepler, et al., Phys. Rev. B 35 (1987) 2818.
7) P. Trefonas, et al., J. Am. Chem. Soc. 107 (1985) 2737.
8) for a review, see K. Furukawa: Acc. Chem. Res. 36 (2003) 102.
9) S. Seki, et al., Adv. Mater. 13 (2001) 1663.
10) S. Seki, et al., J. Phys. Chem. B 103 (1999) 3043.
11) A. Fujii et al., Jpn. J. Appl. Phys. 34 (1995) 1365.
12) S. Seki, et al, Jpn. J. Appl. Phys. 42 (2003) 4159.
13) S. Seki, et al., Macromolecules 32 (1999) 1080.
14) J. L. Magee and A. Chattarjee: Kinetics of Nonhomogenious Processes, ed. G. R. Freeman (John Wiley & Sons, New York, 1987) Chapter 4, p. 171.
15) K. Furukawa, et al., Macromolecules 23 (1990) 3423.
16) M. Fujiki: Chem. Phys. Lett. 198 (1992) 177.
17) S. Seki, et al., Philos. Mag. B79 (1999) 1631.
18) K. Maeda, et al., J. Am. Chem. Soc. 97 (1993) 12144.
19) S. Seki, et al., Jpn. J. Appl. Phys. 36 (1997) 5361.
20) J. M. Mintmire and J. V. Ortiz: Macromolecules 21 (1988) 1989.
21) K. Takeda, et al., Phys. Rev. B 36 (1987) 8129.

3.7 Prevention of Charging Effects on TOF Secondary Ion Mass Spectra using a Cluster Ion Beam

K. Hirata[*], Y. Saitoh[**], A. Chiba[**], K. Narumi[***], Y. Kobayashi[*], Y. Ohara[**], and K. Arakawa[**]

National Institute of Advanced Industrial Science and Technology (AIST)[*]
Advanced Radiation Technology Center, JAERI, Takasaki[**]
Advanced Science Research Center, JAERI, Takasaki[***]

1. Introduction

Methods for the mass analysis of secondary ions emitted by slow and fast ion bombardments are well known as secondary ion mass spectroscopy (SIMS) and plasma desorption mass spectroscopy (PDMS), respectively. Because of the difference between the injected and emitted charges, monoatomic ion bombardment to insulators usually leads to charge accumulation on targets, which results in an increase in the absolute charging potential. The increase would change the emission energy of secondary ions and thus make their precise mass analysis difficult.

Cluster ion bombardment provides unique nonlinear irradiation effects on secondary emissions, and we found that these effects lead to a charge accumulation process that differs from the process for monoatomic ions and that the cluster ion bombardment into an organic insulator provides a lower absolute charging potential in comparison with a monoatomic ion bombardment[1]. In this study, we have applied a cluster ion beam to time-of-flight (TOF) secondary ion mass analysis of organic insulators, and compared the TOF spectra with that obtained with a monoatomic ion beam in order to investigate the effect of charging on the spectra [2].

2. Experimental

A 3 MV tandem accelerator at the Japan Atomic Energy Research Institute (JAERI) /Takasaki was used for this experiment [3-6]. A schematic diagram of the experimental arrangement is shown in Fig. 1. Pulsed 0.5MeV/atom-C_1^+ and C_8^+ beams were injected into polycarbonate films that were attached by double-sided conducting tape to a sample holder. The ion bombardments were performed at a pressure below 3×10^{-8} Torr and with an incident beam angle of 45° relative to the sample surface without charge compensation. Secondary positive ions accelerated between the target and a TOF drift tube flew a fixed distance of 0.3m in the tube before hitting a 40mm-diameter MCP. The TOF spectra recorded in a multi-channel analyzer (MCA) were transferred to a computer for off-line data handling. A fresh sample was used for each measurement.

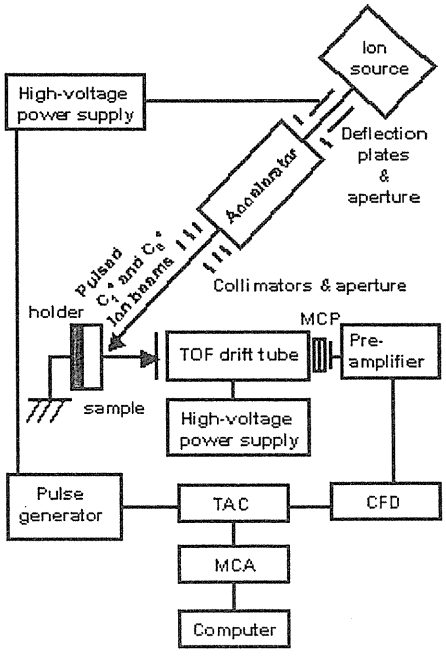

Fig. 1 Schematic illustration of the experiment set-up.

3. Results and discussion

Figures 2 and 3 show the atomic dose dependencies of the positive secondary ion TOF spectra for C_1^+ and C_8^+ bombardments, respectively. The spectra are shown in the lower mass range, which is dominated by small fragments, including hydrogen and hydrocarbon ions. We note that the positions and relative intensities of some fragments are different between Fig.2 and Fig.3. We also note that the spectrum in Fig.2 exhibits considerable peak shift and overall spectrum compression as the atomic dose increases.

Implanted ions with ~MeV order incident energy dominantly lose their kinetic energy by electronic interaction with the target and the electronic energy deposited by the implanted ion is converted to the target atomic and molecular motions. Depending strongly on the local deposited energy density, the target molecule may be fragmented and a fraction of the fragments is emitted as secondary ions. The deposited energy density at the near surface due to C_8^+ impact is larger than that due to C_1^+ impact because constituent atoms originating from the same cluster simultaneously transfer their kinetic energy to a small area of the target surface. The higher deposited energy density makes the fragmentation process for C_8^+ different from that for C_1^+; this difference provides the different positions and relative intensities of some fragments between the C_1^+ and C_8^+ impacts.

For C_1^+ bombardment, the peak shift to a smaller MCA channel and overall compression of the TOF spectrum are observed as the atomic dose increases (Fig. 2). This phenomenon is ascribed to the positive potential build-up of the ion-emission point on the target. The enhancement of the potential in going from spectrum (a) to spectrum (b) (ϕ_{eff} = 1×10^{11} atoms/cm^2) is estimated to be 0.2kV (FIG. 2b), and the corresponding enhancement to spectrum (c) (DC beam irradiation dose = 1×10^{12} atoms/cm^2) reaches as high as *ca.* 2kV (Fig. 2c).

In contrast to the C_1^+ bombardment (Fig. 2), the dose dependence of the TOF spectrum for C_8^+ does not show clear spectrum compression (Fig. 3). Although the general shape of the spectrum differs from that of Fig. 3a-b by chemical modification due to the ion bombardment, we can obtain a clear TOF spectrum even after DC beam irradiation with a dose as high as 7×10^{12} (atoms/cm^2) without charge compensation (Fig. 3c).

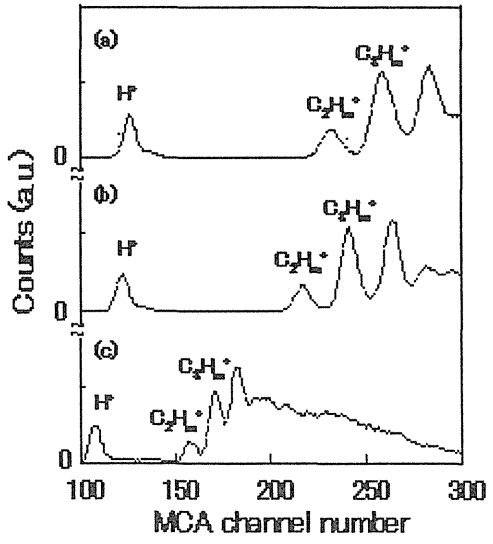

Fig.2 Positive secondary ion TOF spectra for C_1^+ bombardment. (a) ϕ_{eff} = 1×10^{10} atoms/cm^2, (b) ϕ_{eff} = 1×10^{11} atoms/cm^2, (c) DC beam irradiation dose = 1×10^{12} atoms/cm^2. The vertical axis shows ion counts in linear scale. Each channel corresponds to 0.05μs.

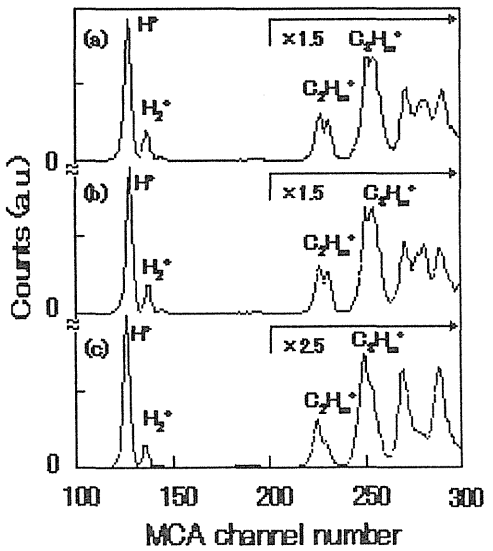

Fig.3 Positive secondary ion TOF spectra for C_8^+ bombardment. (a) ϕ_{eff} = 1×10^{10} atoms/cm^2, (b) ϕ_{eff} = 1×10^{11} atoms/cm^2, (c) DC beam irradiation dose = 7×10^{12} atoms/cm^2. The vertical axis shows ion counts in linear scale. Each channel corresponds to 0.05μs.

These results show that the potential of the ion-emission point is stable during the C_8^+ bombardment over a wide range of atomic doses. Comparison of magnified TOF spectra around H^+ and H_2^+ peaks between C_1^+ and C_8^+, with an effective dose of $\phi_{eff} \approx 1\times10^{10}$ atoms/cm^2 during the measurements (Fig. 4), reveals that the H^+ peak for C_8^+ is narrower than that for C_1^+. The narrower peak for C_8^+ enables H^+ to be clearly distinguished from the H_2^+ for C_8^+, whereas it is difficult to distinguish the corresponding peaks for C_1^+ because charging during the measurement results in continuous peak shifts and, hence, peak broadening. Therefore, the use of the cluster ion beam also has an advantage over the monoatomic ion beam in improving the resolution of the spectrum.

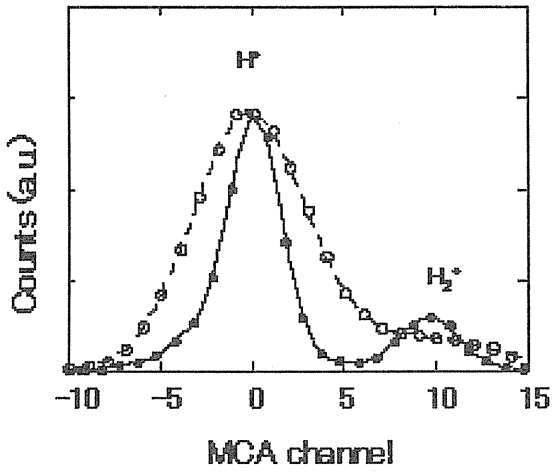

Fig.4 Magnified TOF spectra around the H^+ peak for C_1^+ and C_8^+ with an effective atomic dose of $\phi_{eff} \approx 1\times10^{10}$ atoms/cm^2 during the measurements. The spectra were arbitrarily shifted and scale-adjusted. The lines through the data points are a guide for the eyes.

In conclusion, the use of C_8^+ instead of C_1^+ as a primary ion for the secondary ion TOF measurement of PC almost completely eliminates dose-dependent peak shift and compression due to charging, both of which are observed with C_1^+ bombardment to PC. The stability of the TOF spectrum against charging in C_8^+ bombardment provides a better spectrum resolution than that obtained in C_1^+ bombardment. Mass spectroscopy using a cluster ion as a primary ion will be a promising tool for chemical analysis of materials with lower electric conductivities.

References

1) K. Hirata, S. Saitoh, K. Narumi, and Y. Kobayashi, Appl. Phys. Lett., **81**, 3669 (2002).
2) K. Hirata, Y. Saitoh, A. Chiba, K. Narumi, Y. Kobayashi, and K. Arakawa , Appl. Phys. Lett., **83**, 4872 (2003).
3) Y. Saitoh, S. Tajima, I. Takada, K. Mizuhashi, S. Uno, K. Ohkoshi, Y. Ishii, T. Kamiya, K. Yotsumoto, R. Tanaka, E. Iwamoto, Nucl. Instrum. Methods Phys. Res. B **89**, 23 (1994).
4) K. Narumi, K. Nakajima, K. Kimura, M. Mannami, Y. Saitoh, S. Yamamoto, Y. Aoki, and H, Naramoto, Nucl. Instrum. Methods Phys. Res. B **135**, 77 (1998).
5) Y. Saitoh, K. Mizuhashi, and S. Tajima, Nucl. Instrum. Methods Phys. Res. A **245**, 61 (2000).
6) K. Hirata, Y. Saitoh, K. Narumi, Y. Nakajima, and Y. Kobayashi, Nucl. Instrum. Methods. Phys. Res. B **193**, 816 (2002).

4. Inorganic Materials

4.1 Effect of Irradiation Defects on the Thermal Diffusivity of SiC and SiC/SiC Composites by He Ion Implantation

T.Taguchi*, N.Igawa*, E. Wakai** and S.Jitsukawa**
Neutron Science Research Center, JAERI/Tokai*
Department of Material Science, JAERI/Tokai**

1. Introduction

Ceramic matrix composites show excellent high temperature mechanical properties and non-catastrophic failure behavior. These materials are, therefore, attractive candidates for structural applications at high temperatures. In particular, SiC/SiC composites are expected to be used for first wall and blanket components in a fusion reactor because of low residual radioactivity. In the fusion reactor, these materials have to have high thermal diffusivity for heat exchange and reducing the thermal shock.

Under fusion conditions, He and H are produced by 14MeV neutron-induced transmutation reactions which are (n, α) and (n,p), respectively. These transmutation rates in SiC are larger than those in other candidate materials such as ferritic steels and vanadium alloys.[1] It is important to investigate He and/or H effects on the thermal and mechanical properties. In this study, we investigated the effect of He ions implantation on the thermal diffusivities of SiC and SiC/SiC composite.

2.Experimental procedure

2.1 Materials

The samples of SiC were fabricated by chemical vapor deposition (CVD) and reaction bonding (RB) process. The SiC/SiC composites were fabricated by chemical vapor infiltration (CVI) and RB process. As reinforcement, Hi-Nicalon Type S and Tyranno SA SiC fibers were used in this study. The details of fabrication procedure of SiC and SiC/SiC composites are described elsewhere[2]. Densities and porosities of these SiC and SiC/SiC composites are summarized in Table I. The specimen size was 10 mm in diameter and 0.7 mm in thickness

2.2 Measurement of thermal diffusivity and thermal conductivity

The thermal diffusivities of the specimens were measured in the temperature range from 15 to 1100℃ using a laser flash thermal diffusivity analyzer (PS-2000, Rigaku Co. Ltd., Japan) with a ruby laser of 20J in the maximum power. The transient temperature response at the rear surface of the specimen was monitored with an IR detector. The

Table I Characterization of SiC and SiC/SiC composites.

Specimen ID	Density / g/cm^3	Implanted He / appm	
CVD-SiC	2.72	26	Stoichiometric SiC
RB-SiC(10:0)	3.02	26	Residual free-Si: ~15%
RB-SiC(10:9)	3.21	9	Residual free-Si: ~40%
CVI-SiC/SiC(S)	2.56	7, 30	Hi-Nicalon Type S fiber was used
CVI-SiC/SiC(SA)	2.65	7, 30	Tyranno SA fiber was used
RB-SiC/SiC(SA)	2.65	7, 30	Tyranno SA fiber was used

thermal diffusivity, α, was obtained by $t_{1/2}$ method using the following equation:

$$\alpha = 1.388L^2/\pi^2 t_{1/2} \quad (1)$$

where $t_{1/2}$ is the time required to reach half of the total temperature rise on the rear surface of the specimen, and L is the specimen thickness.

2.3 Implantation

An irradiation apparatus was installed in Light Ion Room No.2 of cyclotron facility at TIARA. The SiC and SiC/SiC composites were irradiated by 50MeV He ions for several hours with this apparatus using an Al-foil energy degrader in order to obtain the uniform He distribution in the specimens. Figure 1 shows the depth distribution of He concentration calculated by TRIM code.[3] In this case, it assumed that the beam current density was 0.4 μ pA/cm^2 and the irradiation time is about 19 hours. This calculated result indicates that He^+ ions are implanted uniformly in the specimen toward the depth of about 760 μ m. The concentration of implanted He ions is also shown in Table I.

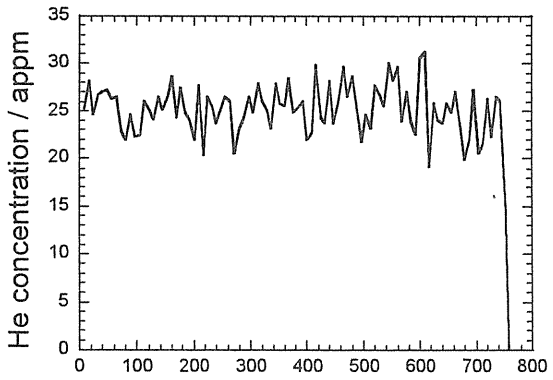

Fig.1 Depth distribution of He in SiC calculated by TRIM code.

3. Results

Although the 6 kinds of SiC and SiC/SiC composites were implanted with He ions, the result of only CVD-SiC is shown in this paper. Figure 2 shows the measured results

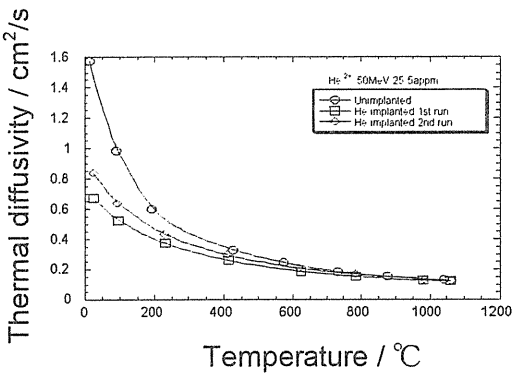

Fig.2 The thermal diffusivities of as-received CVD-SiC and He implanted CVD-SiC as functions of temperature.

of thermal diffusivities of the CVD-SiC. The thermal diffusivities of CVD-SiC decreased after implantation of He^+ ions. He atoms combine with lattice defects easily and become stable because they are not soluble in SiC. In general, the thermal conductivity of SiC is contributed to phonon-phonon scattering. The implanted He in SiC amplifies the phonon-phonon scattering. Consequently, the thermal diffusivities of He implanted specimens decreased. The thermal diffusivity of CVD-SiC measured in the 2nd run was higher than that measured in the 1st run. It is reported that He release from SiC starts at 500 ℃ and tended to increase with increasing temperature[4]. The specimen was heated up to 1100 ℃ during the 1st measurement. Therefore, the thermal diffusivity of the 2nd measurement was higher than that of 1st measurement. However, the thermal diffusivity of 2nd measurement was lower than those of as-received CVD-SiC. By annealing at temperature higher than 1100 ℃, it is expected that the thermal diffusivity of specimen recovers higher.

4. Discussion

The thermal conductivity K is calculated from the thermal diffusivity α by the following equation:

$$K = \alpha \rho C_P \quad (2)$$

where ρ is the density and C_P is the specificheat capacity at constant pressure. Because heat conduction in SiC takes place by phonon-phonon scattering, K is also given by Debye equation:

$$K=1/3 C_V V l_{thermal} \quad (3)$$

where $l_{thermal}$ is the mean free path of phonons C_V is the heat capacity per unit volume, and V is the mean phonon velocity, which we assume to be equal to the velocity of sound in SiC. And C_V is obtained by the following equation,

$$C_V = \rho C_P \quad (4)$$

In this study V is given by the following equation:

$$V=\sqrt{E/\rho} \quad (5)$$

where E is the elastic modulus of the SiC. By setting eqn(2)=eqn(3), we obtain

$$l_{thermal}=3\alpha/V \quad (6)$$

When additional phonon scattering by defects is introduced into a solid after irradiation, the mean free path is reduced from $l_{thermal}$ to l_I. The mean free path attributable to irradiation induced defects, $l_{irradiation}$, is approximated by:

$$1/l_I=1/l_{thermal}+1/l_{irradiation} \quad (7)$$

Finally, the defect concentration induced by irradiation, $X_{irradiaiton}$, is calculated from $l_{irradiaiton}$ by the following equation,

$$X_{irradiation}=M/(2\rho l_{irradiaiton}{}^3 N_A) \quad (8)$$

where M is the molecular weight of SiC and N_A is Avogadro's constant.

Figure 3 shows the $X_{irradiation}$ of CVD-SiC calculated from eqn(7) and eqn(8). The defect concentration of implanted He estimated by 1st measurement data rapidly decreased around 600 ℃. This is because the He release from SiC starts at 500 ℃. On the other hand, the defect concentration by 2nd measurement data was smaller than that by 1st measurement data and almost constant independent of temperature. The reason for this is that some part of the induced defects disappeared when the specimens were heated up to 1100℃ during the 1st measurement.

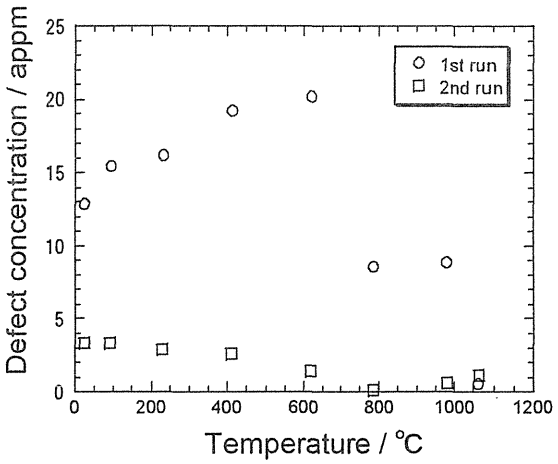

Fig.3 Relationship between defect concentration induced by irradiation and temperature.

5. Conclusion

He ion implantation effect on the thermal diffusivities of CVD-SiC was investigated. The results obtained in this study are summarized as follows:

[1] The thermal diffusivities of CVD-SiC decreased after implantation of He ions.

[2] The thermal diffusivity measured in the 2nd run was higher than that measured in the 1st run because He was released from CVD-SiC during the 1st run.

[3] The defect concentration induced by irradiation, $X_{irradiation}$, was estimated.

References

1) L.L.Snead et al., Journal of Nuclear Materials **233-237** (1996) 26-36

2) Taguchi et al., Ceramic Transactions 144 (2002) 69-76

3) J.F.Ziegler et al., The Stopping and Ranges of Ions in Matter, vol.1, Pergamon Press, New York, 1985

4) K.Sasaki, T.Yano, T.Maruyama and T.Iseki, Journal of Nuclear Materials **179-181** (1991) 407-410

4.2 Synergistic Effects of Implanted Helium and Hydrogen on the Microstructural Change of SiC/SiC Composites

T. Taguchi*, N. Igawa*, S. Miwa**, E. Wakai***, S. Jitsukawa*** and A. Hasegawa**

Neutron Science Research Center, JAERI/Tokai*

Department of Quantum Science and Energy Engineering, Tohoku University**

Department of Materials Science, JAERI/Tokai***

1. Introduction

SiC/SiC composites are being developed as structural materials for fusion power reactors in part due to their high temperature strength and low residual radioactivity after neutron irradiation. However, the effect of transmutation gasses on SiC, which are not produced in the current fission-neutron damage studies, is largely unknown. Of particular concern are the high levels of helium (He) and hydrogen (H) transmutation atoms produced by the 14.1-MeV fusion neutrons. The production rates of He and H in SiC in first wall region are approximately a gas/dpa ratio of 130 appm He/dpa and 40 appm H/dpa[1]. Irradiation-induced microstructural changes may be accelerated in SiC/SiC composites under the fusion condition since He is insoluble in virtually all materials and is captured easily within vacancy clusters produced during cascade formation.

In this study, the synergistic effect of implanted He and H atoms and the effect of irradiation temperature on microstructural change of SiC/SiC composites using near-stoichiometric SiC fiber is presented by application of simultaneous ion irradiation at 1000 and 1300 °C.

2. Experimental procedure

2.1 Materials

The 2D plane weave of Hi-Nicalon Type S and Tyranno SA SiC fiber fabrics as reinforcement were used in this study. The SiC/SiC composites were fabricated using the forced thermal gradient chemical vapor infiltration (F-CVI) process at Oak Ridge National Laboratory. The details of fabrication procedure are described elsewhere[2].

2.2 Irradiation

Simultaneous ion irradiation was carried out at TIARA (Takasaki Ion Accelerators for Advanced Radiation Application) facility of JAERI. The specimens were irradiated at 1000 or 1300 °C by 6.0 MeV Si^{2+} ions, 1.0 MeV He^{+} ions and/or 340 keV H^{+} ions. Various combinations of ions were examined in this study as summarized in Table 1. The implantation of He^{+} and H^{+} ions was conducted using an aluminum foil energy degrader in order to control He and H distribution in the depth range of about 1.0-1.8 . m from the specimen surface. The displacement damage, He, H and Si concentration as a function of depth from the surface in SiC calculated by TRIM code[3] is shown in Fig. 1.

Table 1 Irradiation condition of simultaneous ion-beams in this study.

Condition ID	Kinds of ions	Displacement damage (DPA)	He concentration (appm)	H concentration (appm)
Single (Si)	Si^{2+}	10	0	0
Single (He)	He^{+}	~0	1300	0
Dual	Si^{2+}+He^{+}	10	1300	0
Triple	Si^{2+}+He^{+}+H^{+}	10	1300	400
Triple (Hx10)	Si^{2+}+He^{+}+H^{+}	10	1300	4000

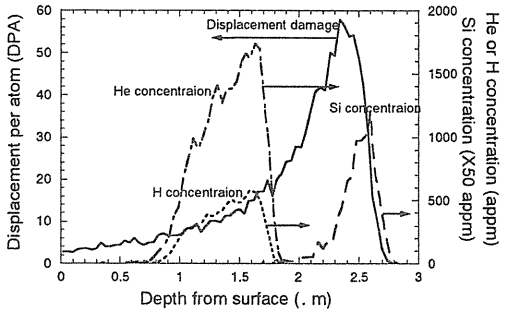

Fig. 1. Displacement damage, He, H and Si concentration as a function of depth from the surface in SiC calculated by TRIM code

3. Results and discussion

Cross-sectional TEM microphotographs of the irradiated SiC matrices at about 1.4 . m depth from the surface are given in Fig. 2. The average size, average number density and formation position of He bubbles in the matrix is summarized in Table 2. For implantation at 1000 °C, He bubbles are not observed in the matrix irradiated by single Si ions or single He ions. However, He bubbles were observed in the matrix irradiated under dual (Si+He) or triple (Si+He+H) ion-beams. These results reveal that the simultaneous ion-beams irradiation enhances the formation of stable He clusters. It is thought that this is caused by the simultaneous formation of vacancies by the silicon ion damage that are stabilized in the presence of helium. Once stable vacancy clusters are formed they continue to add helium leading to the helium bubbles observed. These He bubbles were preferentially formed at the grain boundaries. The average size of He bubbles decreased with increasing amount of implanted H ions. On the other hand, the number density of He bubbles slightly increased with increasing the amount of implanted H ions. These results indicate that the simultaneously implanted H might prevent the migration of He and the growth of He bubbles might be inhibited. Hojou has reported that H atoms implanted simultaneously with He atoms would contribute to forming a large number of nuclei for bubbles formation at room temperature by in-situ TEM observation technique[4]. The result in this study is corresponding to this previous work.

At irradiation temperature of 1300 °C, He bubbles were observed in the matrix irradiated by single He ions, dual and triple ion-beams. Hasegawa has reported that He bubbles were formed in He pre-implanted matrix of SiC/SiC composite annealed at 1400 °C for 1 hour[5]. Such voids (average size: 5.8 nm) were also observed in the matrix irradiated by single Si ions although gas atoms such as He and H were not implanted. Price reported that neutron irradiation at 1250 °C produces voids in . -SiC and the average size of voids was 4.2 nm[6]. The results in this study are in good agreement with the previous studies. Helium bubbles in the matrix irradiated by single He ions and the voids were mainly formed at grain boundary. Helium bubbles in the matrix irradiated by dual and triple ion-beams were formed both at

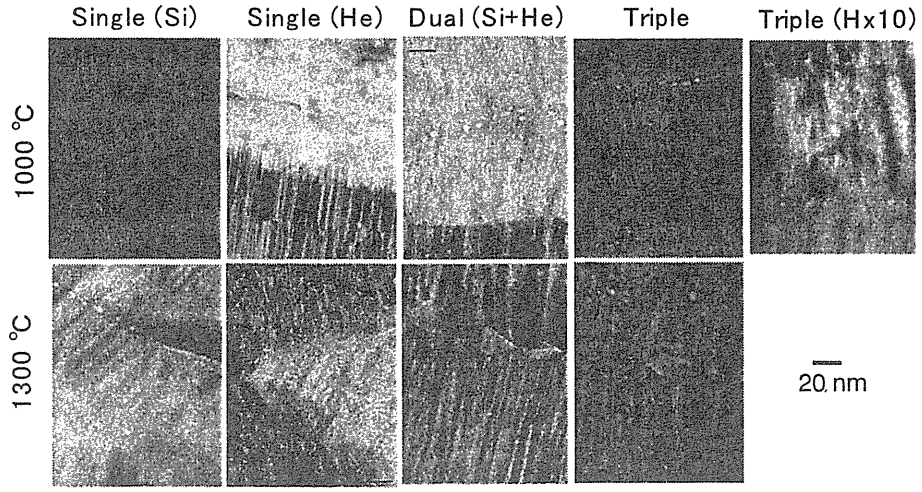

Fig. 2. Cross-sectional TEM microphotographs of the irradiated SiC matrices at about 1.4 μm depth from the surface.

grain boundary and within the grain. The average size of He bubbles at the grain boundary was much larger than that in the grain. The reason is that the recombination of He clusters was accelerated since the mobility of He interstitial and vacancy at grain boundary is larger than that in the grain.

Both average size and number density of He bubbles increased with increased irradiation temperature (Table 2). He bubbles formed at irradiation temperature of 1000 °C were observed only in the He implanted region (0.7-1.8 . m from the surface). On the other hand, He bubbles at 1300 °C were also observed outside of He implanted region; the formation depth-range of He bubbles was from 0-3.0 . m. The mobility of He interstitial and induced vacancy was increased with increasing the irradiation temperature. Therefore, He bubbles grew easily and the number of visible He bubbles was increased at higher temperature.

Table. 2 The average size, average number density and formation position of He bubbles in the matrix

Irradiation temperature (.C)	Condition ID	Single (Si)	Single (He)	Dual (Si + He)	Triple	Triple (X10 H)
	Position	Average size (nm)				
1000	Grain boundary	----------	----------	4.9	4.6	2.7
	Grain interior	----------	----------	----------	----------	----------
	Density (m^{-3})	0	0	$1.61x10^{22}$	$2.51x10^{22}$	$2.75x10^{22}$
1300	Grain boundary	5.8	2.3	23.2	20.9	Not examined
	Grain interior	----------	----------	4.1	3.9	Not examined
	Density (m^{-3})	Not measured	Not measured	$5.92x10^{22}$	$7.22x10^{22}$	Not examined

4. Conclusions

(1) At the irradiation temperature of 1000 °C, He bubbles were not observed in the matrix irradiated by single Si ions or single He ions while He bubbles were observed in the matrix irradiated by dual or triple ion-beams. Simultaneous existence of the induced vacancies by Si ion beam and implanted He ions contributed to the formation of He bubbles.

(2) The average size of He bubbles in the matrix decreases with increasing density of implanted H ions. The number density of He bubbles increases when the implantation temperature is increased from 1000 to 1300°C and the amount of implanted H is increased.

(3) At the irradiation temperature of 1000 °C, He bubbles in the matrix were mainly formed near the grain boundary. At the irradiation temperature of 1300 °C, He bubbles in the matrix were formed both at grain boundary and within the grains. The average size of He bubbles at grain boundary was much larger than that near the grain.

References:

1) L.L. Snead, R.H. Jones, A. Kohyama, P. Fenici, J. Nucl. Mater. 233-237 (1996) 26.
2) T. Taguchi, N. Igawa, S. Jitsukawa, T. Nozawa, Y. Katoh, A. Kohyama, L. L. Snead, J. C. McLaughlin, Ceram. Trans. 144 (2002) 69.
3) J. F. Ziegler, J. P. Biersack, U. Littmark, The Stopping and Ranges of Ions in Matter, vol. 1, Pergamon Press, New York, 1985.
4) K. Hojou, S. Furuno, K. N. Kushita, H. Otsu, K. Izui, Nucl. Instr. and Meth. in Phys. Res. B 91 (1994) 534.
5) A. Hasegawa, M. Saito, S. Nogami, K. Abe, R. H. Jones, H. Takahashi, J. Nucl. Mater. 264 (1999) 355.
6) R. J. Price, J. Nucl. Mater. 48 (1973) 47.

4.3 Extra Radiation Hardening and Microstructural Evolution in F82H by High-dose Dual Ion Irradiation

M. Ando*, E. Wakai**, T. Sawai**,S. Matsukawa* A. Naito**,
S.Jitsukawa**, K. Oka***, T. Tanaka*** and S. Ohnuki***

Department of Fusion Engineering Research, JAERI*
Department of Materials Science, JAERI**
Graduate School of Engineering, Hokkaido University***

1. Introduction

Reduced activation ferritic/martensitic steel (RAFs) is the most promising candidate for the blanket structural material in fusion reactor. Radiation embrittlement caused by irradiation at lower temperatures (<673 K) would affect their service life[1]. Neutron irradiation data suggest that the shift of ductile brittle transition temperature (DBTT) seems to saturate at higher doses, although high dose data are very limited. Furthermore, the effect of transmutation helium on radiation embrittlement in RAFs is also an important subject[2,3]. Advantages of multi-ion irradiation experiments include that high dose irradiation up to ~ 100dpa can be easily achieved and that the ratio of displacement damage and helium production can be controlled during irradiation[4]. The positive correlation is generally observed between radiation hardening and radiation embrittlement in ferritic/martensitic steels by neutron irradiation data. Radiation hardening by ion-irradiation can be evaluated by an ultra micro-indentation technique, systematically[5].

The objectives of this study are to evaluate radiation hardening on ion-irradiated F82H up to 100 dpa and to examine the extra component of radiation hardening due to implanted helium atoms (up to ~3000 appmHe) in F82H under ratio of 0, 10, 100 appmHe/dpa.

2.Experimental procedure

2.1 Materials and preparation

The material used in this study was reduced activation ferritic/martensitic steel (F82H; Fe-8Cr-2W-0.2V-0.04Ta-0.1C). The heat treatment was normalized at 1313 K for 0.5 hr and tempered at temperatures of 1023 (denoted as Std) and 1073 (denoted as HT) K for 1 hr.

2.2 Ion Irradiation

Small coupons specimens (6 x 3 x 0.8 mm) were irradiated in the TIARA facility by 10.5 MeV Fe^{3+} ions with/without 1.05 MeV He^{+} ions. He^{+} ion implantation was performed with using aluminum foil energy degrader in order to control helium distribution in the depth range of about 0.5~1.3 μm from the specimen surface. Further details of irradiation system are described elsewhere[6]. The irradiation was performed to 3.3-100 dpa at the depth of 0.6 μm and the damage rate was about $1.0x10^{-3}$ dpa/s at this depth. The deformation depth due to micro-indentation reaches up to 4-5 times larger than the indentation depth[5]. The nominal damage level in this study is expressed as the damage at 600 nm, which is 1.5 times of indentation depth.

2.3 Micro-indentation hardness

Micro-indentation tests were performed at loads to penetrate about 0.40 μm in the irradiated specimens using an UMIS-2000 (CSIRO, Australia). The micro-hardness showed

the average of 35 measurements per an irradiated specimen. The direction of indentation was chosen to be parallel to the ion beam axis.

2.4 Microstructure observation

Irradiated specimens were made into thin films, with a Hitachi FB-2000A focused ion beam (FIB) processing instrument with a micro-sampling system. The foils were made so that they included the ion-beam axis or normal to the irradiated surface. The microstructural examination was carried out using a JEOL JEM-2000FX transmission electron microscope (TEM) operating at 200 kV.

3. Results and discussion

3.1 Radiation hardening by high-dose irradiation

Fig. 1 shows the dose dependence of radiation hardening in F82H (Fe^{3+} single ion irradiation). Micro-hardness tends to increase with displacement damage up to about 30 dpa at 633 K. The increment in radiation hardening of F82H from 50 to 100 dpa was much smaller than that of from 0 to 50 dpa. This tendency of dose dependence up to 30 dpa agrees approximately with the results of yield stress (σ_y) about F82H irradiated at HFIR.

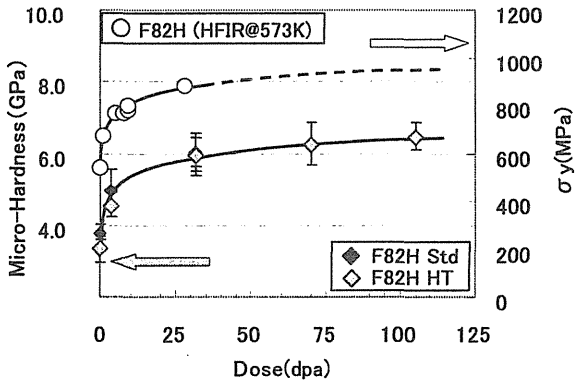

Fig. 1. Dose dependence of radiation hardening at 633 K (Fe^{3+} single ion irradiation). Radiation hardening data of neutron –irradiated F82H is also shown for comparison.

3.2 Extra component of radiation hardening by helium

Fig. 2 shows the extra component of hardening due to helium and displacement damage. For the dual (10 appmHe/dpa) ion-irradiated F82H at 633 K, the extra component of radiation hardening due to helium was a hardly detectable with helium content less than 500 appm. However, the extra hardening due to helium was caused by more than 1000 appm. Moreover, at 100 appmHe/dpa (~3300 appmHe; at 0.6 μm from surface), the extra hardening about 20 % is obviously caused by implanted helium atoms in F82H (Std) and (HT). Fig. 3a)-c) shows the cross-sectional TEM images in the single/dual irradiated F82H. The microstructures for the single/dual (10 appmHe/dpa) ion beam irradiated specimens consisted of similar fine interstitial loops and defect clusters at 50 dpa (the depth of 1.0 μm) and no cavities were observed. However, in the dual-beam (100 appmHe/dpa) irradiated

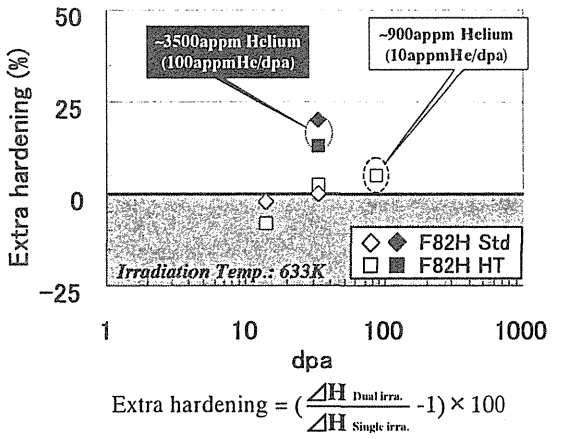

Fig. 2. Relationship between extra hardening due to helium and displacement damage

microstructure, Nano-cavities and fine defects were observed. It is suggested that the formation of nano-cavities causes an extra radiation hardening by higher He/dpa. Similar results of the extra-hardening due to helium are also reported in references[7,8].

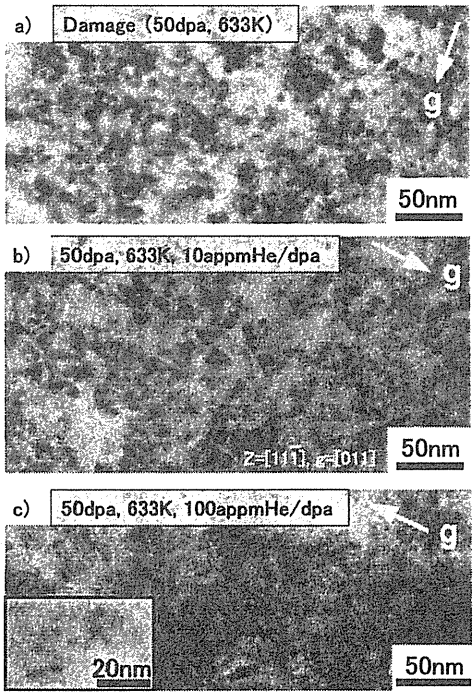

Fig. 3. Cross-sectional TEM bright field images in the single/dual ion-irradiatied F82H HT (633K, 50dpa)

4. Conclusions

1] As a result of the single irradiated F82H (Std), the micro-hardness tended to increase about 30 dpa.

2] The extra radiation hardening was obviously caused by co-implanted helium atoms more than 1000 appm in F82H irradiated at 633 K.

3] In the dual-beam (100 appmHe/dpa) irradiated microstructure, nano-cavities and fine defects were observed. It is suggested that the formation of nano-cavities causes the extra radiation hardening by helium co-implantation.

References

1) A. Hishinuma, A. Kohyama, R. L. Klueh, D. S. Gelles, W. Dietz, K. Ehrlich, J. Nucl. Mater. 258-263(1998)193-204.

2) M. Rieth, B. Dafferner, H. D. Rouhrig, J. Nucl. Mater. 258-263(1998)1147-1152.

3) E. I. Materna-Morris, M. Rieth, K. Ehrich, Effects of Radiation on Materials, STP1366, p.597.

4) E. Wakai, T. Sawai, K. Furuya, A. Naito, T. Aruga, K. Kikuchi, S. Yamashita, S. Ohnuki, S. Yamamoto, H. Naramoto, S. Jitsukawa, J. Nucl. Mater. 307-311(2002)278-282.

5) M. Ando, H. Tanigawa, S. Jitsukawa, T. Sawai, Y. Katoh, A. Kohyama, K. Nakamura, H. Takeuchi, J. Nucl. Mater. 307-311(2002)260-265.

6) E. Wakai et. al., JAERI-Review 2001-039 "TIARA Annual Report 2000" p.141.

7) P. Jung, J. Henry, J. Chen, J-C. Brachet, J. Nucl. Mater., 318(2003)241.

8) J. Henry, M.-H. Mathon, P. Jung, J. Nucl. Mater., 318(2003)249.

4.4 Mechanical Properties of Austenitic Stainless Steel Ion-irradiated under External Stress

I.Ioka*, M.Futakawa*, A.Naito**, Y.Nanjyo*, T.Suzuki*, K.Kiuchi* and T.Naoe***
Department of Nuclear Energy System, JAERI*
Department of Materials Science, JAERI**
Graduate School of Ibaraki University***

1. Introduction

Irradiation creep has been studied extensively to provide data that can be used for component analysis of fusion, fast breeder and light water reactors. It is now generally recognized that the irradiation creep data were in agreement with an empirical equation[1]. Moreover, there have been many irradiation experiments done under applied stress to investigate stress effects on microstructural evolution. It is reported that the total nucleation rate of Frank loops was increased with increasing external stress[2]. However, there are few studies on the effect of external stress on mechanical properties of the material under irradiation.

Triple ion beam irradiation can simulate the neutron irradiation environment by producing displacement damage in the material while simultaneously implanting H and He. However, the ion-irradiated area is limited to the very shallow surface layer (<2μm depth) of the specimen so that the irradiation damage is distributed in a thin layer. Hence, a nanoindentation technique combined with inverse analysis using a finite element method (FEM) was applied to examine the influence of ion irradiation on the mechanical properties of the thin layer and derive the constitutive equation of the damaged layer[3]. The purpose of this study is to evaluate the mechanical properties of the irradiated material under external stress.

2. Experimental procedure

The material tested is type 304 stainless steel in the solution-annealed condition. The chemical composition is given in Table 1. The configuration of the specimen and the ion irradiation holder for applying the required stress are shown in Fig. 1. The thickness of specimen is about 0.2mm. The specimen has three different cross-sections (1.5mm, 1.75mm, 2.0mm in width) to be irradiated under different stresses at the same time. The surface of specimen was polished with #2400 sand paper and then electrochemically polished. The spring was used to apply the required stress to the specimen during irradiation. The strain gauge was attached on L part (2.0mm in width) of the specimen to measure the tensile strain before ion-irradiation. The spring was adjusted so that the tensile strain at L part may become about 0.2%. The applied stress, about 200MPa, at L part was estimated from the stress-strain curve of type 304SS. In this time, the applied stresses of M part (1.75mm in width) and S part (1.5mm in width) were calculated to be about 228MPa and 266MPa, respectiveliy. The strains of S and M parts were estimated from strain-stress curve to be about 1% and 0.5%, respectively. The strain gauge was removed before irradiation.

The electrochemically polished specimens were irradiated in triple (12MeV Ni^{3+}, 1.1MeV He^{+} and 380keV H^{+}) ion beam mode at a temperature of 300°C using the triple ion beam facility (TIARA) at JAERI. The temperature of

the specimen was measured by an infrared thermometer(THERMAL VISION, Nikon Co.). The temperature of the spring was lower than 50°C during irradiation at 300°C. It was believed that the stress applied to the specimen was maintained during irradiation. The displacement damage in the specimen was mainly attributed to Ni^{3+} ion irradiation. The peak dose was about 10dpa at around 2μm from the surface. The He^{+} and H^{+} ions were implanted in depth ranges from 1.0 to 1.5μm using an aluminum foil energy degrader. The concentration of He and H atoms in the implanted range were 11 appmHe and 91 appmH, which correspond to LWR condition. The dose was about 5dpa in the implanted range of He^{+} and H^{+} ions.

The nanoindentation test was carried out on the surfaces of the irradiated and unirradiated specimens at room temperature. A conical indenter that has a hemispherical apex with radius of 1.2μm was used. A DUH-200 (Shimadzu Co.) testing machine was used for the nanoindentation test. The load was applied with a loading speed of 2.6×10^{-3} N/s, held for 1 second and then removed. During loading and unloading, the load was continuously monitored along with the displacement with a resolution of 19.6mN and 0.01μm, respectively.

The interaction between the irradiated thin layer and substrate (unirradiated region) complicates the deformation under the indenter and makes it difficult to characterize the irradiated thin layer. An inverse analysis was carried out using an explicit FEM code which enables us to roughly analyze a large deformation that accompanys contacting behavior. In the analysis, the indenter and specimen were treated as axisymmetric two-dimensional bodies to improve the efficiency of the calculation. The indenters were modeled as a perfectly rigid. The fineness of the mesh size is determined by the required accuracy. The minimum element size of 0.05μm is near the apex contacting zone.

The constitutive equation of the material employed in the model was assumed to be a simple power-law which is generally believed to be applicable to normal metallic materials as follows:

$$\sigma = E\varepsilon \qquad \sigma \le \sigma_y \tag{1}$$

$$\sigma = A(\varepsilon_0 + \varepsilon)^n \tag{2}$$

$$\varepsilon_0 = (\sigma_y / A)^{1/n} - (\sigma_y / E) \qquad \sigma > \sigma_y \tag{3}$$

where σ is true stress, ε true strain, E Young's modulus, σ_y yield stress, A work hardening coefficient and n work hardening exponent. Therefore, we have to identify the following material constants; σ_y, A and n through the inverse analysis on the L-D curve. The inverse analysis method is described in detail elsewhere[3].

3. Results and discussion

Figure 2 shows the Load-Depth(L-D) curves measured using the conical indenter, and the calculated results using the material constants given in Eqs (1)-(3) calculated by the inverse analysis method on the L-D curve. The calculated L-D curves agree well with the experimental ones as shown in Fig.2. The material constants estimated from the inverse analyses on the L-D curves of the stressed and stress-free irradiated specimens are summarized in Table 2. The results of analysis for an unirradiated specimen are also shown in Table 2. It seems that the difference in the yield stress of the stressed and stress-free irradiated specimen is not remarkable considering the difference in the calculated and experimental yield stresses of the unirradiated specimen. The values of A and n are the same for both specimens. The value of n corresponds to uniform deformation of the material. So, it seems that the ductility loss of

the irradiated specimens with or without applied stress is the same.

The constitutive equations identified for the irradiated layer with or without applied stress were used for the FEM analysis to obtain the stress-strain relationship. A two dimensional axisymmetric model as shown in Fig.3 was used for the analysis. The model has a high mesh density around the center of the specimen. The deformation of the specimen was calculated by the FEM code. Figure 3 shows the calculated nominal stress-strain curves of the irradiated specimen with or without applied stress. The analytical results indicated irradiation hardening and ductility loss from the very shallow irradiated layer. It is considered that there is little influence of applied stress on yield stress and nominal stress-strain curve of the irradiated specimen in this test condition.

4. Summary

From the inverse analytical results, there is little influence of applied stress on yield stress and nominal stress-strain curve of the irradiated specimen in this test condition.

References

1) F.A.Garner, M.B.Toloczko, J. Nucl. Mater. 251(1997)252.
2) H.Tanigawa. Y.Katoh, A.Kohyama, Nucl. Instru. and Methods in Phy. Resea. B 102(1995)151.
3) I.Ioka, M.Futakawa, Y.Nabjyo, T.Suzuki, K.Kiuchi, JAERI-Review 2002-35(2002)149.

Table 1 Chemical Composition of the Material in wt%

Materials	Fe	C	Si	Mn	Cr	Ni
Type 304SS	bal.	0.063	0.49	1.45	18.72	10.27

Table 2 Material constants estimated from the inverse analyses of irradiated layer with or without external stress

	Irradiated		Unirradiated
	Stress-free	Stressed	Stress-free
σ_y (MPa)	540	620	190
A(MPa)	1410	1350	1410
n	0.21	0.20	0.41

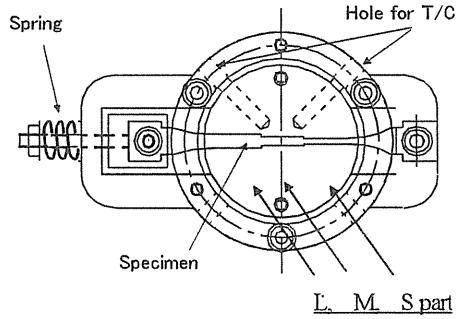

Fig. 1 Configuration of the specimen and the ion irradiation holder

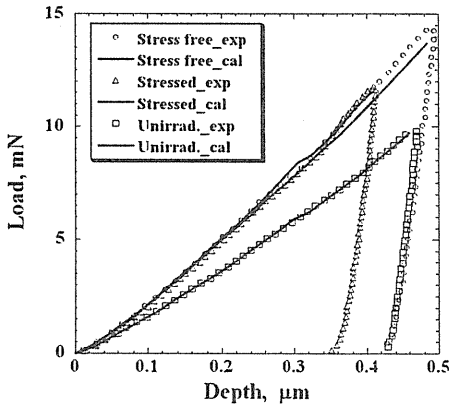

Fig.2 L-D curves measured and calculated results using the inverse analysis

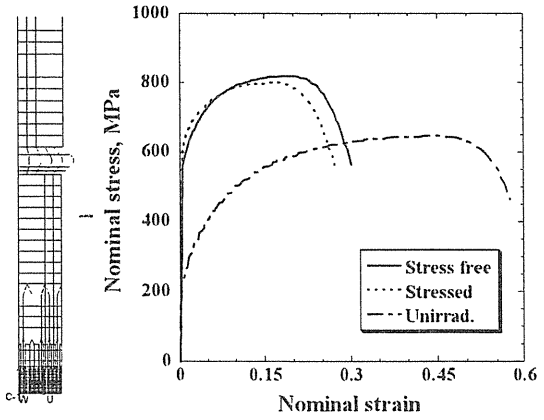

Fig.3 Calculated nominal stress-strain curves of the stressed and stress-free irradiated specimens

4.5 Effect of Ion Irradiation on Mechanical Property of Surface Treated Materials for Mercury Target

M.Futakawa*, A.Naito**, Y. Ioka** and Y. Kogawa*
Center for proton accelerator facilities, JAERI*
Department of Nuclear Energy System, JAERI**

1. Introduction

A MW-scale target that is being constructed in J-PARC (Japan Proton Accelerator Research Complex) can produce a high-intensity neutron beam by the spallation reaction due to accelerated protons impinging on the target material. A liquid-mercury target system for the MW-scale target will be installed to take advantages of self-circulating heat removal and neutron yield in the liquid mercury.

The proton beam with 1 μs pulse duration is injected into the mercury through the beam window at 25 Hz. The moment the proton beam hits the target vessel, stress waves will be imposed on the beam window and pressure waves will be generated in the mercury by the thermally shocked heat deposition. The pressure waves travel from the mercury to the vessel wall and the reflected waves propagate back. Stress waves are excited by the pressure wave propagating in the vessel wall. The resulted dynamic stress distribution in the vessel becomes very complicated. Provided that the negative pressure causes cavitation in the mercury, the following collapse of the cavitation bubbles generates microjets and/or shock waves forming pits on the surface of the vessel wall. This cavitation erosion damage was observed in off-line tests using mechanically imposed pressure wave and for in-beam tests using protons. This cavitation erosion damage accumulates on the surface of the vessel wall, compromising the structural integrity and reducing the life of the vessel.

Futakawa, et al. have carried out evaluation tests of cavitation erosion damage by using SHPB (Split Hopkinson Pressure Bar) [1,2] and MIMTM (Magnetic IMpact Testing Machine) [3]. Through these tests, it was found that surface hardening treatments such as nitriding and carburizing are useful to suppress the damage. Additionally, irradiation damage is another issue for the structural integrity and the life estimation of the target, since the target window will be irradiated by neutrons and protons. There has been, however, no data on the effect of irradiation on surface hardening treated steels under spallation condition. Hence, in order to investigate the irradiation effect on surface hardening treated 316SS (the candidate window material), triple ion beam irradiation tests using H^+, He^+ and Ni^{3+} were carried out. The changes of mechanical properties and microstructure due to irradiation were evaluated by microhardness.

2. Experimental

The specimens are prepared from reference 316SS materials (As-received and 50% cold worked) with and without carburizing: Kolsterising, which is a registered trademark of Bodycote International plc. and nitriding surface-hardening treatments. In the case of nitriding, the specimens were nitrided for 60 min at 853 K using a gas mixture of NH_3 and NH_4Cl in a pit-type gas nitriding furnace. Vickers hardness is ca 250 Hv and ca 500 Hv for as-received and 50% cold worked 316SS and ca 1000 Hv and ca 1200 Hv for those hardened by Kolsterising and nitriding treatments, respectively. The hardness is one of material key factors to reduce the pitting damage [2].

Irradiation was carried out on the cross-section of the specimen including the surface hardening treated layer at 473 K with a triple ion

beam of 12 MeV Ni^{3+}, the degraded 1.1 MeV He^{+} and the degraded 380 keV H^{+} using the Takasaki Ion Accelerators for Advanced Radiation Application (TIARA) facilities at JAERI.

The SRIM-2000 code was used to compute the displacement dose and the implanted ion concentration as a function of depth beneath the specimen surface, assuming a displacement energy of 40 eV. The peak dose depth was around 2 μm. The ranges of implanted helium and hydrogen ions were controlled so that the effect of implanted nickel ions could be neglected. At the depth of approximately 1.0 μm in the specimen, the dose was 10 dpa and the He/dpa and H/dpa ratios were about 200 and 2000 appm/dpa, respectively.

Microhardness was evaluated from the load and depth (L/D) curve measured by the instrumented indenter machine (Shimadzu DUH-200). The maximum imposed indent load and loading rate are 30 mN and 0.2 mN/s, respectively. The micro hardness Hu was evaluated by using the following equation :

$$Hu=P_{max}/26.43h_{max} \qquad (1)$$

Here, h_{max} is the maximum depth at the imposed maximum load P_{max}. The L/D curve was measured 10 times at each distance from the surface.

3. Results and Discussion

Figure 1 shows typical results of load and depth curves obtained from Kolsterised as-received 316SS. It was found that the L/D curves of the hardening layer were hardly affected by the ion irradiation although those of the substrate significantly changed. That is, the maximum depth h_{max} of the substrate without irradiation reached 0.7 μm under the maximum load of 3 mN while the h_{max} with irradiation is 0.5 μm. The dpa distribution along the depth is present within the depth of 2.2 μm, according to the SRIM calculation. The measured hardness is influenced by that of the surface layer with 7 times thickness of the measured depth [4]. The decrease of the h_{max} represents the irradiation hardening of the surface layer with the thickness up to 3.5 μm at least.

The microhardness distributions along the distance from surface, which are evaluated by using Eq. (1) with h_{max} obtained form the L/D curves, are shown in Figure 2 for both the unirradiated and irradiated area of the nitrided and the Kolsterised specimens. The nitriding treatment hardened the surface layer up to the distance of nearly 35 μm from the surface, and the Kolsterising treatment hardened that up to the distance of nearly 30 μm. The hardness of the hardening layers was hardly affected by the irradiation, while that of the substrates was significantly increased for the as-received one.

High compressive stress is distributed in the surface treated layers by carburizing and nitriding because they have larger specific volume compared with the substrates. It is considered that hardening mechanisms of the treated layers are based on those lattice distortions and especially in the case of nitriding, the generation of the quite fine nitrides such as CrN, Fe_3N and Fe_4N with high number density, and the lattice distortions and the

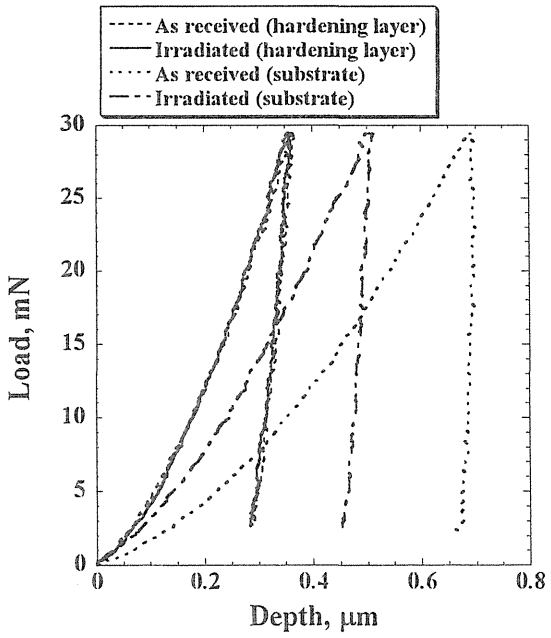

Fig.1 Measured load and depth curve in the Kolsterised as-received 316SS.

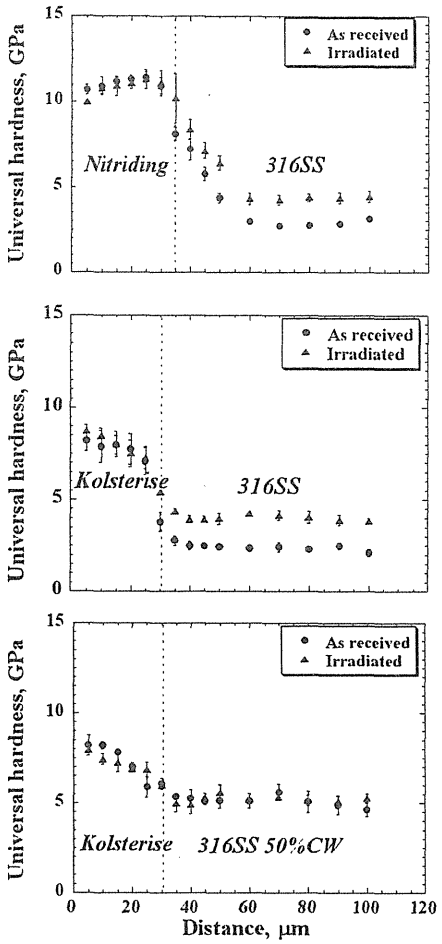

Fig.2 Hardness distribution along distance from the surface of hardening treated specimens

formation of the martensitic phases with extremely high dislocation density.

It is reported that the stress relaxation given by the ratio of instantaneous stress to initial stress was approximately 0.5 for the 316 and 316L SS neutron-irradiated to 1 dpa at ranging from 288 to 370 °C in the EBR-II [5] and the JMTR[6] or by calculation[5,7]. In the irradiated hardening treated layers, the increase in hardness due to the formation of defect clusters and the decrease in hardness accompanying the relaxation of residual compressive stress were considered to be complexly occurred as irradiation effects. In the results, the effect of irradiation relaxation can be ignored since the hardness of hardening treated layers was hardly changed by irradiation.

4. Summary

In order to investigate the irradiation effect on the surface hardening treated 316SS: the candidate window material, triple ion beams irradiation test using H^+, He^+, Ni^{3+} was carried out, taking account of the target spallation condition. The changes of mechanical properties and microstructure due to irradiation were evaluated by the microindentation technique. As a result, the distinguished change was hardly observed on the surface hardening treated layers of 316SS. In the future work, the microstructure investigation will be carried out.

References

1) Futakawa M., Kogawa H. and Hino R. ,Measurement of dynamic response of liquid metal subjected to uniaxial strain wave, J. Phys. IV France 10 Pr9-237-242(2000).

2) Futakawa M., Kogawa K., Hino R., Date H. and Takeishi H., Erosion damage on solid boundaries in contact with liquid metals by impulsive pressure injection, Int J. Imp. Eng. 28 123-135 (2003).

3) M. Futakawa, T. Naoe, H. Kogawa, C.C. Tsai, Y. Ikeda: Pitting damage formation up to over 10 million cycles –Off-line test by MIMTM-, J. Nucl. Sci. Tech. Vol.40 No.11,2003, 895-904.

4) M. Futakawa, T. Wakui, I. Ioka, M. Eto, Mechanical-property evaluation of thin corroded surface layers of ceramic materials by the microindentation technique, J. Euro. Ceram. Society 20(2000), 1135-1143.

5) J.P. Foster, E.R. Gilbert, K. Bunde, D.L. Porter, J. Nucl. Mater. 252 (1998) 89.

6) Y. Kaji, Y. Miwa, T. Tsukada, M. Kikuchi, S. Kita, M. Yonekawa, J. Nakano, H. Tsuji, H. Nakajima, J. Nucl. Mater. 307-311 (2002) 331.

7) J. Nagakawa, J. Nucl. Mater. 212-215 (1994) 541.

4.6 Change in Cr at Grain Boundary of the Advanced Fuel Cladding Material with Triple Ion Irradiation

Y.Nanjo*, I.Ioka*, A.Naito*, H.Yamamoto**, K.Kiuchi*
K.Fujimura*** and H.Obata***
Department of Nuclear Energy System, JAERI*
Nuclear Science Research Center, JAERI**
Japan Atomic Power Company***

1. Introduction

The advanced fuel cladding material, adapted to the 100GWd/t of ultra high burn-up extension with Mixed Oxide (MOX) fuel, is developed on the view points of the radioactive waste reduction, Pu effectual utilization and improvement of economical efficiency. A stabilized austenitic stainless steel with high Cr concentration and high gamma phase stabilization, Fe-25Cr-35Ni, has been adopted for the candidate. The ultra high purification and the strain aged recrystallization (SAR) were made during the machining process for obtaining the fine grain and uniformly dispersed precipitates, which are countermeasures against popular problems such as Intergranular Stress Corrosion Cracking (IGSCC) or ductility loss.

For evaluating the change in Cr concentration at the grain boundary which is an index for the susceptibility of IGSCC, the candidates and comparisons were irradiated with triple ion beams of Ni^{3+}, He^{+} and H^{+} which simulates the ultra high burn-up extension condition. Then dose dependence and composition dependence of the Cr depletion for the candidates and comparisons were measured.

2. Experimental

2.1 Alloys

Two types of the candidates (prototype tube and flat plate) and three types of the comparisons (304SS for Mutsu cladding tube, 316SS flat plate and Fe-25Cr-20Ni flat plate) were used in this study. Chemical composition of the candidates and comparisons is shown in Table 1.

The prototype tube of the candidate was made through vacuum induction melting (VIM) and cold crucible induction melting (CCIM) methods. The flat plates of the candidate and Fe-25Cr-20Ni alloy were made through VIM and electron beam melting (EB) methods. Both of the candidate and Fe-25Cr-20Ni alloy were ultra high purity grade with impurities of C, N and O of total 50ppm.

The prototype tube of the candidate was produced through the SAR process and stretch forming process. SAR process consisted of the 60% cold work with extruding and continuous two heat treatments. The first heat treatment is aging at 873 K for 15 hours to uniformly stabilize impurities as precipitations, and the second one is recrystallization at 1048 K for 10 hours to obtain fine grain. After SAR process, the tube was moved into stretch forming process, corresponding to 7% cold work, for obtaining sufficient strength and straightening.

Mutsu cladding tube was produced through the normal tube fabrication process with 12~15 % cold work.

The flat plates of candidate and other comparisons were used after solution treatment at 1323 K for 1 hour.

2.2 Irradiation sample

The sample for irradiation was the disk of 3mm in diameter, and cut out from each material. If the disks were cut from tube type material, the flat surface was obtained on the outside of the tube by wet polishing with silicon carbon paper,

and the pre-disk was taken from the flat surface with slurry drill core cutter. The curved surface of the pre-disk was wet polished. In flat plate type material, sheets of 0.5 mm in thickness were cut, and the disks were cut from the sheets with electro polishing, in which the mixed acid (sulfuric acid : phosphoric acid = 2:3) was used, at 333-343K about 1 hour. The disks were wet polished to 0.2 mm in thickness. The irradiation side was buff-polished, and then electro-chemically polished prior to irradiation.

2.3 Irradiation

For simulating the neutron irradiation under 100GWd/t of ultra high burn-up extension, the disk was irradiated by triple ion beams, 12MeV Ni^{3+}, 380KeV H^+ and 1.1MeV He^+, at TIARA in JAERI Takasaki. In irradiation, temperature of the disk was kept at 573 K. He^+ and H^+ were irradiated through the energy degraders to be spread at the implanting range. Distributions of displacement damage and each implanted ion in the disk were calculated with SRIM 2000[1]. He^+ and H^+ were at 1.0-1.5 μm from the bombarded surface in the calculation. Displacement damage was adjusted up to 50dpa at the depth because it was supposed that dose was about 50 dpa under ultra high burn-up extension. Ni concentration was less than 1.0 at% (≒1 wt%) at the depth, and H and He concentrations were adjusted 20-30 appm/dpa and 2-3 appm/dpa, respectively.

2.4 Microchemistry measurement

Bombarded surface of the disk was electrochemically removed to 1.2~1.3 μm in depth, and that surface was masked with a manicure for shielding from the following electrochemical process. Another surface was electrochemically jet thinned.

Microchemical measurement was examined by TEM/EDS of JEOL 2000F with Noran 623M-3SUT EDS system. Accelerating voltage was 200 keV at 10^{-7} torr order in operation. A double tilt specimen holder was used for the observation. The incident probe diameter was 1 ~2 nm in S mode. In analysis, each grain boundary was aligned such that the boundary was edge-on (parallel to the electron beam). All measurements were performed at a magnificent of 1000000x. Each data acquisition was typically interrupted every 10~20 sec to put back the electron probe. Data acquisition lasted for 90 sec of detector live time because samples drifted in small step during a period of measurement.

3. Result and discussion

Fig.1 shows the dose dependence of the change in Cr concentration at the grain boundary from the bulk in the 304SS for Mutsu cladding tube and the prototype candidate tube, respectively. It is the same tendency as that shown in other investigations that Cr depletion occurred in both materials. In the candidate tube, Cr depletion occurred up to 10 dpa at the grain boundary. Over 10dpa, Cr depletion is almost constant about 6 wt%. The 304SS tube will show the same pattern. Cr depletion is about 5 wt% until 50 dpa. Segregation of the 304SS for Mutsu cladding tube shows the similar Cr depletion in Refs[2-4].

It is considered that Cr depletion is quasi-saturated with the equilibrium of vacancy flux to the sink, e.g. grain boundary, and Cr self-diffusion flux up to 10 dpa under the irradiation because the primary driving mechanism of RIS is preferential interaction of solute atoms with vacancy flux[4].

Fig.2 shows the composition dependence of the quasi-saturated Cr depletion at the grain boundary for 304SS Mutsu cladding tube, 316SS, Fe-25Cr-20Ni and the candidates. Data of Cr depletion of 304SS for Mutsu cladding tube and the candidate are taken from Fig.1. 316SS and Fe-25Cr-20Ni were irradiated to 15 dpa because it is considered that Cr depletion of each material is quasi-saturated at about 10-20 dpa on this irradiation condition from Fig.1. Cr depletion in each material is about 5-10 wt% at 573K. It is considered that composition

Table 1 Chemical Composition of the candidates and comparisons

			Composition											
	Material	Histry	Fe	Cr	Ni	Ti	C	N	O	S	Si	Mn	P	Mo
Candidate	Fe-25Cr-35Ni	ST*1	bal.	24.40	35.56	0.21	0.0006	0.0010	0.0010	0.001	<0.01	<0.01	0.001	-
	〃 (prototype tube)	SAR*2	bal.	24.55	34.99	0.18	0.0013	0.0014	0.0011	0.0009	0.005	0.001	0.001	-
Comparison	Fe-25Cr-20Ni	ST	bal.	22.90	21.88	0.22	0.0010	0.0006	0.0005	0.002	<0.01	<0.01	0.001	-
	316SS	ST	bal.	17.54	12.55	-	0.008	-	-	0.001	0.43	0.83	0.023	2.11
	304SS(Mutsu cladding tube)	*3	bal.	18.72	10.27	-	0.063	-	-	0.012	0.490	1.45	0.016	-

*1: Solution Treatment
*2: Strain Aged Recrystallization
*3: normal tube processed with 12-15 % cold work

dependence of Cr depletion is seen, but that difference is small.

Cr concentration at the grain boundary measured by other investigators with AES is typically by 2-3wt% lower than that with TEM/EDS[4]. If Cr depletion may be lower than that of this study, Cr concentrations at the grain boundary of 304SS and 316SS may not be kept at 12 wt% for Cr, under which the austenitic stainless steel can be corroded. The candidate has enough Cr at the grain boundary even if the depletion of Cr concentration is 10wt%.

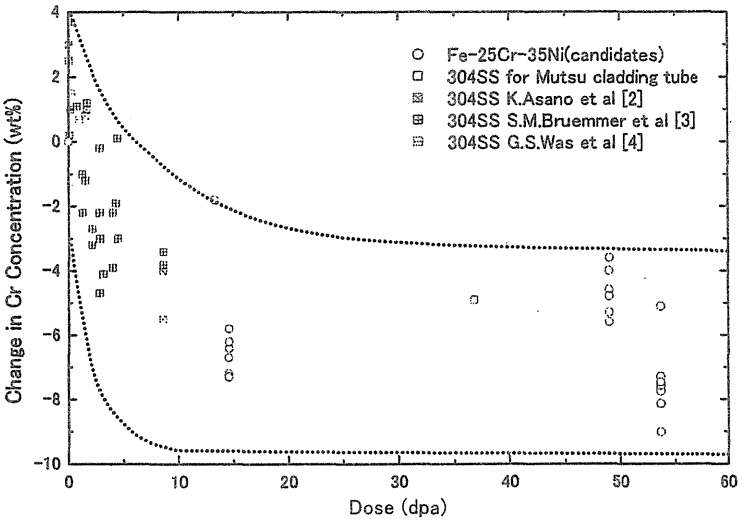

Fig.1 Dose dependence of the candidate tube and 304SS for Mutsu cladding tube

4. Summary

Dose dependence and composition dependence of Cr depletion at grain boundary were evaluated for the candidate and other comparisons at the irradiation temperature of 537K. Cr depletion at grain boundary of the candidate and 304SS are quasi-saturated at over 10 dpa in the value of 5-6wt%. A little composition dependence of Cr depletion was seen at quasi-saturated dose(15dpa). 304SS and 316SS may occur IGSCC if Cr depletion of 10 wt% occurred. But the candidate has enough Cr concentration to resist IGSCC.

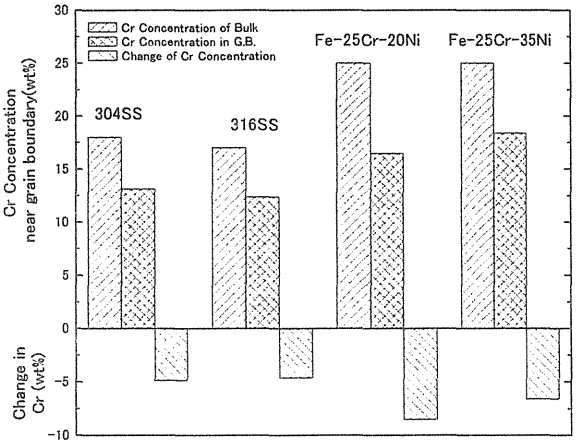

Fig.2 Composition dependence of Cr concentration for the candidates, Fe-25Cr-20Ni, 316SS and 304SS for Mutsu cladding tube

Reference

1) J.F.Ziegler et.al., "The Stopping and Range of Ion in Solids", vol.1, Pergamon Oress, New York (1985)
2) K.Asano et al., 5th Int. Symp. On Enviro. Degra. Of Mater. In Nucl. Power Sys Water Reactor,(1991)838.
3) S.M.Bruemmer et al., Corrosion, 50 (1994) 940.
4) G.S.Was et al, J.Nucl. Mater., 270(1999)96

4.7 Evaluation of Irradiation Effects on Improved Stainless Steel

F.Kano*, Y.Tsuchiya*, N.Saito*, A.Naito** and I.Ioka**
Toshiba Corporation*
Department of Material Science, JAERI**

1.Introduction

The supercritical-water cooled power reactor (SCWR) is expected to be an innovative nuclear power system with considerably higher thermal efficiency and the smaller specific volume. Material compatibility for core components, in particular fuel claddings, is thought to be a key factor for the viability of SCWR, since a severe environment consisting of wide temperature range and high dose of neutron irradiation presumed.

The SCWR will be operated in the wide temperature range of 573K to 823K. It is important to develop materials that have superior irradiation resistance characteristics in the SCWR environment, particularly in regard to void swelling [1,2]. These are influenced by point defect introduced by irradiation. Therefore, the grain size of alloys was made fine, and the effect of additive element to accomplish this in the case of austenitic stainless steels was evaluated.

2.Experimental

The specimens examined were SUS304 stainless steels. The grain size is finer than those of commercial alloys. 0.06%Ti is added to alloys to make the grain sizes fine. Specimen with a usual grain size is given as a reference for the purpose of comparison with other ones. They were manufactured by cold work and heat-treatment. The 3mm diameter TEM discs were irradiated with 12MeV Ni^{3+} ions at 573K and 823K. The dose was 2 dpa at 1μm depth from the surface. The damage peak depth and nickel ion range peak depth were over 2μm. Therefore we can avoid any influence on the compositional distribution of implanted nickel ion. After irradiation, the specimen surface was removed by electropolishing to 1μm and back-thinned for perforation in 10%$HClO_3$+CH_3COOH solution. Microstructural observation on the bright field image (BF) and high-angle annular dark-field (HAADF) were conducted using a FE-TEM (TOPCON EM-002BF).

3.Results

Fig. 1 shows an optical micrograph of the typical specimen before irradiation. The grain sizes of a usual SUS304 and a fine grain SUS304 are 70 and 1 micron, respectively. Fig.2 shows the BF and HAADF microstructures with a usual grain size after irradiation at 723K to 5dpa. Voids were observed on the usual one. HAADF image has a contrast depending on the atomic number Z, then voids can be seen as black points clearly. . Fig.3 shows the BF and HAADF microstructures with a fine grain size after irradiation at 723K to 5dpa.There are few voids in fine one.

Hasegawa et al. [3] have reported that fine-grained austenitic stainless steel has good corrosion performance. Because grain boundary length is longer in fine grained alloy, capture of impurities is thought to be easy,

causing general- corrosion at grain boundary. As the distance to grain boundary is short in refined-grain alloys, the vacancy concentration differs between the fine-grain alloy and the usual alloy at void nucleation temperature.

In this examination, there are specimens with larger grain size and specimens with grain size smaller than the irradiation range from the surface. A change to void swelling is thought unlikely to occur if grain size is larger than the irradiation range. As a r estraint effect of the void production is seen in specimens other than SUS 304, an effect of additive element is a dominant factor. A similar effect is found in titanium-added SUS with the usual grain size [4]. Grain refinement is thought to have magnified the effect.

References

1) F.Kano, Y.Tsuchiya, N.Saito, S.Shiga, S.Kasahara and H.Takahashi, Proc. of Int.Cong. on Advenced Nuclear Power Plants, ANS, 2003, pp3285
2) Y.Tsuthiya, F.Kano, N.Saito, S.Shiga, S.Kasahara, K.Moriya and H.Takahashi, Proc. of Int. Conf. on Global Environment and Advanced Nuclear Power Plants, NEI, 2003, pp1096
3) M. Hasegawa and M.Osawa, Corrosion, 40,7 (1984)371
4) N.Sakaguchi, S.Watanabe and H.Takahashi, J. Nucl. Inst.&Met.B., 153(1999)142

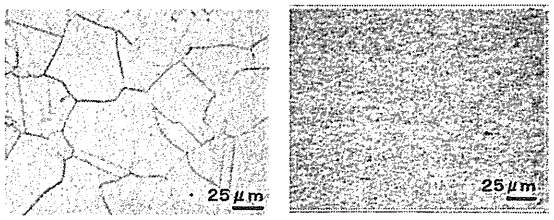

Fig.1 Optical micrograph of the typical specimen before irradiation. The grain sizes of a usual SUS304 and a fine grain SUS304 are 70 and 1 micron.

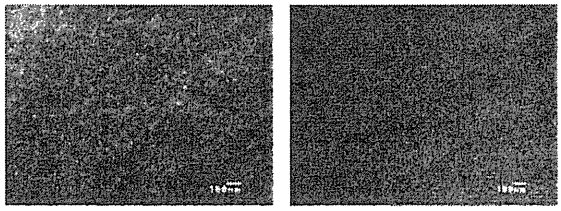

Fig. 2 TEM BF and HAADF microstructures after Ni ion irradiation in SUS304 with usual grain size at 723K to 5dpa.

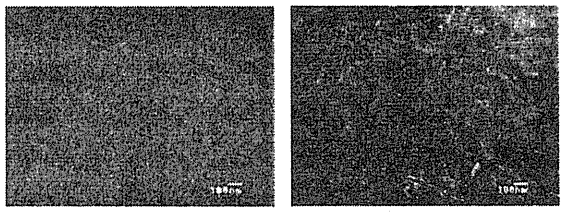

Fig. 3 TEM BF and HAADF microstructures after Ni ion irradiation in SUS304 with fine grain size at 723K to 5dpa.

4.8 Observation of Microstructural Changes in Li_2TiO_3 Caused by Ion Beam Irradiation

D. Yamaki, T. Nakazawa, T. Aruga, T. Tanifuji and S. Jitsukawa
Department of Materials Science, JAERI

1. Introduction

Li_2TiO_3 is regarded as one of the most suitable candidates for the solid tritium breeder material of D-T fusion reactors[1]. It is known that, in an operating fusion reactor, the radiation damage in Li_2TiO_3 will be caused by fast neutrons, energetic tritons and helium ions generated in $^6Li(n,\alpha)^3H$ reaction. The irradiation damage caused by such radiations may result in the microstructural changes, and the changes may affect the characteristics of Li_2TiO_3 such as tritium release behavior. Thus the study of irradiation defects and microstructural change caused by irradiation in Li_2TiO_3 is essential to evaluate its irradiation performance.

Simulation of the fusion reactor environment and hence the study of a synergistic effect of atomic displacement damage in Li_2TiO_3 are presumed to be approached by a simultaneous irradiation with "triple" ion beams which consist of O^{2+}, He^+ and H^+ ion beams. In the previous study, the formation of the anatase (TiO_2) layer on the surface of Li_2TiO_3 by irradiation with triple ions has been found. It is also clarified that the formation mainly caused by the effect of O^{2+} ion beam irradiation[2-5]. In the present study, the results of the FT-IR photoacoustic spectroscopy (PAS) with Li_2TiO_3 samples irradiated with the single and the triple ion beams were analyzed to study the relation between the irradiation effects and the microstructural change.

2. Experimental

The characteristics of the Li_2TiO_3 samples used in this experiment were described in ref.4. The Li_2TiO_3 samples were irradiated at 573K with the single and the triple ion beams of 0.25 MeV H^+, 0.6 MeV He^+ and 2.4 MeV O^{2+}. The fluence of the respective ions were about $1x10^{21}$ ions/m^2 The ion energies were so chosen that the projected ranges of the irradiated ions in Li_2TiO_3 were around 2 μm[3].

Using the FT-IR photoacoustic spectroscopy (PAS) technique on the non-irradiated sample, on samples irradiated with the triple ion beam and on samples irradiated by the single ion beams were examined in order to obtain information near the end of the ion range. The photoacoustic signal was generated from the surface layers of sample with a thickness of some micrometers, which is a function of the mirror velocity of the FT-IR interferometer and wave number. In this case, the mirror velocity was 2 cm/s which corresponds to the thickness of about 15-5 μm for 400-4000 cm^{-1}, so that the spectra of irradiated samples are a superposition of spectra of irradiated and non-irradiated zones of the sample.

3. Results and discussion

The FT-IR PAS spectrum of a non-irradiated sample is shown in Figure 1. The characteristic peaks in FT-IR PAS spectra were observed around 680, 780, 880, 1090, 1430, 1480, 1570, 3150, 3450 cm^{-1}. The 880, 1090, 1430 and 1490 cm-1 peaks are believed to be due to Li_2CO_3 which is one of the raw materials of Li_2TiO_3 samples and is believed to exist as an impurity in the samples[6]. In comparison to the reported spectra of TiO_2 and Li_2TiO_3, 680 and 780 cm^{-1} peaks are identified as due to Ti-O, and 1570, 3150 and 3450 cm^{-1} peaks are from the O-H

bond in hydroxyls adsorbed on or near the surface[7-9].

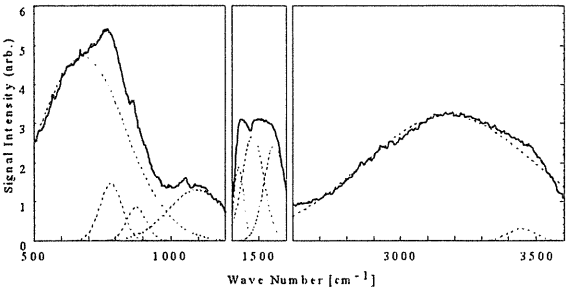

Figure 1. FT-IR PAS spectrum of non-irradiated Li_2TiO_3 sample. Dashed lines are the results of peak analysis.

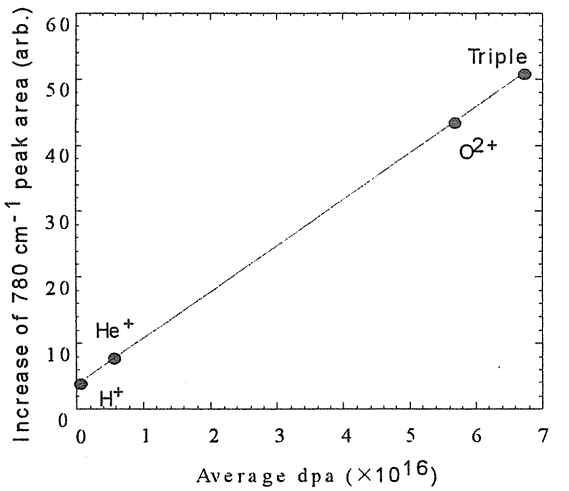

Figure 2. Dependence of the increase of 780 cm^{-1} peak area on the average dpa.

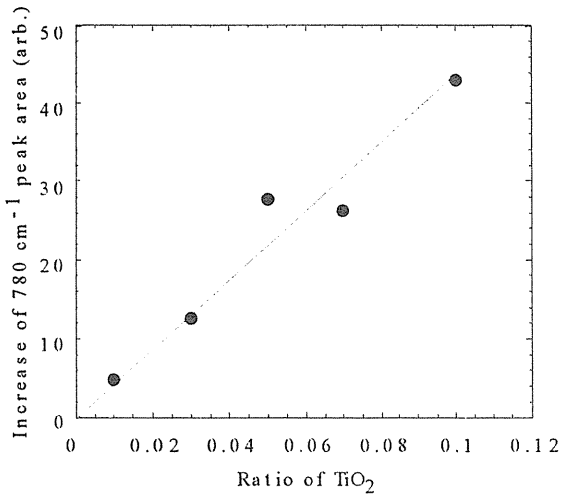

Figure 3. Dependence of the increase of 780 cm^{-1} peak area on the ratio of doped TiO_2

Among the observed peaks, irradiation effect is clearly found for 780 and 3450 cm^{-1} peaks. Figure 2 shows the relation between the average displacements per atom (dpa) in the depth measurable with FT-IR PAS and the increase of 780 cm^{-1} peak area from the Ti-O bond, for each irradiation. The dpa was estimated with the TRIM code. It is shown that the peak area increases in proportional to the average dpa. To simulate the formation of TiO_2 in Li_2TiO_3, Li_2TiO_3 samples doped with 1-10% TiO_2 were prepared. Figure 3 shows the relation between the ratio of doped TiO_2 and the increase of 780 cm^{-1} peak area. It is also shown that the peak area increases in proportion to the ratio of doped TiO_2. From the comparison of the results in Figures 2 and 3, it is suggested that TiO_2 observed by Raman spectroscopy in the sample irradiated with the triple ion beams[2-3] is formed by displacements, and the amount of TiO_2 is proportional to the dpa in the sample.

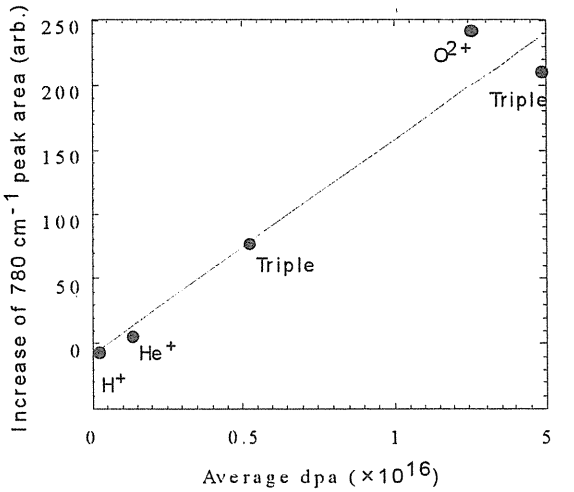

Figure 4. Dependence of the increase of 3450 cm^{-1} peak area on the average dpa.

Figure 4 shows the relation between the average dpa in the measurable depth with FT-IR PAS and the increase of 3450 cm^{-1} peak area, which is due to the O-H bond. The peak area increases in proportion to the average dpa. In this case, there is no relation between the

increase of 3450 cm^{-1} peak area and the amount of doped TiO_2. Thus, it suggests that the increase of 3450 cm^{-1} peak area observed in the irradiation samples has no relation to the formation of TiO_2 by irradiation, and the defects generated by displacements become the trapping sites for hydrogen adsorbed on or near the surface, so that the amount of hydroxyl near the surface increased proportionally to the dpa. It must be noted that such the hydrogen-trapping sites would also trap tritium generated in the fusion environment and would disturb the rapid recovery of tritium from the breeding material.

4. Conclusion

The microstructural changes in Li_2TiO_3 irradiated with the triple ion beam and with single ion beams of H^+, He^+ and O^{2+} were observed by FT-IR PAS. The results suggest that amount of TiO_2 formed is proportional to the average dpa, and that the defects generated by irradiation would trap hydrogen near the surface. The formation of TiO_2 and increase in the amount of hydroxyl near the surface observed in this study are believed to significantly affect the chemical form of released tritium and the tritium inventory in the breeding material of a fusion reactor. Further study of the effects of dpa on the tritium release is needed.

References

1) P.Gierszewski, Report no CFFTP G-9561, 1995.

2) T.Nakazawa, V.Grishmanovs, D.Yamaki, Y.Katano, T.Aruga, A.Iwamoto and S.Jitsukawa, JAERI-Review 2001-039 (2001) 146-148.

3) T. Nakazawa, V.Grishmanovs, D.Yamaki, Y.Katano, T.Aruga and A.Iwamoto, in: Proceedings of the 2000 International conference on Ion Implantation Technology, 2000, p.753-756.

4) D.Yamaki, T.Nakazawa, T.Aruga, T.Tanifuji, S.Jitsukawa and A.Iwase, JAERI-Review 2002-035 (2002)133-135.

5) D.Yamaki, T.Nakazawa, T.Aruga, T.Tanifuji, and S.Jitsukawa, JAERI-Review 2003-033 (2003)162-164.

6) S. Oohira, M.Kakihana, Y.Fujii, T.Nagumo and M.Okamoto, J. Nucl. Mater. 133&134 (1985) 201-204.

7) G. Durinck, H.Poelman, P.Clauws, L.Fiermans, J.Vennik and G.Dalmai, Solid State Communications Vol.80 (1991) 579-581.

8) K. Morishige, F.Kanno, S.Ogiwara and S.Sasaki, J. Phys. Chem. 89 (1985) 4404-4408.

9) S. Tanaka, M.Taniguchi, M.Nakatani, D.Yamaki and M.Yamawaki, J. Nucl. Mater. 218 (1995) 335-338.

4.9 Visualization of Mobile Defect Clusters in Copper and Gold under Ion Irradiations by In-situ TEM Observations

H. Abe*, T. Tadokoro **, N. Sekimura ** and H. Itoh ***

Research Center for Nuclear Science and Technology, University of Tokyo, Tokai, Japan*
Department of Quantum Engineering and Systems Science, University of Tokyo, Hongo, Japan **
Department of Materials Development, JAERI, Takasaki, ***

1. Introduction

Irradiation with ions and neutrons produces bunches of atomic displacements in materials, so-called displacement cascades. Molecular dynamics (MD) simulations claimed punching of tiny crowdion-related dislocation loops at the periphery of displacement cascades in iron and copper at 0-100 K. Neither post-irradiation observations nor in-situ observations was successful to detect interstitial-type defect clusters at the temperature of vacancy-mobile regions (stage III, IV and V), because of their presumed instability. We have been successful to visualize the interstitial-type crowdion-related clusters by developing modified weak-beam dark-field (WBDF) method, which allows highest resolution detecting weak strain field around defects. The purpose of this study is to report first experimental evidence of such highly-mobile and crowdion-related interstitial clusters by in-situ TEM observations under ion irradiations.

2. Experimental procedure

Well-annealed copper and gold disks were electrochemically perforated to achieve electron-transparent thin foils. Irradiation was performed with 240 keV Cu^{+} ions or 900 keV Xe^{3+} ions and 5 x 10^{11} ions/cm^{2}s at temperatures ranging from 573 K to 823 K. Taking into account the irradiation geometry, projected ranges from the sample surface were estimated by TRIM calculations as 57 and 110 nm for copper and xenon ions, respectively. Thickness of the observed regions was typically fixed from 50 to 70 nm, so as to achieve the identical implantation rate and to perform quantitative analysis based on areal density measurements of defect clusters. Microstructural evolution was observed mainly with the WBDF technique ($\mathbf{n}$ = [001], $\mathbf{g}$ = 200, $\mathbf{g}$ (4-6$\mathbf{g}$)). The sample geometry and the g vector were carefully chosen to minimize sample vending effect on the microstructure. The image was videotaped with time resolution of 1/30 s and analyzed without image processors to achieve the maximal time resolution.

3. Results and discussion

Tiny defect clusters (typically 1-10 nm in diameter) were formed under ion irradiation, majority of which were vacancy-type clusters including stacking fault tetrahedra (SFTs). Their lifetime ranging from a tenth to tens of seconds, and typically it became longer as increasing mass of incoming ions and as

lowering irradiation temperature. The interstitial- type defect clusters, detected for the first time in this work, have lifetime of several thirtieth seconds at temperatures from 673 to 823 K. Some of the interstitial clusters transform into highly-mobile clusters whose rate ranges 1 to 140 nm per video frame (1/30 s). They were typically mobile one-dimensionally. Note that the maximum velocity mentioned above could be experimentally limited because we employed a fixed magnification so as to achieve 1-nm resolution or even better. Molecular dynamics simulations on 1/3 {111} (111) loops (sessile loops) under compression revealed that the loops transform into 1/2 {110} (110) loops, and the energy variation is 30 meV/atom. It is presumed that the sessile-to-glissile transition of interstitial dislocation loops plays a role on the mobile cluster formation.

As increasing implantation dose, decrease in evolution rate of defect clusters, longer lifetime of the clusters and lower mobility of glissile loops were observed. Implantation effect is presumed. SRIM calculations indicate the penetration rate of incoming ions varies from 60 to 75 % in the 50 nm-thick samples within the conditions investigated in this work. A model is proposed that mobility of glissile clusters is perturbed by existence of point defects, and attributable to form sessile clusters which are visible in transmission electron microscopy.

4. Conclusions

Defect clusters corresponding to displacement cascades were observed by in-situ TEM observations in copper under irradiations with 240-keV Cu^+ ions and 900-keV Xe^+ ions at temperatures from 573 K to 823 K. We observed two or three defects appeared at the same time within the time resolution of 1/30 s under irradiation. From their anisotropic distributions, and fluence-dependent distance ranging from 4 to 140 nm, as well as mass-dependence, we conclude that the multi-cluster formation is a single ion event, and that subcascades and mobile defect clusters formed directly from cascades are attributable. The observations and molecular dynamics simulations suggest that the dislocation loops can transform into crowdion-related defect clusters, diffuse along the crowdion directions, and transform again into sessile ones at certain diffusion obstacles which are invisible in TEM.

4.10 *In-situ* Observation of Nitriding Transformation of Titanium Thin Films by Nitrogen-implantation

Y. Kasukabe*, J. J. Wang**, T. Yamamura**, S. Yamamoto***,
M. Yoshikawa*** and Y. Fujino*
International Student Center / Department of Electronic Engineering, Tohoku University*
Department of Metallurgy, Tohoku University**
Department of Material Development, JAERI***

1.Introduction

Titanium nitride (TiN_y) of NaCl-type has widely been used for many purposes such as a hard wear-resistant coating in cutting tools, a diffusion barrier in microcircuits, etc.[1),2)] Although its elastic and diffusion-barrier properties are highly anisotropic and depend strongly upon film orientation, the formation mechanisms of preferred orientation of epitaxial TiN film are not sufficiently understood. Recently, it was reported that NaCl-type (110)- and (001)-oriented TiN_y crystallites were "epitaxially" grown by nitrogen (N-) implantation into CaF_2-type (110)-oriented TiH_x and (03•5)-oriented hcp-Ti in deposited Ti films held at room temperature (RT).[3)] However, the detailed "epitaxial" nitriding process of Ti films without the domains of TiH_x, and the change of the bonding interaction of Ti atoms with ligand of N-atoms during N-implantation have not yet been understood.

The purpose of this study is to elucidate the nitriding process of pure hcp-Ti without TiH_x. In this paper, the changes of the electronic structures induced by N-implantation were examined by applying *in-situ* electron energy loss spectroscopy (EELS). The results of EELS were discussed along with the results of a self-consistent charge discrete variational (DV)-X α molecular orbital (MO) calculation combined with transmission electron microscope (TEM) observations.

2.Experimental

Detailed descriptions of the preparation of evaporated-Ti films were presented in the earlier paper.[3)] The 100-nm-thick Ti films were deposited by an electron-beam heating method in an ultra-high vacuum onto thermally cleaned NaCl substrates held at RT. The ultimate pressure in the working chamber was less than $4x10^{-9}$ Torr. The implantations of N_2^+ ions with 62 keV into the deposited Ti films held at 350℃ were performed in the 400 kV analytical and high resolution TEM combined with ion accelerators at JAERI- Takasaki.[4)] According to the Monte Carlo simulation using the SRIM2003 code, the projected range of N_2^+ with 62 keV was 55 nm, and thus most of the implanted ions are thought to be retained inside the Ti films. The N- concentrations in Ti films were able to be estimated from the implantation dose measured by a Faraday cage. The maximum dose in this experiment was $5.40x10^{17}$ ions/cm^2, which corresponded to the N/Ti ratio of 0.954 (the average atomic concentration of N in the Ti film).

3.Results and discussion

In-situ observations by TEM elucidated that Ti films grown on NaCl (001) surfaces at RT consisted of hcp-Ti and CaF_2-type TiH_x ($x \cong 1.5$). The TiH_x was transformed into hcp-Ti at 350℃, accompanied by H-release. Thus, nitrogen ions were implanted into the hcp-Ti films without TiH_x. The NaCl-type TiN_y is "epitaxially"

formed in N-implanted hcp-Ti by the transformation of the hcp-Ti to fcc-Ti, partially inheriting the atomic arrangement of the hcp-Ti and accompanying the occupation of octahedral (O-) sites of the fcc-Ti by N atoms.

In-situ observation of EELS elucidated that electron energy loss spectra gradually changed with increasing the dose of N-implantation into hcp-Ti at 350℃. Figure 1 shows the variation of energy loss spectra with N-dose. The loss peak (~47 eV) denoted by the line of Ti 3p-3d corresponds to the Ti 3p-3d resonant photoemission, in which the electron is excited from the Ti 3p state to an empty Ti 3d state and then relaxes back to the Ti 3p state, and another electron from Ti 3d states is ejected. It should be noted that the Ti 3p-3d peaks are almost invariant with the N/Ti ratio, which means that the energies of the core levels are almost invariant during this experiment. The energy loss of ~17.0 eV, indicated by a solid triangle at N/Ti=0, was found to agree well with the theoretical value of ~17.6 eV, the energy loss due to plasmon excitation, calculated with assumption that 3d and 4s electrons are all free.

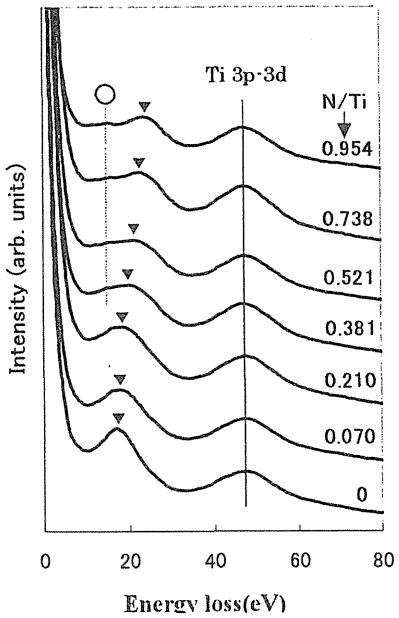

Fig. 1 Variation of EELS spectra with the dose of N ions.

The energy loss peaks due to plasmon excitation indicated by solid triangles gradually shifted to higher energies with increasing dose. This means that the number of N atoms bonding to Ti atoms increases with the dose, and that the electron density in the hybridised N 2p/Ti 3d-4p valence band also increases with the dose.

To investigate changes in the electronic structures of N-implanted Ti films in detail, DV-$X\alpha$ MO calculations have been performed for two cluster models shown in Figs. 2(a)-2(b). The Ti_{19} cluster of Fig. 2(a) corresponds to a part of hcp-Ti structure. The Ti-Ti distances are taken to be 0.29238 nm, corresponding to those of the bulk ideal crystal structure. A $Ti_{14}N_{13}$ cluster model for NaCl-type TiN is shown in Fig. 2(b). The nitrogen atom as indicated by G occupies the O-sites of the octahedron as formed by A-F atoms in the fcc-Ti sublattice. The Ti-N distances are assumed to be 0.21200 nm, corresponding to those of the bulk crystal

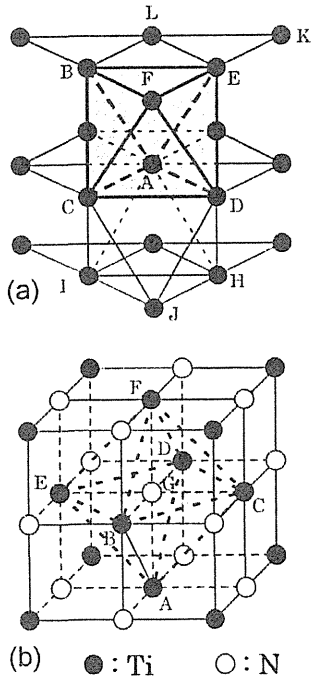

Fig. 2 Schematic illustrations of (a) Ti_{19} cluster, (b) $Ti_{14}N_{13}$ cluster models. The corner-, edge-, and/or face-sharing contacts of octahedron as indicated by A-F atoms lead to the formation of the hcp-Ti and fcc-Ti structures

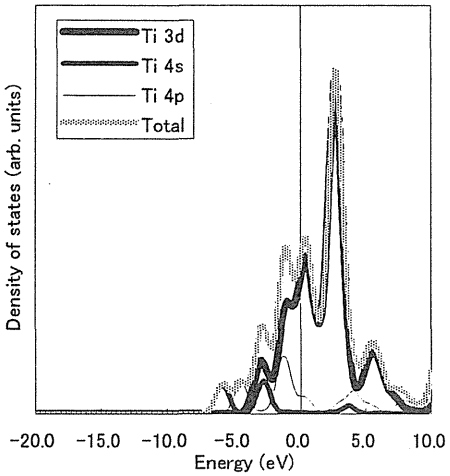

Fig. 3(a) Local density of states (DOS) curves for Ti_{19} cluster shown in Fig 2(a).

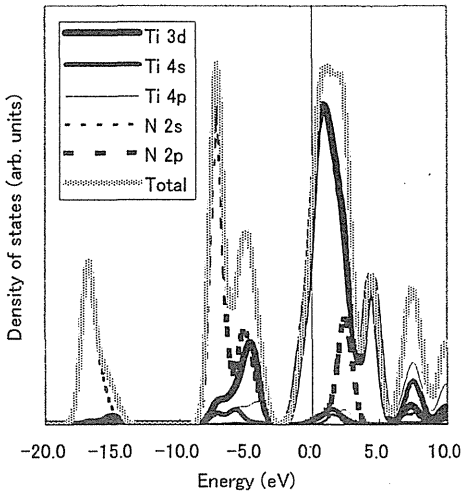

Fig. 3(b) Local density of states (DOS) curves for Ti_{19} cluster shown in Fig 2(b).

structure of TiN. The DOS curves for the Ti_{19} cluster of Fig. 2(a) are shown in Fig. 3(a). Curves of Ti 3d, Ti 4s, Ti 4p and Total correspond to Ti 3d, Ti 4s, Ti 4p DOS and superimposition (total DOS) of them, respectively. The line at 0.0 eV represents the Fermi level, E_f. It is seen from Fig. 3(a) that the width of Ti 3d DOS is smaller than that of hybridized Ti 4s-4p DOS. This means that the DOS structure of the Ti_{19} cluster already has the feature of the Ti electronic structure, and that the conduction band consists of the narrow 3d DOS and the broad 4s and 4p DOS. Figure 3(b) shows DOS curves for the $Ti_{14}N_{13}$ cluster of Fig. 2(b). Curves of N 2s, N 2p correspond to N 2s, N 2p DOS, respectively. The loss peak (-16.0 eV) denoted by the dotted line connected to the open circle in Fig. 1 can be seen at $N/Ti \geq 0.38$. This peak is considered to be due to excitation of N 2s electrons around -16 eV in Fig. 3(b) to the conduction band. It is seen from Fig. 3(b) that the occupied states consist of bonding states from -2.4 eV to -9.8 eV and the antibonding states from E_f to -2.2 eV. The bonding states are mainly derived from N 2p, whereas the antibonding states are mainly derived from Ti 3d.

Comparing Fig. 3(b) with Fig. 3(a), it can be seen that Ti 3d DOS from –3.0 eV to -8.0 eV in Fig. 3(b) appears when N 2p DOS from –3.2 eV to –8.6 eV appears. This means that the contribution to the bonding states by hybridization of Ti 3d-N 2p is larger than that by the other hybridization. The hybridization of the Ti 3d state to N 2p and N 2s states results in the increase in the electron density of the valence band, which leads to the shift to higher energy loss side due to the excitation of plasmon in the N-implanting stage. Moreover, formation of Ti 3d DOS around –5 eV due to the hybridization of Ti 3d-N 2p leads to the decrease in the DOS near the E_f, which means the reduction in the electron energy of Ti sublattice, and the reinforcement of covalent bonds of TiN_y.

References

1) G. S. Chen, J. J. Guo, C. K. Lin, Chen-Sheng Hsu, L. C. Yang, and J. S. Fang, J. Vac. Sci. & Technol. **A20** (2002) 479-485.
2) J. E. Sundgren, Thin Solid Films **128** (1895) 21-44.
3) Y. Kasukabe, N. Saito, M. Suzuki, Y. Yamada, Y. Fujino, S. Nagata, M. Kishimoto, and S. Yamaguchi, J. Vac. Sci. & Technol. **A16** (1998) 3366-3375.
4) H. Abe, H. Naramoto, K. Hojou, and S. Furuno, JAERI-Research **96-047** (1996) 1-18.

4.11 Preparation TiO_2/ZnO Films by Pulsed Laser Deposition

S. Yamamoto, Y. Choi, T. Umebayashi, A. Takeyama and M. Yoshikawa
Department of Material Development, JAERI

1. Introduction

The photocatalytic properties of titanium dioxide (TiO_2) have attracted much interest from the viewpoints of basic science and applications. For improving photocatalytic activity of TiO_2 films, the high quality epitaxial films, the control of crystalline phase and the fabrication of effective large surface area were required. However, the growth of epitaxial TiO_2 films was necessary to use the high quality single-crystal substrates such as $SrTiO_3$, $LaAlO_3$, α-Al_2O_3. In order to utilize the photocatalytic activity of epitaxial TiO_2 films, it is essential that techniques for preparation films on glass or polycrystalline substrate be available. Zinc oxide (ZnO) is one of the most suitable materials to use as a buffer layer. Since ZnO films are highly c-axis oriented, self-textured ZnO thin films have been prepared on any substrate such as quartz glass. Furthermore, high quality epitaxial ZnO films consisting of hexagonal shaped grains on α-Al_2O_3 substrates have been synthesized. Thus, ZnO buffer layer on substrate can be realized the fabrication of TiO_2 films consisting of highly oriented grains with nanometer sizes.

In this study, highly oriented anatase TiO_2 (001) and rutile TiO_2 (100) mixed films were grown using a highly oriented ZnO (0001) buffer layer with nanometer sizes grain on quartz glass substrate. ZnO and TiO_2 thin films were deposited by pulsed laser deposition (PLD) in an O_2 atmosphere. The crystal quality, the crystallographic orientation relationships, and photocatalytic activity of films are reported.

2. Experimental

TiO_2 and ZnO films were deposited on α-Al_2O_3 and quartz glass substrates by PLD using a KrF excimer laser (wavelength: 248 nm). The laser beam was incident on a target with an incident angle of 45°. It was focused to a 2 × 3 mm rectangle on the target face. A metal Zn (purity: 99.9%) and a single-crystal TiO_2 (rutile) targets were used for ZnO and TiO_2 film deposition, respectively. The substrates were separated by about 5 cm from the target. Oxygen gas (purity: 99.99 %) was flowed into the chamber through a mass-flow meter controlled by an absolute pressure gauge under the pumping condition. In this study, ~200 nm thick TiO_2 films were deposited at 500°C under oxygen pressure of 1.3 – 26.3 Pa. The crystallographic relationships between TiO_2 films and ZnO layer were determined by X-ray diffraction (XRD). Rutherford backscattering spectroscopy (RBS)/channeling analysis using a 3 MV single-stage-accelerator at JAERI/Takasaki was employed to characterize the epitaxial thin films. The analyzing 2.0 MeV $^4He^+$ ions were incident and backscattered particles were detected at 165° scattering angle with a surface barrier detector. The film thickness and composition were evaluated from RBS spectra. The surface morphology of the deposited films was examined using a high-resolution field emission scanning electron microscopy (FE-SEM). Photocatalytic activity of films was evaluated using the decomposition of methylene blue in aqueous solution monitored by UV-vis spectroscopy.

3. Results and discussion

The growth condition for highly oriented ZnO films was optimized referring to the crystal quality of ZnO on the α-Al_2O_3(0001) substrate. The suitable condition for highly oriented ZnO films was following conditions; laser energy: 150 mJ/cm^2, oxygen gas pressures: 4.7 Pa, substrate temperature: 500°C, target species: Zn metal. Figure 1 illustrates 2.0 MeV $^4He^+$ RBS spectra for the ZnO film on (a) α-Al_2O_3 ($11\bar{2}0$) and (b) quartz glass substrates taken under the random and the axial channeling condition. The aligned spectrum was taken with the beam directed along the <0001> axis of the ZnO film. The minimum yield, χ_{min} value, the ratio between the random and the axially aligned yield at the fixed depth near the surface region, gives a measure to evaluate the degree of disorder in crystalline solids. The χ_{min} value in the <0001> aligned spectrum is 0.05 at the just

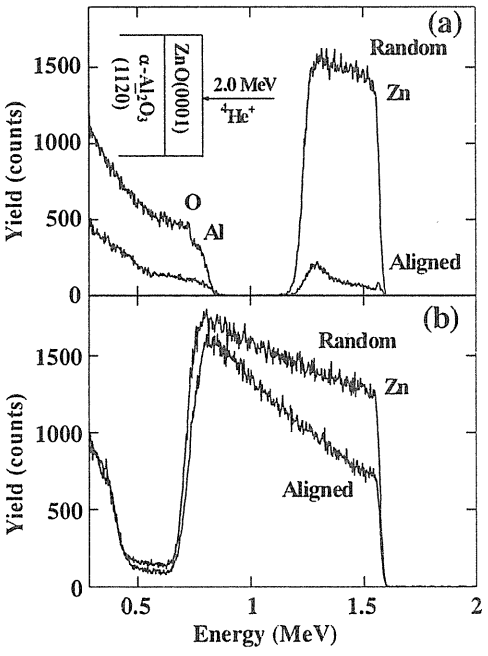

Fig. 1. 2.0 MeV $^4He^+$ RBS/channeling spectra for deposited ZnO films on the (a) α-Al_2O_3 ($11\bar{2}0$), and (b) quartz glass, respectively. The thicknesses of ZnO fims are 233 nm and 571 nm, respectively. The aligned spectrum was taken with the beam directed along the <0001> axis of the ZnO films.

area behind the surface peak of the Zn component in the ZnO film, which suggests that the crystal quality of the ZnO film is high enough as in a bulk single-crystal.

As can be seen from Fig.1 (b), axial channeling RBS spectra are obtained from ZnO film on quartz glass substrate even if it has amorphous structure. The huge reduction of backscattering yield from the Zn component of the ZnO film under the axial channeling condition suggests that highly oriented ZnO films are grown with increasing the film thickness. The results suggest that thicker ZnO films on glass substrate can be useful as a buffer layer for highly oriented oxide films.

The TiO_2 films were prepared under the following conditions; laser energy: 150 mJ/cm^2, oxygen pressures: 1.3 – 26.3 Pa, substrate temperature: 500°C, target species: single-crystal TiO_2 (rutile). Figure 2 shows the X-ray diffraction patterns for TiO_2/ZnO films on quartz glass substrates deposited at various oxygen pressures. It can be seen from Fig. 2

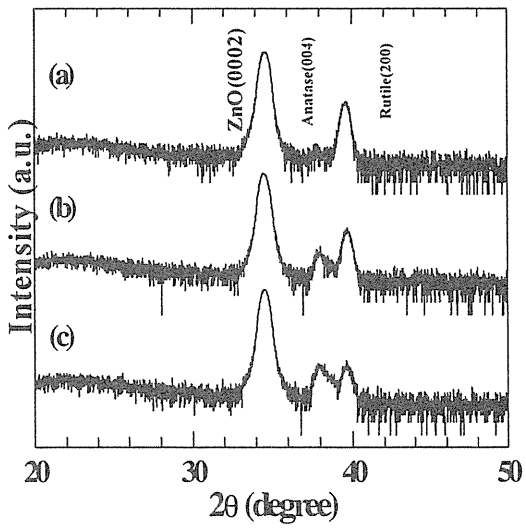

Fig. 2. X-ray diffraction patterns for TiO_2/ZnO films on quartz glass substrate. TiO_2 films were deposited at various oxygen pressures: (a) 1.3 Pa; (b) 13.3 Pa; (c) 26.6 Pa.

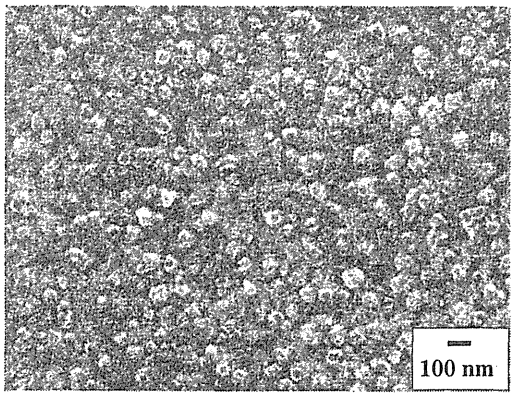

Fig. 3. SEM image of TiO_2 surface grown at 500°C under the oxygen pressure of 13.3 Pa.

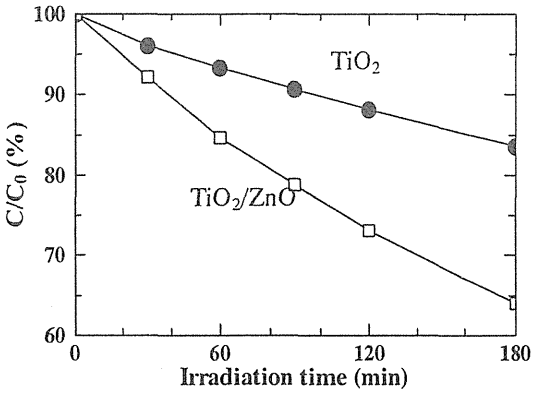

Fig. 4. Decomposition of methylene blue in an aqueous solution (1×10^{-5} mol dm^{-3}) by the (.) TiO_2/glass and (.) TiO_2/ZnO/glass as a function of the UV light irradiation time.

(a)-(c), the structure of deposited TiO_2 film on the highly oriented ZnO (0001) layer is composed of oriented anatase TiO_2 (001) and rutile TiO_2 (100). As the oxygen pressure was increased during the deposition, the component of anatase phase was increased. It is found that the anatase-rutile ratio in such phase mixed films is controlled by oxygen pressure during the deposition.

Figure 3 shows the surface morphology of the TiO_2 film on ZnO buffer layer observed by FE-SEM. The TiO_2 film was grown at 500°C under the oxygen pressure of 13.3 Pa. The surface of the film shows coarse grains with about 100 nm sizes. The grain size of the TiO_2 films is comparable to that of ZnO films on quartz glass substrate. Surface morphology implies that each grain corresponds to single crystal of rutile and anatase TiO_2 structures. These grains have grown epitaxailly on the highly oriented ZnO (0001) buffer layer.

Photocatalytic activity of films was evaluated using the decomposition of methylene blue in aqueous solution. The progress of the degradation reaction was followed by monitoring the decrease in the absorbance of aqueous dye solutions as a function of the UV-light irradiation time counted from the beginning. The UV-light (1.0 mW/cm^2) with a black light lamp was used. The result of TiO_2/ZnO films deposited with different oxygen pressure showed that the TiO_2 film deposited on the ZnO buffer layer at 500°C under the oxygen pressure of 13.3 Pa, consisting of oriented anatase TiO_2 (001) and rutile TiO_2 (100) (referred to Fig. 2), had a high efficiency for the decomposition reaction. Figure 4 shows the photocatalytic behavior of the (.) TiO_2/ZnO and (.) TiO_2 films on quartz glass substrates during the degradation of methylene blue. Each TiO_2 films were deposited at 500°C under the oxygen pressure of 13.3 Pa. The TiO_2/ZnO film shows a high efficiency for the decomposition reaction. The above results reveal that the ZnO buffer layer on glass substrate is very useful for improving photocatalytic properties of the present TiO_2 film

4.12 Secondary Electrons Emitted from Solids Bombarded by MeV Atom Clusters

H. Kudo*, T. Suzuki*, M. Nagata*, S. Tomita*, K. Shima**, K. Sasa**, S. Ishii**, Y. Saitoh***, S. Yamamoto****, K. Narumi*****, H. Naramoto***** and T. Kaneko******
Institute of Applied Physics, University of Tsukuba*
Tandem Accelerator Center, University of Tsukuba**
Advanced Radiation Technology Center, JAERI***
Department of Material Development, JAERI****
Advanced Science Research Center, JAERI*****
Department of Applied Physics, Okayama University of Science******

1. Introduction

Fast cluster ions in the MeV/atom energy range give rise to nonlinear radiation effects on solid targets with respect to the number of atoms in the cluster n.[1,2] Empirically, whether the nonlinearity is constructive (superlinear) or destructive (sublinear) depends on whether the phenomenon is related closely with the nuclear or electronic stopping power. Indeed, the sublinearity has been observed by several workers for electron emission by fast cluster impacts, which results from the electronic cluster-solid interactions.

It is of vital interest to investigate the electronic cluster effects by energy analysis of the cluster-induced electrons. Since low-energy electrons escape mainly from a nanometer surface layer, they should reflect the behavior of the cluster itself, rather than of the fractions of the cluster after being broken up seriously.

2. Experiment

The experimental technique has been much improved in this year. The emitted electrons in the low-energy range were successfully measured at 180° with respect to the beam direction, using a 45° parallel-plate electrostatic spectrometer of the double-deflection type.[3] The 180° measurement is advantageous for the purpose of avoiding errors associated with misalignment of the spectrometer direction. Once the spectrometer is accurately placed at 180°, its entrance axis always passes through the irradiated spot on the surface of the sample. This is not necessarily anticipated at other detection angles. In some cases, the misalignment is caused by different beam-transport conditions for different cluster beams, which effectively changes the counting efficiency, and therefore, disturbs the measurements of n-dependence of the electron spectra.

Furthermore, we have collected the experimental data not only at TIARA, but also at UTTAC recently. This is useful because the velocity dependence of the cluster effect can now be studied.

3. Results and discussion

The improved experimental method has allowed observation of clearer cluster effects than before, especially at low-energy region of the electron spectra. Figure 1 shows the energy spectra of electrons emitted from highly-oriented pyrolytic graphite (HOPG) bombarded by 0.50 MeV/atom C (n=1, 4, 8). The yields for the two targets are shown for the same number of the incident C atoms for comparison of the spectra per projectile atom.

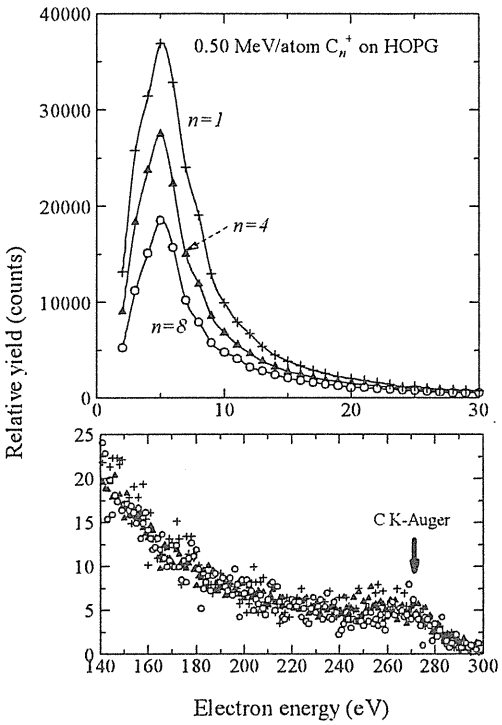

Fig. 1 Energy spectra of the C_n^+-induced electrons from HOPG (TIARA data).

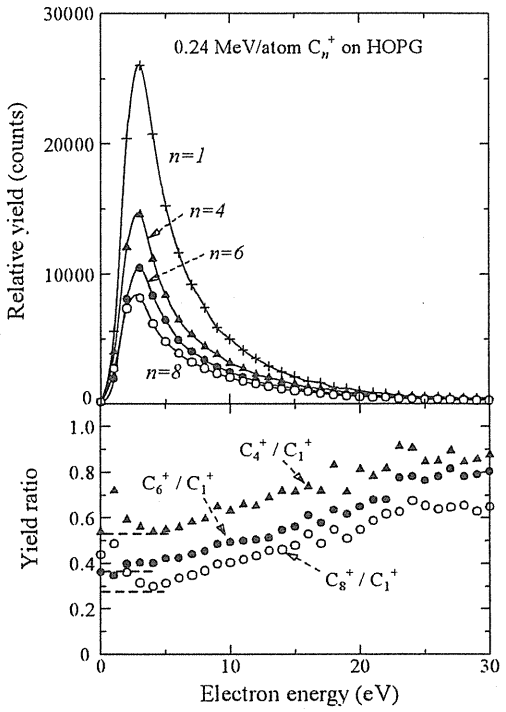

Fig. 2 Energy spectra of the C_n^+-induced electrons from HOPG (UTTAC data).

Figure 2 shows the results for 0.24 MeV/atom C_n (n=1, 4, 6, 8) incident on the HOPG target. In Figs. 1 and 2, the yield at low energies is appreciably reduced with increasing n, relative to the case of n=1. The yield ratios take minimum values at 0–10 eV, increase with increasing the electron energy, and become ~1.0 at energies typically higher than hundred-electron-volts. The absence of the cluster effect with the high-energy electrons stems from the fact that these electrons, including the C K–shell Auger electrons in Fig. 1, are originated from close encounter between the cluster atoms and the target electrons. Because of the small probability for the close encounters, the target electrons interact effectively with only one of the cluster atoms, rather than with multiple atoms in the cluster, so that there is no cluster effect for the production of high-energy electrons.

In contrast, the electrons of 0–10eV stem mainly from the distant collisions between the cluster and the target atoms near the surface layer. The middle range of the electron energy, for example, at 10–50 eV, corresponds to the intermediate case of the electron emission resulting from the interaction of the target electrons partially with the cluster atoms. The ratios of the spectra can therefore be interpreted in terms of the amount of energy transfer to the target electron, which can be associated with the classical impact parameter.

Baudin and coworkers pointed out that the sublinearity of the electron emission results from the electron–presweep mechanism in the cluster-solid collision processes.[4] Indeed, the front atom in the cluster sweeps out the weakly–bound target electrons and, accordingly, the following atoms in the cluster ionize only the reduced number of weakly–bound electrons. If the available number of the weakly–bound electrons reduces by a factor of $1-\omega$ per presweep, the reduced yield ratio R_n for n=1 can be expressed as[2-4]

$$R_n=[1-(1-\omega)^n]/n\omega . \quad (1)$$

The electron–presweep model provides an insight into the understanding of the present results. We may obtain the values of ω satisfying Eq. (1) for the observed values of R_n, which is indicated by the dashed lines in Fig. 2, for example. Notably, the set of R_n values can be reproduced by a unique value of ω for a given pair of the target and the equal-velocity cluster species. For example, the observed values R_4 =0.53±0.03, R_6=0.36±0.03, and R_8=0.27±0.04 for 0.24 MeV/atom C_n^+ incident on HOPG can be reproduced by the unique value of $\omega \cong 0.44$.

However, for a given target and ion species, the value of ω for 0.50 MeV/atom is greater than that for 0.24 MeV/atom. This is apparently inconsistent with the ion-energy dependence of the cluster effect expected from the meaning of ω, i.e., the ratio of the ionization cross section for the single-ion impact (n=1) to the effective size of the track of the cluster, which was proposed previously by Baudin and coworkers. For the present experimental parameters, the ionization cross section increases with increasing the ion energy, and therefore, ω should increase, i.e., R_n should decrease as the ion energy increases. Nevertheless, it appears from the present analysis that the electron–presweep model should essentially describe the cluster-induced electron emission if a reasonable definition of the parameter ω is given.

4. Concluding remarks

The dependence of energy spectra of cluster-induced electrons on the number of cluster atoms has been observed. The energy spectra at 0–10 eV reflect the interaction of the cluster with the target electrons up to a depth of ~100 Å, while the cluster effect is hardly seen beyond the hundred electron-volt energy range. The n dependence of the electron yield might be explained by the electron–presweep picture based on the single parameter ω which describes the reduced electronic interaction of clusters, although its physical meaning is not yet well understood. The electron–presweep model also predicts effective suppression of the electron emission as n increases.

From a viewpoint of the correlation between the electron emission and the electronic energy loss, we may anticipate that the cluster should experience considerably reduced stopping powers, for example, by a factor of typically 0.5 or less even in the present experimental conditions. The experimental as well as theoretical investigations of the behavior of large n clusters are of fundamental interest for a better understanding of the cluster-solid electronic interactions.

The electron–presweep picture is physically the same as the time-independent interaction of electrons with the multi-center Coulomb field by the cluster atoms.[5] Both approaches may be possible to describe the cluster effects in the electron emission.

References

1) D. Jacquet, Y. Le Beyec, Nucl. Instrum. Methods B 193 (2002) 227-239.
2) E. Parilis, Nucl. Instrum. Methods B 193 (2002) 240-247.
3) H. Kudo, *Ion-Induced Electron Emission from Crystalline Solids* (Springer, Berlin, Heidelberg, 2002), Chap. 5.1.
4) K. Baudin, A. Brunelle, S. Della-Negra, J. Depauw, Y. Le Beyec, E. S. Parilis, Nucl. Instrum. Methods B 117 (1996) 47-54.
5) T. Kaneko, Phys. Rev. A66 (2002) 052901 -1-13.

4.13 Application of X-ray Photoelectron Spectroscopy to Characterization of Metallic Nanoclusters Formed by Ion Implantation

K. Takahiro*, A. Terai*, T. Morikawa*, K. Kawatsura*, S. Yamamoto** and H. Naramoto***

Department of Chemistry and Materials Technology, Kyoto Institute of Technology*

Department of Materials Development, JAERI**

Advanced Science Research Center, JAERI***

1. Introduction

A nanometer-sized cluster, referred to as "nanocluster" hereafter, embedded in a matrix exhibits unusual optical[1], electrical[2], and magnetic[3] properties. A large number of methods, including co-sputtering, sequential evaporation, sol-gel deposition and ion implantation have been applied to preparation of nanoclusters in a matrix. Ion implantation is very promising for the formation of nanoclusters because of its ability to control the type and concentration of the implanted atoms. In addition, ion implantation can be, in principle, applied for any combination of ions and matrices.

Usually implanted atoms as well as defects do not distribute uniformly along depth, resulting in the depth-dependent nucleation and growth of nanoclusters. It is, therefore, necessary to examine the depth-dependent size distribution of nanoclusters. Cross sectional transmission electron microscopy (XTEM) is often used to directly investigate their size. However, much effort and time have to be paid to prepare good specimens for XTEM observation. Alternatively, there are some spectroscopic techniques, such as optical absorption measurement and X-ray diffraction (XRD) to estimate the size of nanoclusters embedded in a matrix. In these techniques, X-ray photoelectron spectroscopy (XPS) is a sensitive technique to investigate electronic structure, and hence the size, of nanoclusters. The size of a nanocluster affects on its electronic structure.

In this study, Au, Ag or Cu ions are implanted into glassy carbon (GC), because such metallic atoms are immiscible in carbon and metallic nanoclusters will be formed in GC.

2. Experimental procedure

Glassy carbon (Tokai Carbon, Japan; GC-30 grade) was mechanically polished to mirror surface with 1 μm diamond slurry on a cloth lap. Au^+ ions with an energy of 600 keV were implanted to a dose of 4×10^{16} cm^{-2} at room temperature. Au implantation was performed using a tandem accelerator at Institute for Materials Research (IMR), Tohoku University. 350 keV Ag^+ ions were implanted to a dose of 1×10^{17} cm^{-2} at room temperature using the ion implanter at TIARA. The depth distributions of implanted atoms were analyzed by using Rutherford backscattering spectrometry (RBS) with 2 MeV He ions from the tandem accelerator at IMR. The projected ranges of 600 keV Au and 350 keV Ag ions were approximately 300 nm and 140 nm, respectively.

XPS analysis using non-monochromatized Mg Kα radiation was performed with JEOL 9010. To obtain depth profile of XPS binding energies for the implanted atoms, the surface of implanted GC samples was etched with 0.8 keV Ar ions produced by a sputter-etching gun, which is equipped with JEOL 9010. The etching rate was typically 0.24 nm/sec in the XPS analysis for Ag.

In case of the analysis for Au, unfortunately, the etching rate could not be controlled. Therefore only two points at depths of ~240 nm and ~360 nm are analyzed in that case.

3. Results and discussion

Figure 1 shows Au 4*f* core-level XPS spectra obtained from Au atoms implanted at depths of ~240 nm and ~360 nm. The Au implantation dose was 4×10^{16} cm^{-2}. The spectrum from a bulk Au sample is also shown for comparison The peak positions of $4f_{7/2}$ and $4f_{5/2}$ levels for the implanted Au at both depths shift towards higher binding energy by 0.4 eV compared to those for the bulk Au. The energy shift can be understood by the effect of an averaged coordination number or a cluster size on core-level binding energy[4]. The average size of the Au clusters was estimated to be 1.4 nm from an empirical relationship between the size and energy shift derived from the literature[4]. The width of the 4*f* lines of the spectra for the implanted Au at both depths was 2.2 eV, relatively larger than that for the bulk Au (1.2 eV). Indeed, the linewidth for thenanocluster increases with decrease in its size, since the atoms involved in the nanocluster have various coordination numbers[4),5]. In addition to the above effect, such a large broadening shown in Fig. 1 suggests the presence of small Au nanoclusters with various sizes[6] in the analyzing layers. Another possibility for the line broadening will be described below.

In Fig. 2, Ag $3d_{5/2}$ core level binding energies are plotted as a function of sputtering time. The depth profile of Ag concentration is also shown in this figure. The sputtering time of 600 sec corresponds to the analyzing depth of ~140 nm, at which maximum Ag concentration is obtained. The Ag $3d_{5/2}$ core level binding energies for the implanted Ag are higher than that for the bulk Ag (368.3 eV), indicating the existence of relatively small-size Ag clusters. Wertheim and DiCenzo[7] found that Ag 3*d* core level binding energy increases with decreasing the coverage of Ag atoms deposited onto an amorphous carbon substrate. Their findings show that the Ag 3*d* core level binding energy increases with decreasing the size of an Ag cluster, because the size of an Ag cluster tends to decrease with decrease in the coverage of deposited Ag atoms. To the best of our knowledge, the relationship between the

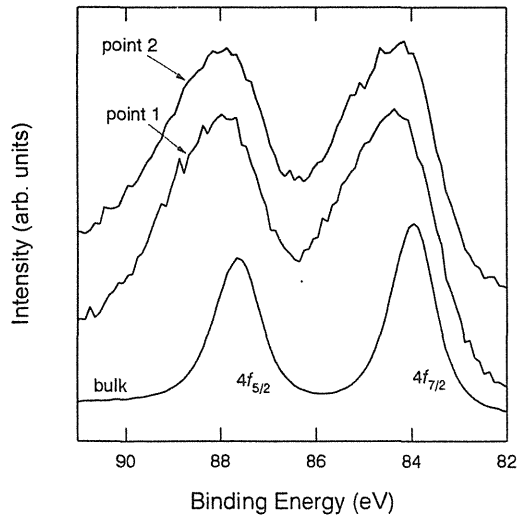

Fig. 1. Au 4*f* core level XPS spectra for implanted Au in GC at ~240 nm (point 1) and ~360 nm (point 2). The XPS spectrum for a bulk Au sample is also shown for a comparison (bulk).

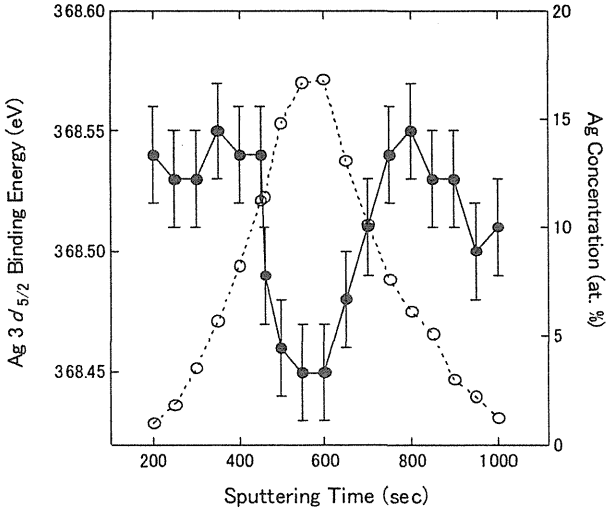

Fig. 2. Ag $3d_{5/2}$ core level binding energies (closed circles) together with Ag concentrations (open circles) as a function of sputtering time. The Ag $3d_{5/2}$ core level binding energy for the bulk Ag is 368.3 eV

binding energy and size of an Ag nanocluster is unavailable. Hence we shall discuss qualitatively the Ag concentration dependence of the size of an Ag nanocluster.

We examine the size of the Ag clusters in three distinct regions in Fig. 2, including the surface region, corresponding to the sputtering times, t, of 200-400 sec, the region near the projected range (t: 400-800 sec), and the region in the vicinity of the end of range (t: 800-1000 sec). In the regions of surface and near the end of range, the Ag concentrations are 1-10 at. %. In these two regions, the Ag $3d_{5/2}$ binding energies are found to be independent of the Ag concentration, almost constant at 368.50-368.55 eV. Suppose that binding energy of an Ag cluster depends only upon its size, the sizes of the Ag clusters do not vary with the Ag concentration in these regions. On the contrary, in the region near the projected range, the Ag $3d_{5/2}$ binding energy decreases as the Ag concentration increases up to ~17 at. %. This tendency indicates that the Ag clusters coalesce each other to form larger size clusters in this region. In fact, larger size Au clusters in a SiO_2 matrix were observed with XTEM in the region near the projected range[8], which supports our interpretation.

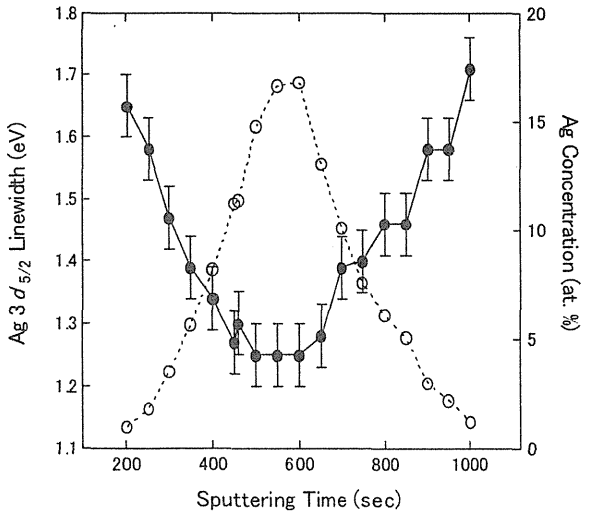

Fig. 3. Ag $3d_{5/2}$ line widths (closed circles) together with Ag concentrations (open circles) as a function of sputtering time. Ag $3d_{5/2}$ line-width for the bulk Ag is 1.1 eV

Figure 3 shows the Ag $3d_{5/2}$ linewidths, as well as the Ag concentrations, as a function of sputtering time. Note that the Ag $3d_{5/2}$ linewidth of the bulk Ag sample was 1.1 eV. The depth profile of the Ag $3d_{5/2}$ linewidth was found to strongly correlate with that of the Ag concentration. The lower Ag concentration results in the broader linewidth. Considering that the Ag $3d_{5/2}$ binding energies, and hence the size of Ag clusters, are independent of the Ag concentration in the region of surface and near the end of rang, the linewidth may not be related to the size or size distribution of Ag clusters, but to the Ag concentration only. The line broadening can be understood by a local charging[9] of the Ag clusters. The local charging effect would be remarkably observed on the low concentration Ag clusters. Further investigations are needed to clarify the origin of the line broadening.

References

1) R. Ruppin, J. Appl. Phys. 59 (1986) 1355-1359.
2) G. Medeiros-Riberro, D. A. A. Ohlberg, R. S. Williams and J. R. Health, Phys. Rev. B 59 (1999) 1633-1636.
3) G. L. Zhang, W. H. Liu, F. Xu and W. X. Hu, Appl. Phys. Lett. 61 (1992) 25272529.
4) S. B. DiCezo, S. D. Berry and E. H. Hatford Jr, Phys. Rev. B 38 (1988) 84658468.
5) P. Zhang and T. K. Sham, Phys. Rev. Lett. 90 (2003) 245502-1 - 245502-4.
6) T. T. P. Cheung, Surf. Sci. 140 (1984) 151-164.
7) G. K. Wertheim and S. B. DiCenzo, Phys. Rev. B 37 (1988) 844-847.
8) G. Mattei, Nucl. Instr. Meth. B 191 (2002) 323-332.
9) Y. Uwamino and T. Ishizuka, J. Electron Spectrosc. Relat. Phenom., 23 (1981) 5562.

4.14 Effects of Ion Irradiation on Electrochemical Hydriding Rate of Misch Metal-based Alloys

H. Abe*, H. Uchida**, R. Morimoto**, F. Satoh** and T. Kamiya*
Department of Material Development, JAERI*
Faculty of Engineering, Tokai University**

1. Introduction

Misch metal (Mm)-based alloys have been applied to the negative electrodes of the Ni-H batteries, etc., in recent years because of their excellent hydrogen storage properties. In order to apply such alloys to hydrogen storage system in automobiles, further improvement of their hydrogen storage properties is indispensable. Surface modifications are crucial for improving the absorption of hydrogen into metals because the dissociation of H_2 molecules in the gas phase or the dissociation of H_2O molecules in electrochemical process, which is the first step of the overall reaction of hydrogen absorption in metals[1], can be influenced by the surface states. So far, we have systematically investigated the effects of surface oxide layers on the hydrogen absorption in metals[1, 2] as well as the influences of surface modifications such as metallic coatings[3], fluorination treatments[4, 5] and alkaline treatments[6].

In this study, the surface modification of Mm-based alloys was performed by ion irradiation using proton (H^+), argon (Ar^+) and potassium (K^+), and the effects of this modification on the rate of electrochemical hydriding were investigated. Ion irradiation onto the surface of a metal effectively induces defects such as vacancies, dislocations and micro-cracks in the surface region of the metal. As well known, vacancies trap hydrogen atoms. The hydrogen trapping was reported to result in a marked increase in the hydrogen solubility in Pd[7, 8] or $LaNi_5$[9, 10]. It was also reported that hydrogen trapping sites act as the center of segregation of hydrides even in hydrogen solid solution region[11], and that oxide/metal interfaces tend to act as hydrogen trapping sites and form hydrides[12, 13]. Based on these facts, we have investigated the effects of ion irradiation on the initial rate of hydriding of Mm-based alloys in electrochemical process.

2. Experimental Procedure

The samples used in this study were $MmNi_{3.48}Co_{0.73}Mm_{0.45}Al_{0.34}$ (Mm = $La_{0.35}Ce_{0.65}$) pellets with a size of 13 mmϕ and 2 mm thickness. Ion irradiation was made with H^+, Ar^+ and K^+ at an acceleration energy of 350 keV in a dose range from 1 x 10^{14} to 1 x 10^{16} cm^{-2} using a 400 kV ion implanter at TIARA.

For the electrochemical measurements of hydriding rate of the unirradiated and ion irradiated samples, an Mm pellet was used as an anode. An Hg/HgO electrode was used as the reference electrode in an open cell[14]. The rate of hydriding of the sample was measured in a 6 M (*mol/l*)-KOH using the open cell at a constant voltage -0.93 V and at 298 K. Details of the measurements of the electrochemical hydriding rate has been reported elsewhere[14].

3. Results and Discussion

Figure 1 shows the hydriding curves of the Mm-based alloy samples irradiated at two different doses of 1 x 10^{14} to 1 x 10^{16} cm^{-2} of H^+ and Ar^+. The initial rate of all irradiated samples was high compared with that of the un-irradiated sample. At the initial stage (within 30 minutes from the start of each

reaction), the rate of irradiated samples was increased as the ion dose was increased from 1 x 10^{14} to 1 x 10^{16} cm^{-2}. Compared with the result of H^+, the samples irradiated with Ar^+ exhibited higher initial rates. Similar results were obtained for Pd metals[15]. It is derived from TRIM calculation that Ar^+ ions produce much higher concentrations of vacancy in the surface than H^+ ions. The higher concentrations of vacancy lead to increased numbers of hydrogen trapping sits, and resulting in the acceleration of the rate of hydride nucleation and growth in the surface region.

Figure 2 shows the result of K^+ irradiation effects on the hydriding rate of the Mm-alloy when the irradiation was made at an energy of 350 keV at a dose of 1 x 10^{16} cm^{-2}. In the measurements, hydrogen absorption and disorption were made 3 times repeatedly. The results obtained for K^+ irradiation are found to differ from those for H^+ and Ar^+ irradiations. That is, in comparison with the unirradiated sample, the irradiated sample exhibited a very high hydriding rate. In addition, the value of H/Mm in the irradiated sample at an elapsed time of 350 minutes was three times as high as that in the unirradiated one. Of the ions used in this study, the K^+ irradiation was found to be the most effective in improving the initial hydriding rate.

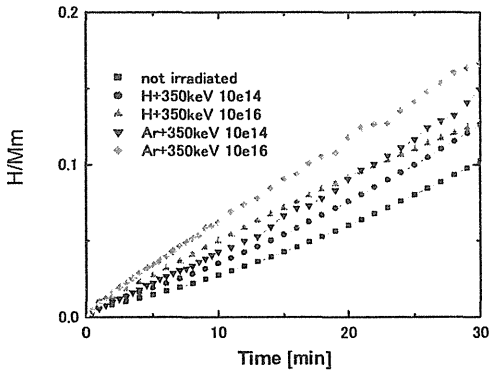

Fig.1 Hydriding curves of the Mm-based alloy irradiated with H^+ and Ar^+.

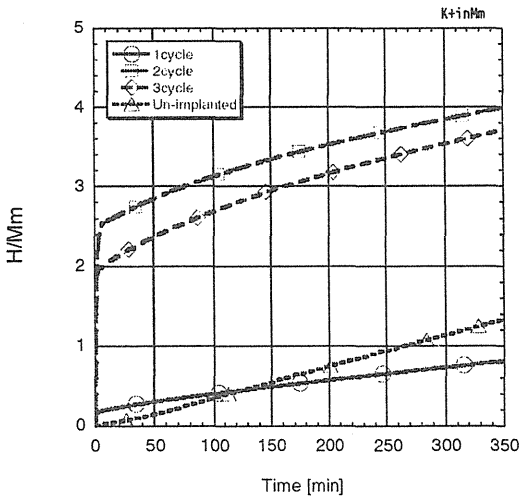

Fig.2 Hydriding curve of the Mm-based alloy irradiated with 350 keV-K^+.

The improvement of the hydriding rate of the Mm-based alloy due to K^+ irradiation cannot be explained only by the production of vacancy-type defects in the surface region. Chemical reactions with K atoms implanted near the surface might be related to the increase in the hydriding rate. Further investigations are necessary to clarify the mechanisms behind the improvement of the hydriding rate by K^+ irradiation.

References

1) H.Uchida, Int. J. Hydrogen Energy 24 (1999) 861-869.

2)H.Uchida, Y. Ohtani, M. Ozawa, T. Kawahata and T. Suzuki, J. Less-Common Met., 172-174 (1991) 983-996.

3) E. Fromm, Chap.6 "Poisoning of Hydrogen Reactions" in "Kinetics of Metal-Gas Interactions at Low Temperatures", Springer Verlag, Berlin, 1998, ISBN 3-540-63975-6, p. 126.

4) H. Uchida, T. Inoue, T. Tabata, S. Seki, H.H. Uchida, F. Aono, T. Nakazawa, H. Kikuyama and R. Hirayama, J. Alloys Comp., 253-254 (1997) 547-549.

5) H. Uchida, F. Aono, T. Iwamoto, T. Matsu, M. Ito, T. Nakazawa, T. Tabata and A. Kosuge,

Proc. 13th World Hydrogen Energy Conference 2 (2000) 1088-1092.

6) H. Uchida, K. Yamashita and M. Goto, J. Alloys and Comp., 330-332 (2002) 622-626.

7) H. Abe, A. Uedono, H. Uchida, A. Komatsu, S. Okada and H. Itoh, Mat. Sci. Forum 363-365 (2001) 156-158.

8) T. B. Flanagan, in "Progress in Hydrogen Treatment of Materials", ed. by V. A. Goltsov, pub. by Donetsk State Technical Univ., Ukraine, 2001, ISBN 966-7418-71-5, 37-45.

9) H. Uchida, A. Hisano, K. Terao, N. Sato and A. Nagashima, J. Less-Common Met., 172-174 (1991) 1018-1027.

10) S. Seta and H.Uchida, J. Alloys and Comp., 231 (1995) 448-453.

11) G. H. Kim, A. G. Lee, K. Y. Lee, C. H. Chun and J. Y. Lee, Acta Metall. Mater, 43, No. 6 (1995) 2233-2236.

12) Y. Ohtani, S. Hashimoto and H. Uchida, J. Less-Common Met., 172-174(1991) 841-850.

13) H. Uchida, S. Seki and S. Seta, J. Alloys and Comp., 231(1995) 403-410.

14) H.H. Uchida, Y. Watanabe, Y. Matsumura and H. Uchida, J. Alloys Comp., 231 (1995) 679-683.

15) H. Abe, H. Uchida, Y. Azuma, A. Uedono, Z. Q. Chen and H. Itoh, Nucl. Inst. and Meth. B, 206 (2003) 224-227.

4.15 Hydrogen Bubble Formation in H-implanted ZnO Studied using a Slow Positron Beam

Z. Q. Chen[*], M. Maekawa[*], A. Kawasuso[*], S. Yamamoto[**], X. L. Yuan[***], T. Sekiguchi[***], R. Suzuki[****] and T. Ohdaira[****]
Advanced Science Research Center, JAERI[*]
Department of Material Development, JAERI[**]
Nanomaterials Laboratory, National Institute for Materials Science[***]
National Institute of Advanced Industrial Science and Technology[****]

1. Introduction

Recently the behavior of hydrogen in ZnO has attracted much attention[1)], because not only it is a shallow n-type donor, but also it might improve the optical properties by increasing the UV emission efficiency. This is due to the passivation of the dangling bonds of intrinsic defects. However, up to now there is still a lack of fundamental knowledge about the interaction between hydrogen and defects, and their underlying relationship with the electrical and optical changes. Positron annihilation spectroscopy provides us a unique tool to study vacancy-type defects in semiconductors[2)]. In this paper, we incorporated hydrogen into ZnO by ion-implantation technique. The introduction and thermal evolution of defects and their interaction with hydrogen were studied by positron annihilation measurements. The effect of hydrogen implantation on the luminescence properties before and after annealing was also characterized by the cathodoluminescence measurements.

2. Experiment

ZnO single crystals (undoped n-type) with (0001) orientation were purchased from the Scientific Production Company (SPC goodwill). Hydrogen implantation was performed at room temperature with multiple energies ranging from 20-80 keV using a 400 keV implanter. The total implantation dose is around 4.4×10^{15} cm^{-2}. The implanted samples were annealed isochronally in a nitrogen ambient from 200 to 1100°C for 30 minutes. Doppler broadening of positron annihilation spectra were measured using a slow positron beam (0.2-30 keV). Positron lifetime spectra were also measured using a pulsed slow positron beam. The conventional S-parameter, which is defined as the ratio of the centra region to the total area of the 511 keV annihilation peak, is used to analyze the measured Doppler spectra. Cathodoluminescence spectra were measured using a modified scanning electron microscope (TOPCON DS-130). The electron beam energy and current for excitation were 5 kV and 1 nA, respectively, and the acquisition time for each measurement was 5 s.

3. Results and discussion

Figure 1 shows the Doppler broadening S-parameter as a function of incident positron energy for the ZnO sample before and after H^+-implantation. After implantation, the S-parameter increases in the energy region of 5-15

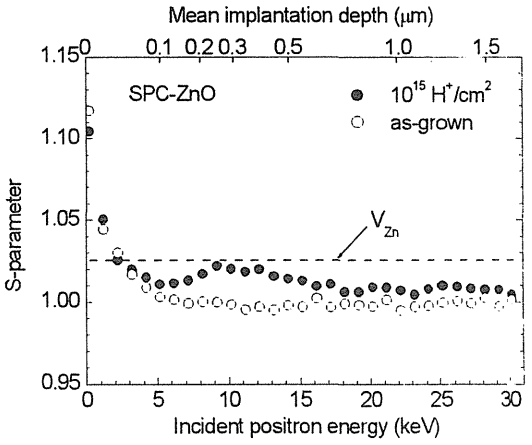

Fig.1 S-E curves measured for the ZnO before and after H^+-implantation.

keV. This means that H^+-implantation produces vacancy defects in ZnO. However, the S-parameter is in the range of 1.01-1.02, which is smaller than that of zinc monovacancies (1.025). The positron lifetime presented in Fig. 2 also shows very small increase from 182 ps to 202 ps after H^+-implantation, and it is clearly shorter than that of zinc vacancy (V_{Zn}), which is around 230 ps obtained from the previous electron irradiation measurements. This means that the vacancy size is smaller than that of V_{Zn}. It is apparent that hydrogen impurities are filled into these vacancies. This is supported by the theoretical calculation, which shows the decrease of positron lifetime after filling the hydrogen into V_{Zn}.

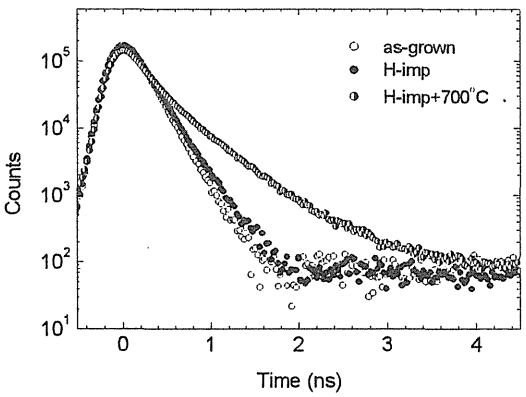

Fig.2 Positron lifetime spectra measured for the ZnO before and after H^+-implantation and 700°C annealing. The positron energy is 7 keV.

Figure 3 shows the average S-parameter in the positron energy range of 7-10 keV as a function of annealing temperature. After annealing, the S-parameter shows very interesting behavior. Three annealing ranges can be separated. From 200-500°C, the S-parameter shows slight increase. After annealing at 500-700°C, the S-parameter begins to increase quickly, and reaches the maximum value to over 1.17 at 700°C. After further annealing, the S-parameter decreases and reaches the bulk value at 1100°C. The small increase of S-parameter in the first stage is due to the agglomeration of vacancies into large vacancy clusters. But they are still filled with many hydrogen impurities, which are called hydrogen bubbles. Due to the occupation of the space in the bubble by these hydrogen atoms, the S-parameter does not show much increase. After annealing at 600-700°C, the hydrogen impurities began to be released from the bubble[3], and left empty microvoids. At this time, the positronium atom, which is a bound state of positron and electron, is formed in these voids. The para-positronium annihilation contributes a very narrow peak to the Doppler broadening spectra. This results in the quick increase of S-parameter. Detailed analysis of the Doppler broadening spectra confirms the formation of para-positronium. The positron lifetime also shows considerable increase after annealing at 700°C (Fig. 2). This is due to the annihilation of ortho-positronium in the microvoids. Therefore all the results suggest the formation of microvoids after release of hydrogen from the bubbles.

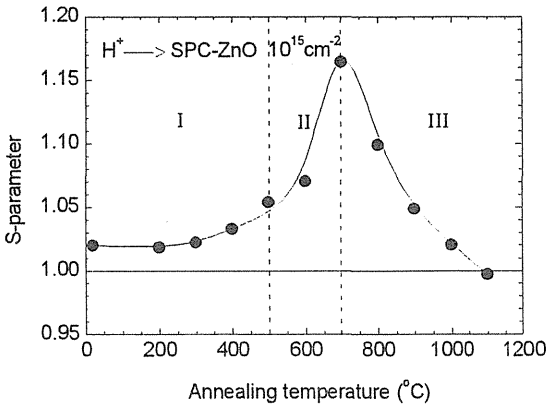

Fig.3 Annealing behavior of the S-parameter for the ZnO implanted with H^+.

The subsequent decrease of S-parameter above 700°C indicates recovery of these microvoids. After annealing at 1100°C, The S-parameter attains the bulk value, indicating that all the vacancies detected by positrons are removed.

The cathodolminescence measurements show that after H^+-implantation, both the deep level and UV emissions are greatly reduced. This is due to the introduction of nonradiative recombination centers. After 300°C annealing, the UV emission recovers, and becomes even stronger than that of the as-grown sample. This indicates that the nonradiative recombination centers are removed. However, the deep level emission is still very weak, which is possibly due to the passivation of the deep centers by hydrogen. Further annealing up to 600°C causes nearly no change of the spectra. At 700°C, the deep level emission shows increase, and as a result, the UV emission is weakened. This can be explained by the release of hydrogen, so the deep level emission centers are not passivated by these hydrogen impurities. However, further increase of the deep level emission at higher temperatures of 1000°C is not fully understood. It might be due to the production of additional deep level defects during high temperature annealing. Further detailed research is needed to clarify this deep level defect center.

References

1) C. G. Van de Walle, Phys. Rev. Lett. 85 (2000) 1012-1015.
2) R. Krause-Rehberg and H. S. Leipner, *Positron Annihilation in Semiconductors, Defect Studies*, Springer Series in Solid-State Sciences **127** (Springer, Berlin, 1999).
3) K. Ip, M. E. Overberg, Y. W. Heo, D. P. Norton, S. J. Pearton, C. E. Stutz, B. Luo, F. Ren, D. C. Look, and J. M. Zavada, Appl. Phys. Lett. 82 (2003) 385-387.

4.16 Surface Structure of Si(111) Studied by Reflection High-energy Positron Diffraction

Y. Fukaya, K. Hayashi, A. Kawasuso and A. Ichimiya
Advanced Science Research Center, JAERI

1. Introduction

The atomic coordinates and the thermal vibration state at the topmost surface are generally different from those of the bulk atoms, because the bonds are cut at surfaces and the surface atoms are rearranged. The coordinates and the vibration state are very important factors to investigate the mechanism of the surface phase transition and the adsorption of atoms or molecules. It is necessary to accurately determine these factors without any influence of the bulk. Then, we tried to study the topmost surface using reflection high-energy positron diffraction (RHEPD)[1].

When the positron beam with positive charge is incident on the surface at low glancing angle, the total reflection takes place below a critical angle[2]. The positrons hardly penetrate the bulk region under the total reflection condition and hence are diffracted only at the topmost layer. Thus, we can determine the atomic positions and the thermal vibrational amplitudes of the topmost surface from the analysis of the totally reflected intensities. Also, under the total reflection condition, the effect of the multiple scattering on the diffraction intensity is expected to be suppressed. Therefore, it is possible to analyze the RHEPD intensity within the kinematical approximation, as opposed to the electron diffraction.

In this study, we present the RHEPD pattern from the Si(111)-7x7 surface and show the pattern analysis by means of the dynamical and kinematical diffraction theories. Furthermore, we measure the temperature dependence of the RHEPD intensities from the Si(111)-7x7 surface and determine the Debye temperature and the thermal vibrational amplitudes of the topmost atoms.

2. Experimental procedure

2.1 Sample preparation

The samples with a dimension of 5 x 0.5 x 15 mm^3 were cut from *n*-type Si(111) wafer with resistivity of 1-10 . cm. They were degassed at 700 K for several hours, followed by the flashing at 1500 K for 10 s a few times. The temperature (*T*) was measured by an infrared thermometer. The clear 7x7 pattern was confirmed by reflection high-energy electron diffraction (RHEED).

2.2 RHPED measurement

All experiments were carried out in ultra-high vacuum chamber equipped with a positron source of ^{22}Na (370 MBq) and electrostatic lens system at TIARA. The details of the RHEPD apparatus were described elsewhere[3]. The accelerating voltage of the incident positron was set at 20 kV. The glancing angle was adjusted by rotating the sample mounted on a manipulator. Hereafter, . and . stand for the glancing angle and the deviation angle from the [$11\bar{2}$] direction.

3. Results and Discussion

3.1 RHEPD pattern analysis[4]

Figure 1 shows the RHEPD pattern from the Si(111)-7x7 surface at . = 1.1°, where the total reflection takes place. In this case, the critical angle of the total reflection can be estimated to be 1.4° using the Snell's equation. In addition to

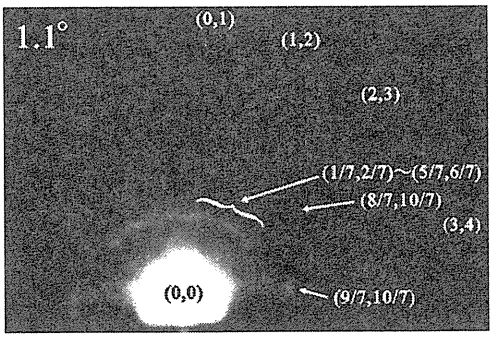

Fig. 1 RHEPD pattern from the Si(111)-7x7 surface (. = 1.1°, . = 0°).

the much intense (0,0) spot, some fractional order spots in the 1/7th, 2/7th, and 3/7th Laue zones can be observable. In particular, the intensities of (1/7,2/7) to (5/7,6/7), (9/7,10/7), and (8/7,10/7) spots are high. Also, the spot intensities in the 1st Laue zone are very weak. In the total reflection region, they are observable as common features.

When analyzing the RHEPD patterns by means of the kinematical and dynamical diffraction theories using the atomic coordinates of the 7x7 structure, we found that the measured patterns can be qualitatively explained by the kinematical calculation. However, the agreement between the measured and calculated patterns by the dynamical calculation is more superior to that by the kinematical calculation. Thus, the multiple scattering effect is necessary to quantitatively analyze the measured patterns. From the result due to the detailed analysis of the patterns, we found that the shift of the adatom height towards the surface-normal direction improved the discrepancy in the experiment, as reported in Ref. [5]. Furthermore, the penetration depth of the positron beam is estimated to be 1-2 Å[4].

3.2 Temperature dependence of RHEPD intensities[6,7]

Figure 2 shows the temperature dependence of the RHEPD intensities under various conditions. The (0,0) spot intensity gently decreases with increasing temperature. However, the (1,1) spot intensity drastically decreases with temperature. This is because the magnitude of the scattering vector for the (1,1) spot is larger than that for (0,0) spot and the attenuation of the intensity is enhanced. Similar to it, the intensity at 3.5° satisfying the (444) Brag reflection drastically decreases with temperature.

Owing to the preliminary result of the dynamical calculation, the spot intensity under the total reflection condition depends only on the Debye temperature of the surface atoms and the spot intensity outside the total reflection condition mainly reflects the Debye temperature of the bulk atoms. Actually, we determined the Debye temperature of the surfacre atoms as 290 K from the analysis of the temperature dependence of the (1,1) spot in the total reflection region. This value is about 100 K smaller than that by the electron diffraction[8]. The thermal vibrational amplitude of the adatoms is estimated to be 0.14 Å at room temperature, which increases by a factor of 30 % compared with those reported before. Similar to

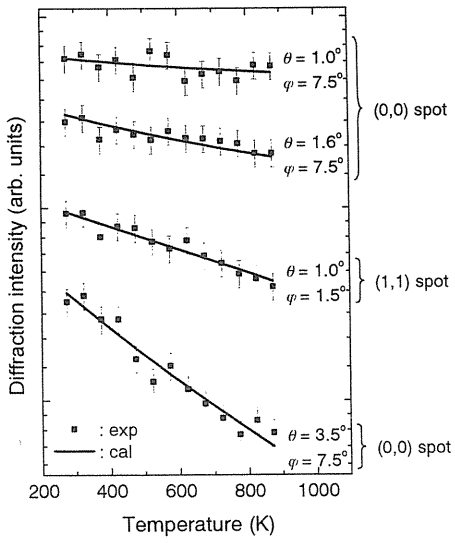

Fig. 2 Temperature dependence of the RHEPD intensities under various condition from the Si(111)-7x7 surface

it, the Debye temperature of the bulk is determined as 600 K, which is in good agreement with that by the x-ray diffraction analysis[9].

3.3 RHEPD rocking curve as a function of temperature[7]

Figure 3 shows the (0,0) spot intensity as a function of the glancing angle, so-called RHEPD rocking curve, up to 873 K. The measured rocking curve does not show any drastic change due to the increase in temperature. Only the intensity of the Bragg peak decreases with increasing temperature. However, the intensity in the total reflection region hardly decreases. These changes are consistent with the result in Fig. 2.

We calculated the RHEPD rocking curve based on the dynamical diffraction theory taking into account the thermal diffuse scattering. The adatom height above the first layer and the absorption potential due to the electronic excitation were taken as 1.52 Å and 0.25 V, respectively, which were determined in previous study[5]. The Debye temperature of the surface and the bulk were set at 290 K and 600 K, respectively, which were obtained in previous section. The calculated rocking curve denoted as the solid line is in good agreement with the measured curve. The reliability factor (R), which indicates the goodness of the fit, is below about 5 % in the whole temperature range. Therefore, the temperature dependence of the rocking curve can be explained by the enhanced Debye temperature of the surface, i.e., large thermal vibrational amplitude of the adatoms. Accordingly, the adatom height does not show significant shift with temperature. Consequently, we found that the adatom bond becomes softer even at room temperature.

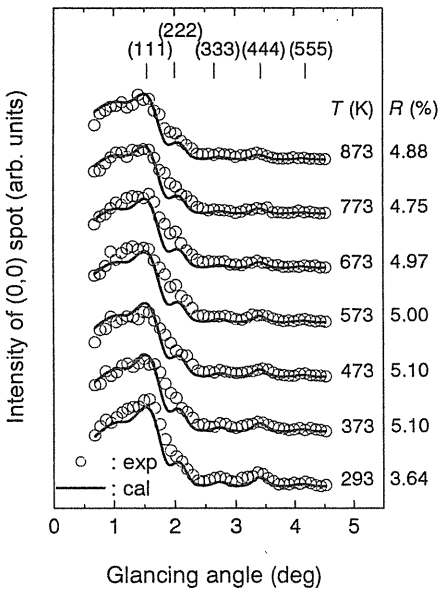

Fig. 3 RHEPD rocking curves from the Si(111)-7x7 surface up to 873 K. The open circle and the solid line show the measured and calculate rocking curves, respectively. The reliability factor (R) is labeled at the right-hand side.

References

1) A. Kawasuso and S. Okada, Phys. Rev. Lett. **81** (1998) 2695-2698.

2) A. Ichimiya, Solid State Phenom. **28&29** (1992/93) 143-148.

3) T. Ishimoto, A. Kawasuso, and H. Itoh, Appl. Surf. Sci. **194** (2002) 43-46.

4) K. Hayashi, Y. Fukaya, A. Kawasuso, and A. Ichimiya, Appl. Surf. Sci. (2004), in press.

5) A. Kawasuso, Y. Fukaya, K. Hayashi, M. Maekawa, S. Okada, and A. Ichimiya, Phys. Rev. B**68** (2003) 241313 (4 pages).

6) Y. Fukaya, A. Kawasuso, K. Hayashi, and A. Ichimiya, Appl. Surf. Sci. (2004), in press.

7) Y. Fukaya, A. Kawasuso, K. Hayashi, and A. Ichimiya, to be submitted.

8) Y. Fukaya, K. Nakamura, and Y. Shigeta, J. Vac. Sci. Technol. A**18** (2000) 968-971.

9) *International Tables for X-ray Crystallography, Vol. III*, edited by C.H. MacGillavry and G.D. Rieck (Kynoch, Birmingham, 1973), p. 234.

4.17 Application of Micro-PIXE to Study on Sorption Behavior of Heavy Elements on Mixtures of Minerals (2)

N. Kozai*, H. Mitamura*, T. Ohnuki**, T. Sakai***, M. Oikawa*** and T. Satoh***
Department of Environmental Sciences, JAERI*
Advanced Science research Center, JAERI**
Advanced Radiation Technology Center, JAERI***

1. Introduction

The purpose of this study is to understand migration behavior of heavy metals in soil environment. Soil is a mixture of various minerals such as clays, other silicates, iron (hydro)oxides, and phosphate minerals. To investigate sorption behavior of heavy metals on mixtures of minerals, this study used the micro-PIXE analyzing system developed in the TIARA facility, JAERI. The spatial resolution of the micro-PIXE analyzing system is less than 1 μm in diameter [1], which allows us to obtain highly sensitive two-dimensional elemental mapping images. The micro-PIXE analyzing system is thus suited for investigating distribution of elements sorbed on individual minerals in their mixture.

The related studies in JAERI have been carried out in qualitative fashion only. These studies have not evaluated influence of mineralogical features such as shape and size of minerals and location of elements in minerals on quantification of minerals and the sorbed elements. In this paper, applicability of micro-PIXE analysis to quantitative evaluation of the heavy elements sorbed on minerals was examined using external standards, which are heavy element-sorbing minerals of uniform shape and size. This paper describes the first result on sorption of Cd on external standards and application of the result to quantitative evaluation of the sorption of Cd on a mixture containing three minerals.

2. Experimental

2.1 Preparation of external standards

For preparation of Cd-sorbing external standards, fine powder of natural montmorillonite produced in Tsukinuno, Japan (Kunimine Industries Co., Ltd) was used. Montmorillonite is a representative swelling clay mineral commonly found in soil. A 0.1 g of the montmorillonite was contacted with 10 cm^3 of a Cd solution (10 mM $NaClO_4$ solution containing 0.1 to 10 mM $CdCl_2$) at 25°C. The starting pH of the Cd solution was adjusted at 5.0 using dilute NaOH and HCl solutions. After 24 hr, solid phase was separated from liquid phase by centrifuge. The liquid phase was further filtrated using a membrane filter with a pore size of 0.2 μm. Cd concentration in liquid phase was determined by ICP-AES and ICP-MS. The solid phase was washed with ethanol three times and dried in the air. The concentration of the sorbed Cd in montmorillonite, C_m, was determined by $(C_0\text{-}C)V/W$, where C_0 and C are the initial and final concentrations of Cd in solution, respectively, V is the volume of solution, and W is the weight of montmorillonite.

2.2 Sorption of Cd on mixture of minerals

A mixture of three minerals was prepared. This mixture contained the natural montmorillonite 80 wt%, a synthetic iron (III) hydroxide (ferrihydrite) 10 wt%, and a synthetic calcium-phosphate hydroxide (hydroxyapatite) 10 wt%. The ferrihydrite was prepared

according to the method by Schwertmann and Cornell[2]. The particle size of the ferrihydrite was between 25-46 μm. The hydroxyapatite was a synthetic spherical shape powder with the size of 20 μm in diameter (Bio-Rad Laboratories Inc.). A 0.04g of the mixture and 4 cm^3 of a Cd solution (10 mM $NaClO_4$ solution containing 1mM $CdCl_2$) were contacted in a centrifuge tube at 25°C. The starting pH of the Cd solution was adjusted at 5.0 using dilute NaOH and HCl solutions. After 10 min, solid phase was separated from liquid phase by centrifuge. The liquid phase was further filtrated using a membrane filter with a pore size of 0.2 μm. Determination of the Cd concentration in the liquid phase and wash of the solid phase were carried out as described above.

2.3 Micro-PIXE analysis

The Cd-sorbing samples were spread on a carbon plate using water and dried in the air. Two-dimensional elemental distribution of the Cd-sorbing sample on a carbon plate was then measured by micro-PIXE using a proton beam with the energy of 2.6 MeV. Lα X-ray of Cd (3.13 KeV), Kα X-rays of Si (1.74 KeV), Fe (6.40 KeV), and Ca (3.69 KeV) were analyzed for the sorbed Cd, montmorillonite, ferrihydrite, and apatite, respectively. To detect these X-rays, a high purity Ge detector with a crystal size of 100mm^2 (ORTEC IGLET-X) and a Si(Li) detector with a crystal size of 30 mm^2 (PGT LS-30135) were used at the same time. Those detectors have different sensitivity to and resolution in energy of X-ray. The Ge detector has a higher performance than the Si(Li) detector in detection of X-ray with energy higher than several KeV. On the other hand, the Ge detector is inferior to the Si(Li) detector in detection of X-ray with low energy. For the Si in the matrix of montmorillonite, the net count of Si Kα X-ray detected by the Si(Li) detector was about eight times greater than the net count detected by the Ge detector.

3. Results and discussion

From the EDS spectra for the external standards, the net counts of the peak areas of the Si in the montmorillonite and the sorbed Cd were obtained. The ratio of the net counts of Cd and Si, Cd/Si, was plotted in Fig. 1 as a function of C_m. In the C_m range between about 6 and 42 mg-Cd/g-montmorillonite, the value of Cd/Si increased linearly with C_m. The linearity of the correlation was particularly good when the Si(Li) detector was employed. This result indicates that the Cd sorbed on montmorillonite can be quantitatively evaluated in the above-mentioned C_m range by using the Si(Li) detector. In this C_m rage, about 10-65 % of the cation exchange sites of the montmorillonite were occupied by Cd^{2+}.

In the sorption experiment of Cd on the mixture containing montmorillonite, ferrihydrite, and apatite, 3.2×10^{-6} mol of Cd was sorbed on the mixture. Figure 2 shows two-dimensional elemental mapping images for the Cd-sorbing mixture sample. In Fig. 2, Cd was clearly detected in the areas where Fe and Ca were distributed. Correlation between the distribution of Cd and Ca was particularly good, suggesting that Cd was accumulated on apatite. On the other hand, correlation between the distribution of Cd and Si was not clear, suggesting that the concentration of the sorbed Cd in the montmorillonite was low. To evaluate this result quantitatively, the averaged value of the ratio Cd/Si measured by the Si(Li) detector was obtained for eight narrow areas where montmorillonite was distributed separately from ferrihydrite and apatite. Using the averaged value of Cd/Si and the relation shown in Fig. 1, the amount of the Cd sorbed on the montmorillonite in the mixture was found to be $1.9 \times 10^{-6} \pm 0.4 \times 10^{-6}$ mol. This amount of Cd

accounts for about 60 % of the Cd sorbed on the mixture ($3.2x10^{-6}$ mol). Because the content of montmorillonite in the mixture was 80 %, it can be said that Cd was somewhat accumulated onto the ferrihydrite and the apatite in the mixture.

It was found that the quantitative analysis using external standard was effective for better evaluation of the results on analysis of heavy metal sorbing minerals by micro-PIXE. The study on applicability of external standards continues for other heavy elements and minerals.

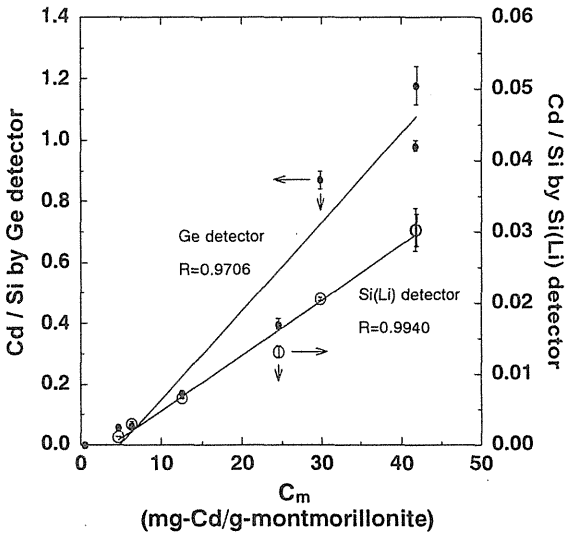

Fig. 1 Ratio of net counts of Cd and Si (Cd/Si) as a function of Cd concentration in montmorillonite (C_m)

References

1) T. Kamiya, T. Suda, R. Tanaka, Nucl. Instr. Meth. B, 118, (1996) 447/450
2) U. Schwertmann and R. M. Cornell, Iron Oxides in the Laboratory, VCH, New York (1991)

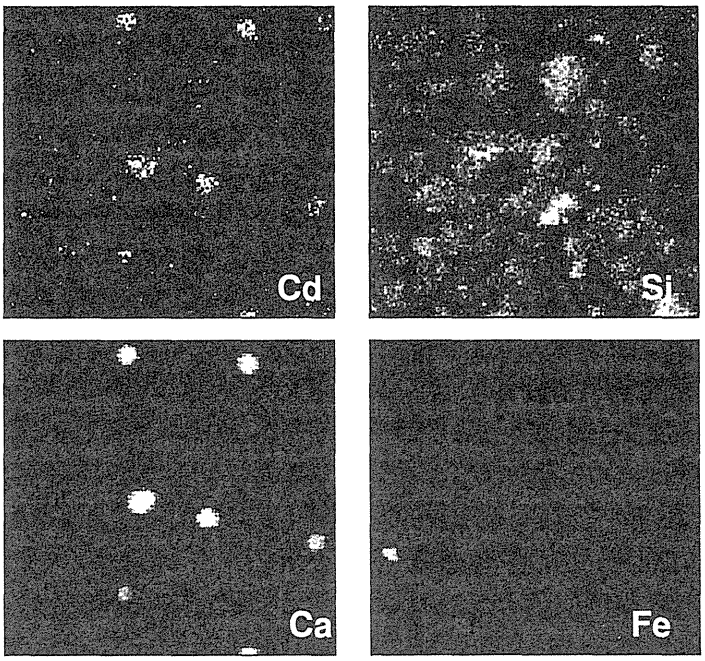

Fig. 2 Distributions of elements in Cd-sorbing mixture of montmorillonite (Si), ferrihydrite (Fe), and apatite (Ca) obtained by micro-PIXE. The above pictures indicate the same region (270x270μm) of the mixture spread on a carbon plate. A brighter region shows higher concentration of a given element.

This is a blank page.

5. Material Analysis

This is a blank page.

5.1 Hydrogen Up-take in Gas Ion Implantation Induced Porous Surface Layers

S. Nagata*, S. Yamamoto**, B. Tsuchiya*, K. Toh*, N. Ohtsu*and T. Shikama*
Institute for Materials Research, Tohoku University*
Department of Material Development, JAERI**

1. Introduction

It is well known that the ion irradiation of metals efficiently enhances the retention of hydrogen isotopes in the ion implanted region [1]. For endothermic hydrogen occluders such as Mo and W, having low solubility of hydrogen, the hydrogen atoms merely enter the crystal lattice, while dissociative adsorption can easily take place at the crystal surface. Recently, we found remarkable hydrogen accumulation by absorbing from the surrounding atmosphere into the He saturated surface of W and Mo single crystals [2,3]. Also, we observed a large isotopic difference of the up-take rates between hydrogen and deuterium[4,5]. However, mechanisms of the hydrogen up-take phenomena have not been clarified. We investigated the concentration depth profiles of up-taken hydrogen and morphological changes in the He, Ne, Ar, Kr, Xe ion implanted Mo and W single crystals. Although, the ion implantation caused different porous structures depending on the ion species, significant hydrogen up-take was found only for He and Xe ion irradiated surfaces [6]. In the present work, we examined hydrogen up-take and thermal release behavior in connection with compositional changes on the surface of Wand Mo single crystals implanted by various species of noble gas ions.

2. Experimental procedure

Specimens used were W and Mo single crystalline disks of 8 mm diameter and 0.5 mm thickness, with <100> or <111> crystallographic axis. They were cut from single crystal rods made by the floating zone melting method, and were electro-polished to obtain mirror like surface. Ion implantations were carried out using a 400 kV ion implantation facility at TIARA, with He, Ne, Kr, Xe ions of 50 ~ 280 keV, at room temperature. The maximum dose was about 2 x 10^{22} ions/m^2, with a typical current density of about 3 x 10^{18} ion/m^2s. During the ion implantation, the residual gas pressure was kept about 2 x 10^{-5} Pa. After the implantation, concentration depth profiles of hydrogen isotopes in the surface layer of the specimen were measured by Elastic Recoil Detection Analysis (ERDA) using 2.8 MeV He^{2+} beams. An ion beam with 1mm diameter was incident on the specimen at an angle of 75 degree to the surface normal and the recoiled He and hydrogen isotopes were detected at an angle of 30 degree with respect to the analyzing beam. The depth resolution of hydrogen in the present ERD experiments was estimated to be 25 nm at the surface of the specimen. Thermal release of hydrogen was investigated by measuring retained hydrogen in the specimen after each stage of isochronal annealing of 10 minutes.

Changes of the surface morphology due to the ion implantation were investigated by Scanning Electron Microscope (SEM) and Atomic Force Microscope (AFM) observation. The depth profile of metal, oxides and implanted spices are investigated Secondary Ion Mass Spectroscopy, using 10 keV Ga^+ beam. X-ray photoelectron spectrometry (XPS) was

performed using monochronized Al K α radiation to examine the implanted surface.

3. Results and Discussion

Fig. 1 shows time dependence of yields of secondary ions (W^-, WO^-, WO_2^-, WO_3^-) emitted from a W crystal surface irradiated by 10 keV He ions up to 1.5 x 10^{22} He/m^2, using 10 kV Ga^+ beam. Yields of each ion spices have a sharp peak at the beginning of the Ga^+ sputter, due to surface oxides. Indeed, WO_3 at the ion irradiated W surface were confirmed by XPS measurements. The secondary ion yields do not correspond to the absolute concentration of each metal or oxide, the shape of the concentration profiles is able to be compared with each other. The depth profile of W is similar to that of WO_3; the secondary ion yields of W and WO_3^- linearly decreased with increasing the sputtering time. On the other hand, the shape of WO^- yields curve coincides with that of WO_2^- yields; WO^- and WO_2^- signals had broad peak beneath the surface. During the Ga^+ sputter, intensities of secondary He ions sputtered from specimens were too low to be detected. Therefore we performed residual gas analysis for examining the depth profile of the implanted He in the same specimens. Fig. 2 shows residual gas yields of m/e = 2, 3 and 4 plotted against Ga^+ sputtering time. The sputtering time dependence of the He as indicated as m/e = 4, showed similar curve to the secondary ion yields of WO and WO_2. The larger yields of WO^- may not be directly connected with the formation of the WO, which is not believed to be stable. Although the quantitative analysis of the secondary ions yields are difficult, it can be stated that oxides of WO_2 were formed in the He retained depth region. We tried to measure depth profile of these oxides by XPS using Ar sputtering. However, the sputtered surface was

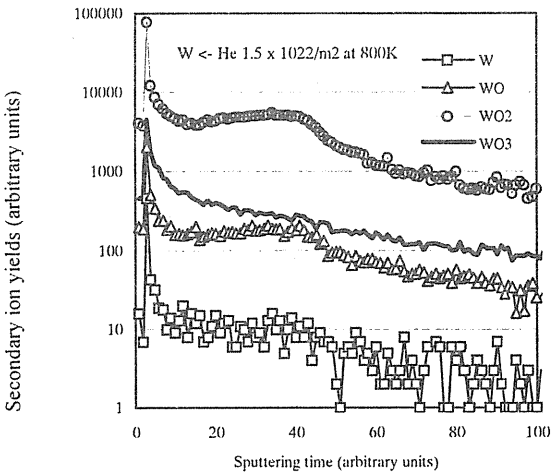

Fig. 1 SIMS depth profiles of W and W oxides from W single crystal irradiated by 10 keV He ions up to a dose of 1.5 x 10^{22}/m^2 at 800K.

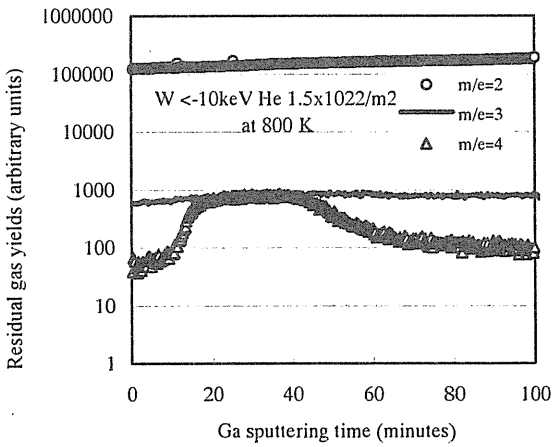

Fig. 2 RGA depth profiles of H and He from W single crystal irradiated by 10 keV He ions upto a dose of 1.5 x 10^{22}/m^2 at 800K.

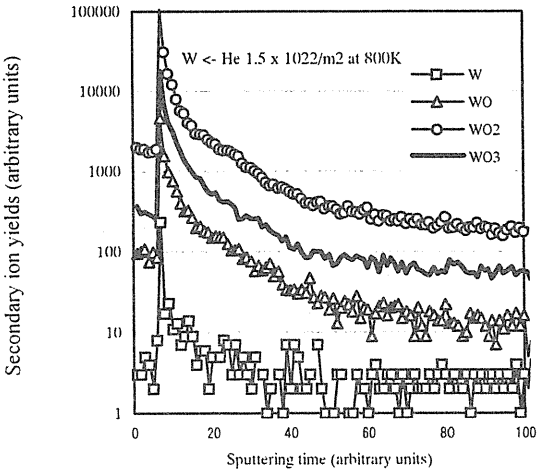

Fig. 3 SIMS depth profiles of W and W oxides from W single crystal irradiated by 200 keV Ar ions up to a dose of 1.5 x 10^{22}/m^2 at 800K.

immediately covered with WO_3 oxide layer probably due to the oxygen in the residual gas introduced by Ar sputtering procedure.

SIMS profile for the W irradiated by 200 keV Ar+ is shown in fig. 3. Relative intensities of secondary ions among W and W oxides are the same as those for the specimen irradiated by He, and the depth profiles for all W oxides are nearly the same. Similar profiles were obtained for Ne^+ irradiated W and Mo crystals. As reported in the latest annual review [6], the hydrogen up-take was found for He and Xe irradiated specimens, but not for Ne and Ar irradiated specimens. The results suggest that the up-take phenomenon is closely related to the WO_2 and MoO_2 formation along the ion range distribution.

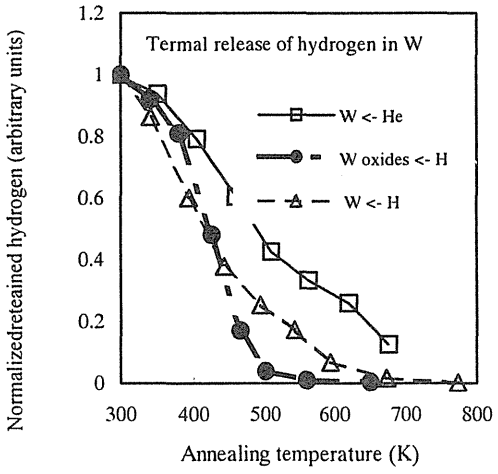

Fig. 4 Normalized retention of hydrogen in He irradiated W(□), in H implanted W (△) and H implanted oxide layer on W (●), during the isochronal annealing of 10 minutes.

Thermal release of up-taken hydrogen from the W crystal was compared with the release of ion implanted hydrogen, as shown in fig. 4. The up-taken hydrogen remained at higher temperature than that for implanted hydrogen. Especially, the release of implanted hydrogen was completed at 750 K from the oxide layer, which formed on the single crystal surface by annealing in air. Although, the oxide layer of W and Mo is able to retain large amount of implanted hydrogen, very little H up-take was observed by He and other noble gas irradiation.

4. Conclusions

Hydrogen up-take occurred in the He and Xe implanted depth region, where oxides such as WO_2 and MoO_2 were formed. Thermal release experiment indicated that the trapping of up-taken hydrogen was stronger than that of implanted hydrogen in the W and Mo metals and oxides. It can be concluded that enhancement of dissociation of the hydrogen is attributed to the oxides formed around the retained projectiles, and trapping of hydrogen atoms are related with the gas bubbles or clusters.

References

1) S.T. Picraux, J. Bottiger and N. Rud, Appl. Phys. Lett. 28 (1976) 179.
2) S. Nagata, B. Tsuchiya, T. Sugawara, N. Ohtsu, T. Shikama, Nucl. Instr. Meth. in Phys. Res. B 190 (2002) 652-656.
3) S. Nagata, B. Tsuchiya, T. Sugawara, N. Ohtsu, T. Shikama,, J. Nucl. Mater. 307-311 (2002) 1513-1516.
4) S. Nagata, B. Tsuchiya, N. Ohtsu, T. Sugawara, T. Shikama, K. Tokunaga, M. Takenaka, E. Kuramoto, J. Nucl. Mater., 313-316 (2003) 279-283.
5) S. Nagata, K. Tokunaga, B.Tsuchiya, N. Ohtsu, T. Sugawara, T. Shikama, J. Alloy. Compd. 356 (2003) 326-329
6) S. Nagata, S. Yamamoto, B. Tsuchiya, K. Toh, N.Ohtsu, T.Shikama, JAERI-Review 2003-033, (2003) 219-221

5.2 Photocatalytic Properties of Sulfur-doped Titanium Dioxide

T. Umebayashi*, S. Yamamoto**, M. Yoshikawa**, T. Yamaki** and K. Asai*
Department of Quantum Engineering and Systems Science,
The University of Tokyo*
Department of Material Development, JAERI**

1. Introduction

Since the early 1970s, TiO_2 has received attention as a promising photocatalytic semiconductor[1]. Extensive studies have been carried out for the realization of air and water purification systems using photocatalytic materials. TiO_2 has a wide optical bandgap of about 3.0 eV, i.e., a fundamental absorption edge of about 400 nm [2]. Therefore, the TiO_2 photocatalyst is active only under ultraviolet (UV) light, rendering it inactive under sunlight whose spectrum predominantly lies in the visible region. The effective utilization of visible light is one of the important subjects for the increasing applicability of this oxide as a photocatalyst.

Recently, the authors have performed the doping of sulfur (S) into TiO_2 [3]. The S-doping shifted its optical absorption edge to a lower energy, thereby increasing its photoreactivity under visible light. These previous studies demonstrated that the S-doped TiO_2 is expected to be applicable to novel photocatalytic reaction systems under the natural or solar beams. In this paper, we report the optical and photocatalytic properties of the S-doped TiO_2 synthesized by oxidative heating of the TiS_2 powder.

2. Methods

The TiO_2-based polycrystalline powder samples, including S substituted for O, were prepared by heating the TiS_2 powder in air at 500 .C for 90 min.

The crystal structures and surface areas of these samples were determined by X-ray diffraction analysis and the nitrogen-BET method. X-ray photoelectron spectroscopy (XPS) and diffusion reflectance spectroscopy (DRS) measurements were carried out to investigate the chemical states of S and the optical properties, respectively.

The photocatalytic activities were evaluated by measuring the optical absorption spectrum of methylene blue (MB) adsorbed on the surface of the pallets of the samples under the visible light irradiation (. = 420-500 nm).

3. Results and discussion

After the thermal treatment at 773K for 90 min, the color of the TiS_2 powder changed from black to beige. Figure 1 shows the XRD patterns of the prepared sample and the raw TiS_2 powder. A single phase of anatase TiO_2

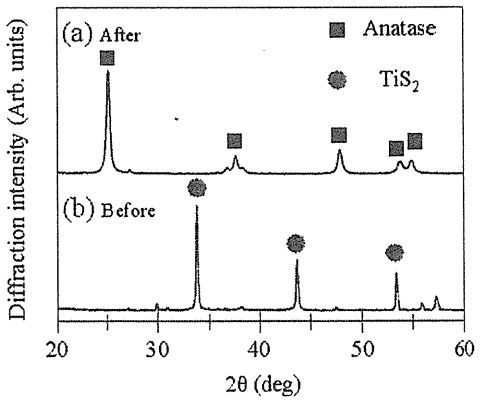

Fig. 1. XRD patterns of the TiS_2 powder (a) after and (b) before the thermal treatment at 500 .C for 90 min.

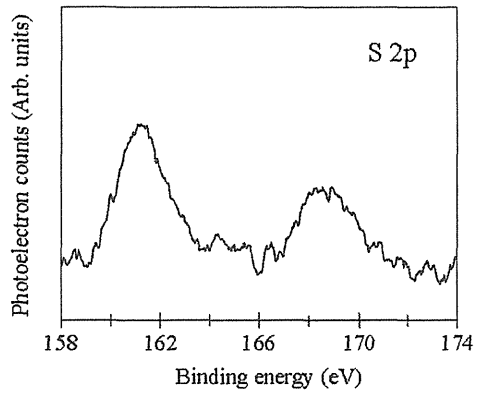

Fig. 2. S 2p core-level XPS spectrum of anatase TiO_2 synthesized by the heating of TiS_2 after the Ar^+ etching for 5 min.

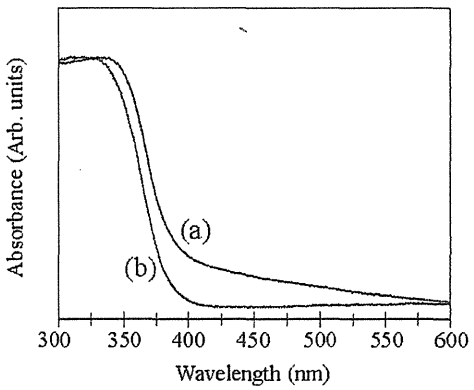

Fig. 3. DRS spectra of (a) S-doped TiO_2 synthesized by the heating of TiS_2, and (b) undoped TiO_2.

appeared in the former patterns. The crystal structure of the powder should be completely transformed into the anatase structure by the thermal treatment. The specific surface areas of the prepared sample and the reference TiO_2 powder were estimated to be ca. 33.5 and 41.2 m^2/g, respectively, by the BET method.

Figure 2 shows the XPS spectrum (S 2p core level) after Ar^+ etching (1 . /min) for 15 min of the anatase TiO_2 powders prepared by the annealing of TiS_2. As seen in the spectrum, a signal occurred around 160 eV. This signal is associated with S forming Ti-S bonds in the TiO_2 [3]. Therefore, a trace amount of S atoms would remain in the annealed sample as homogeneously distributed substitutional atoms at the O sites.

These XRD and XPS results indicated that the S-doped TiO_2 ($TiO_{2-x}S_x$), where the S atoms were substituted for the O atoms, was synthesized by oxidative heating of TiS_2. The concentration index of S, x: $TiO_{2-x}S_x$, was calculated to be ca. 0.01 by comparing the product of the 161 eV peak area multiplied by the S 2p sensitive factor to the product of the 531 eV peak area (O 1s) multiplied by the O 1s sensitive factor.

Figure 3 shows DRS spectra of the S-doped and undoped TiO_2. Due to the S-doping, the optical absorption edge was shifted into the lower energy region and visible-light absorption was enhanced. The present authors and some researchers reported the electronic structures (DOS: density of states) of the S-doped and undoped TiO_2 calculated by the band calculations using the full potential linearized augmented plane wave method [3), 4)]. These reports showed that the mixing of the S 3p states with VB increases the width of the valence band (VB) itself and narrows the bandgap. This would cause the lower energy shift and the absorption of visible light observed in the DRS spectrum of the S-doped sample.

Figure 4 shows the absorption spectra of the MB on the reference (undoped TiO_2) and S-doped sample under visible light irradiation. In the reference sample (Fig. 4 (a)), the change in the absorption intensity was not observed. On the other hand, the decrease in the absorption intensity and a slight blue shift of the spectrum were observed on the S-doped TiO_2 (Fig. 4 (b)). These are due to the decomposition (the former) and the N-demethylation (the later) of MB via the photocatalytic processes. This result undoubtedly means that the S-doped TiO_2 acts as a photocatalyst under the visible light irradiation.

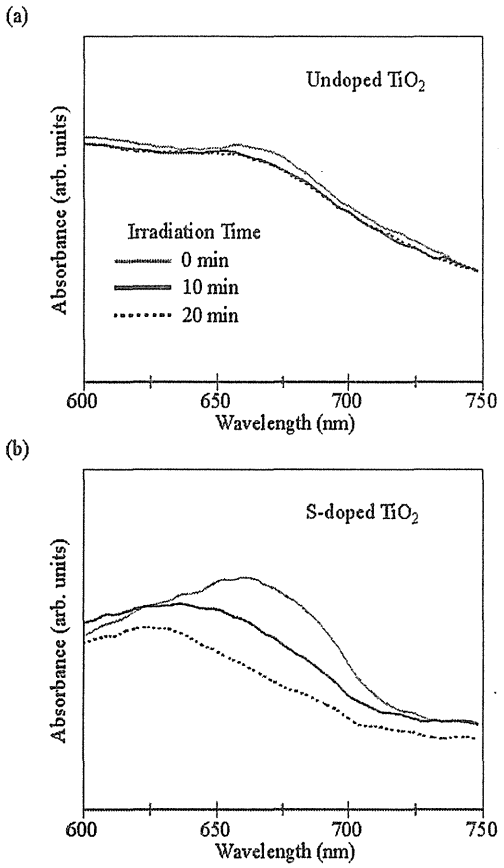

Fig. 4. Absorption spectra of MB on (a) undoped and (b) S-doped TiO_2 under visible-light irradiation (. =420-500 nm).

4. Conclusion

S-doped anatase TiO_2 was prepared by the annealing of TiS_2. The S-doped TiO_2 exhibited a red-shift in the optical absorption edge from the undoped TiO_2, consequently, the photoexcited carriers in the S-doped TiO_2 induced the photocatalytic decomposition of MB under the visible light irradiation. This compound should be effective as a novel visible-light photocatalyst.

References:

1) A. Fujishima and K. Honda, Nature 238 (1972) 37-38.
2) J. Pascual, J. Camassel, and H. Mathieu, Phys. Rev. Lett. 39 (1977) 1490-1493.
3) T. Umebayashi, T. Yamaki, H. Itoh and K. Asai, Appl. Phys. Lett. 81 (2002) 454-456.
4) R. Asahi, T. Morikawa, T. Ohwaki, A. Aoki, and Y. Taga, Science 293 (2001) 269-271.

5.3 C_{60}^+ Ion Irradiation Effect on C_{60} and Si Crystals

H. Naramoto, V. Lavrentiev, K. Narumi and S. Sakai
Advanced Science Research Center, JAERI

1. Introduction

C_{60} and transition metal atoms are supposed to be chemically interesting partners for the spontaneous structure formation study because both play a complementary role in the charge transfer process. The recent effort has shown that the evolved structures are endowed with characteristic electrical properties [1-4]. The structures include the carbon allotrope conversion through the chemical process. The directional energy beams such as ions are useful means to design the structures suitable for the application conditions.

In the present report, is described the radiation-effect-study of low energy C_{60} ions on typical two targets, C_{60} and Si. The ion irradiation is a violent technique beyond the binding energy of the relevant system but the careful application has been shown to be useful[5-10]. The energy of C_{60} ions was chosen so as to include the critical one for the break-up of C_{60} cages.

2. Experimentals

FCC C_{60} thin films were prepared on α-Al_2O_3 around 70-120 °C by using a Knudsen cell. The source material for C_{60} is high quality with 99.99 % purity. For the present study the bombardments of C_{60} ions were carried out under the conditions of 10-400keV and 10-100nA/cm^2. Different from the standard ion irradiation experiment, the negative potential for the secondary electron suppression was not applied for the proper evaluation of ion current under the strong influence of desorbing particles. The irradiated surfaces of C_{60} films were analyzed with micro-Raman spectrometry, AFM and step-profiling with a Dectak machine. The step height changes were evaluated referring to the pristine region in the same sample. The lattice disorder and possible carbon contaminations localized on Si surface were analyzed by employing techniques of RBS/channeling and RBS/nuclear reactions.

3. Results and discussion

In the course of irradiation the special cares were taken for the ion current integration because the desorbing procedure of adsobates becomes dominant by the high momentum transfer by incident C_{60} ions. Actually, the incident ion current has increased apparently after the incubation period where the release of adsorbed molecules is operative. In this course of study it was found that the step height evaluation is more sensitive way to detect the subtle change of C_{60} surface combined with Raman analysis.

Fig. 1 illustrates the intensity change of $A_g(2)$ Raman peak for C_{60} film as a function of the C_{60}^+ ion fluence, together with the spectral features. One can recognize that the C_{60}^+ ion irradiation induces two different processes separated around the dose of 2×10^{15}/cm^2. At the 1st stage($<2\times10^{15}$/cm^2) the intensity increases simply keeping the spectral features that suggests the improvement of the crystal quality through the easy-ejection of light impurity atoms. In the high fluence region ($>2\times10^{15}$/cm^2), the decrease of $A_g(2)$ peak intensity includes the spectral modification.

Through the careful analysis, it has been concluded that the broadening with the peak intensity decrease is associated with the appearance of polymeric component close to the original $A_g(2)$ peak position.

The lattice disorder induced by C_{60}^+ ion irradiation was studied on Si(100). The incident energies of C_{60} ions were changed in the range of 10 – 400keV. The induced lattice disorder seems to be localized in the near-surface-region(<10nm), and the induced disorder was evaluated as the broadening and/or the intensity increase of surface peak under the glancing emitting condition where the scattering angle was set at 105°. The surface peak intensity does not reach the random level probably because of relatively poor depth resolution of our detecting system with a surface barrier detector. The induced disorder increases linearly up to 1×10^{13} /cm^2, and then becomes saturated after 2.5×10^{13} /cm^2 for 10keV C_{60}^+ ions. The accumulated disorder is fairly small compared with the random level in RBS/channeling analysis but the preliminary study of optical reflectance spectroscopy suggests the existence of severe disorder in the near surface region. For further progress of this study, it is inevitable to compare the optical absorption features with the electrical characterization.

The analysis of contaminated carbon atoms on Si surface is also another important item in order to know the maximum energy where C_{60} ions can keep their cage structure even after collisions. The collision process of a whole C_{60} ion with solid may induce the cooperative effect different from the classical binary collision regime.

Fig. 2 suggests that 10keV C_{60} ions do not induce the build-up of carbon contamination in the broad range of C_{60} ion fluence different from the case for 400keV C_{60} ions, however, this result may include the competitive process between sputtering and carbon atom deposition through the C_{60} cage breakage. Further study is scheduled to show the direct evidence of rebound process of C_{60}.

References

1) V. I. Lavrentiev, H. Abe, S. Yamamoto, H. Naramoto and K. Narumi, Physica B: Con. Matter 323 (2002) 303-305.
2) V. Lavrentiev, H. Abe, S. Yamamoto, H. Naramoto, K. Narumi, Materials Letters 57 (2003) 4093-4097.
3) S. Sakai, H. Naramoto, Y. Xu, T. H. Priyanto, V. Lavrentiev, K.Narumi, MRS Symp. Proc. Vol. 788, L11.49.1(2004).
4) V. Lavrentiev, H. Naramoto, H. Abe, S. Yamamoto, K. Narumi and S. Sakai, Fullerene, Nanotubes and Carbon Nanostructures 12 (2004) 519-528.
5) H. Naramoto, X. D. Zhu, J. Vacik, Y. H. Xu, K. Narumi, S. Yamamoto and K. Miyashita, Phys. of Solid State 44 (2002) 668-673.
6) X. D. Zhu, Y. H. Xu, H. Naramoto, K. Narumi, K. Miyashita, J. Phys. :Con. Matter 14 (2002) 5083.
7) X. D. Zhu, H. Naramoto, Y. H. Xu, K. Narumi, K. Miyashita, J. Chem. Phys. 116 (2002) 10458-10461.
8) X. D. Zhu, H. Naramoto, Y. H. Xu, K. Narumi, K. Miyashita, Phys. Rev. B 66 (2002) 165426.
9) X. D. Zhu, X. H. Wen, R. J. Zhan, H. Naramoto, F. Arefi-Khonsart, J. Phys.: Condensed Matter 16 (2004) 1175-1181.
10) X. D. Zhu, K. Narumi, Y. Xu, H. Naramoto, F. Arefi-Khonsari, J. Appl. Phys. 95 (2004) 4105-4110.

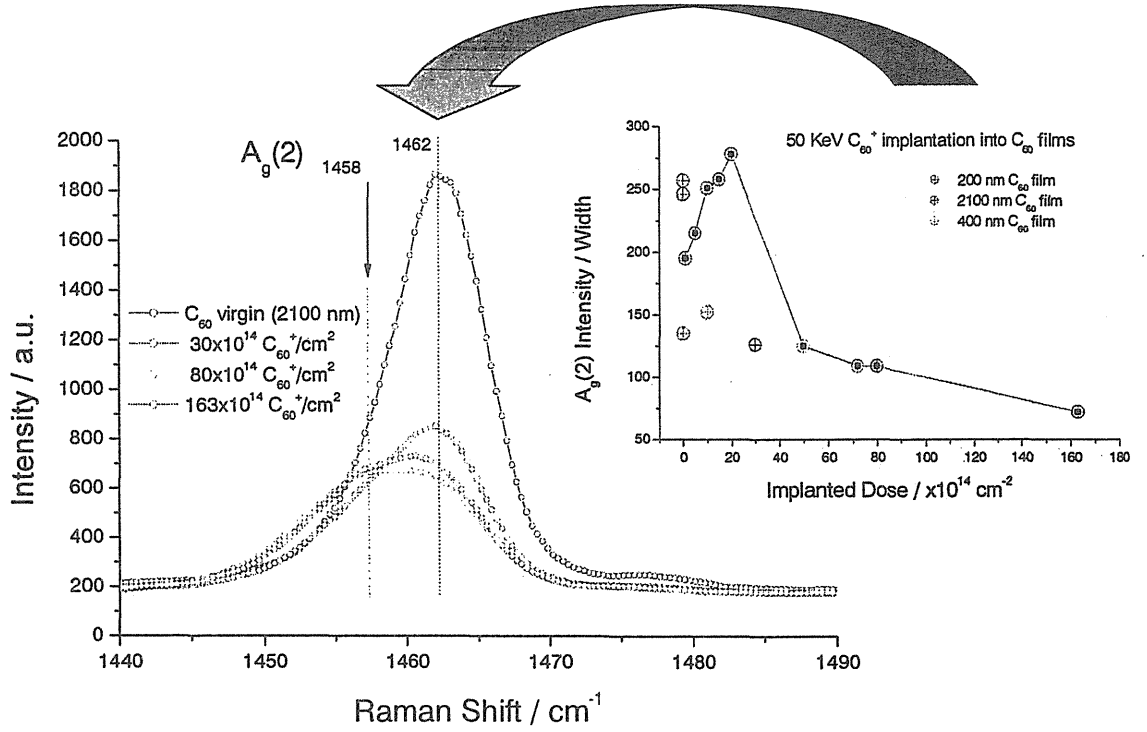

Fig. 1: Typical changes in Raman spectra at the 2nd stage as a function of 50keV C_{60}^{+} ion fluence for three different samples. The increase of Ag(2) peak intensity in the low fluence region ($<2\times10^{15}/cm^2$) corresponds to the recrystallization associated with impurity atom ejection. On the contrary, the decrease of $A_g(2)$ peak intensity in the high fluence region indicates the appearance of additional component reflecting the polymerization cooperated with the sputtering.

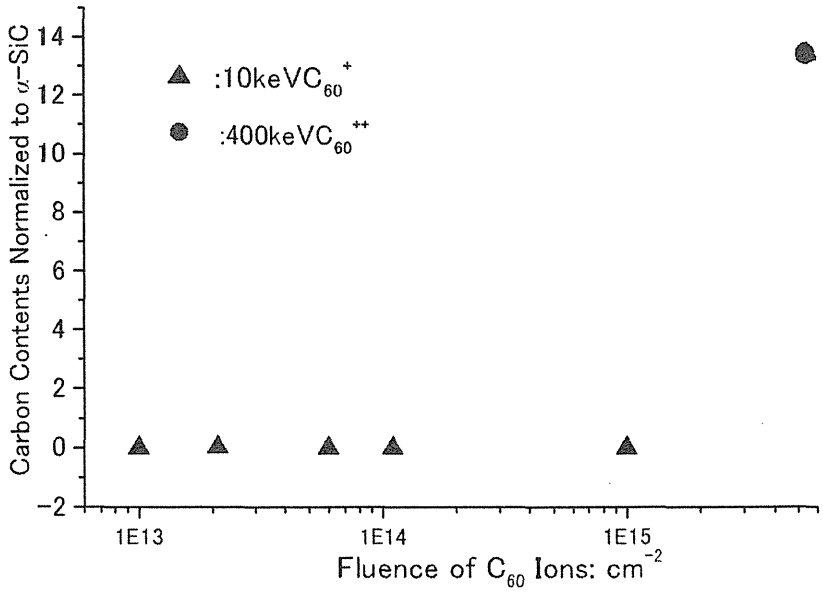

Fig. 2: Content change of carbon atoms on Si surface as a function of C_{60} ion fluence. Carbon atoms were analyzed by $^{12}C(d, p)^{13}C$ nuclear reactions. The contents were normalized to that for α-SiC crystal.

5.4 Observation of a Nano-sized-pinhole Array in Ni Thin Films on MgO(100) Substrates

K. Narumi, C. Lin and H. Naramoto
Advanced Science Research Center, JAERI

1. Introduction

It is well known that the physical properties bear tight relationships with the surface morphology of thin films, and thus patterning the surface on the nanometer scale is of importance to obtain unique properties for potential application; Numerous nanostructures have been prepared: for example, the zero-dimensional quantum dots with interesting electronic and optoelectronic properties and one-dimensional magnetic nanowires. Recently the formation of three-dimensionally structured films has also attracted a great deal of attention. One of such structures is a surface with pinholes. It was found that pinholes on the nanometer scale had a significant effect on the magnetic properties of a Ni film on an anodic aluminum oxide substrate[1] and an annealed Co film[2].

In the present study, pinholes with narrow size distribution and spatial distribution were observed in Ni thin films deposited on MgO(100) substrates. We will discuss the origin of such structure formation in terms of the elastic strain energy.

2. Experimental

Ni films were prepared by using an e-gun evaporation system. Polished MgO(100) single crystals were used as substrates. The base pressure of the deposition chamber was 1×10^{-6} Pa. During deposition, the chamber was cooled by liquid nitrogen and the pressure was lower than 3×10^{-6} Pa. Deposition rate, which was monitored by a standard quartz microbalance system, was less than 0.01 nm/s. The deposition was performed for a substrate kept at 400°C or room temperature (RT). After deposition, the sample was taken out when its temperature arrived at RT. The morphology of the film was immediately investigated by an atomic force microscope (JEOL JSPM 4200) at AC mode in the air. The MikroMasch Si tips were used, which are characterized by radius of curvature less than 10 nm and full tip cone angle less than 20°.

3. Results and discussion

Figure 1 shows examples of AFM images and corresponding height profiles of films with thickness of 1, 10 and 30 nm deposited at RT. As shown in Fig. 1(a) and 1(b), small round Ni grains and some pinholes whose diameter was ~5–10 nm were observed for films with nominal thickness of 1, 2.5, 5, 7.5, 10 and 15 nm deposited at RT. It was also observed, as clear in Fig. 1(b), that the pinholes demonstrated a uniform size distribution and even showed a nearly uniform spatial distribution, which resulted in the formation of a pinhole array. For films with thickness of 20 and 30 nm, it was difficult to find pinholes; a lot of big Ni islands composed of 3–4 grains were observed on the surface as shown in Fig. 1(c).

The formation of pinholes was also observed for 2.5–7.5-nm Ni films deposited at 400°C; Fig. 2(b) shows an example of AFM images of a 7.5-nm Ni film. From the corresponding height profile Fig. 2(e), the mean diameter of the pinhole and the grain is deduced to be 50 nm. On the other hand, for a 1-nm film, only grains whose diameter was approximately 25 nm were observed as shown in Fig. 2(a). For a 10-nm film, the uniformly sized pinholes begin to disappear

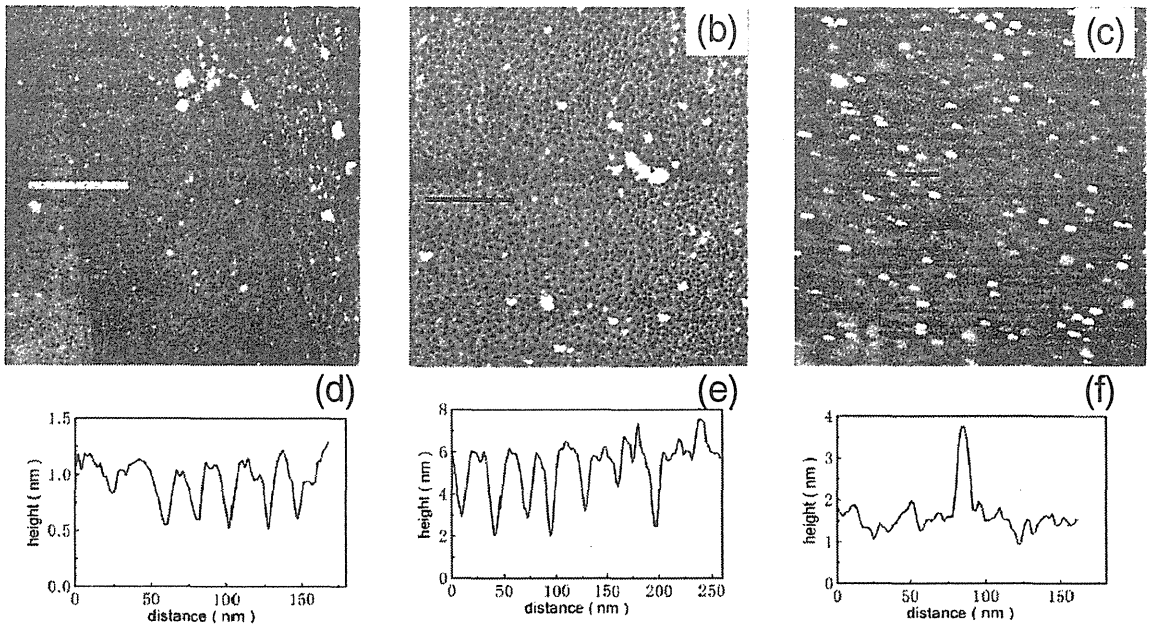

Fig. 1. AFM images of (a) 1-nm, (b) 10-nm and (c) 30-nm Ni films deposited onto MgO(100) at RT; Image size is 1×1 . m^2. The corresponding height profiles (d), (e) and (f) were taken along the horizontal white and black lines shown in (a), (b) and (c), respectively.

as shown in Fig. 2(c).

The formation mechanism of round Ni grains is easy to be understood. It is well known that growth mode for a thin film is governed thermodynamically by the surface energy of both a substrate and a film and the interfacial energy between the film and the substrate[3]. For the Ni/MgO(100) system, the surface energy of Ni and MgO is approximately 2.3 and 1 J/m^2, respectively[4]. The large difference in surface energy induces a Ni film to follow the three-dimensional island growth mode on MgO(100) generally, which results in the formation of small round grains at the initial stage of the growth. The reason why the grains in the films deposited at 400°C are much larger than those in the films deposited at RT is that both the nucleation rate and size of critical nucleus increase with the increasing substrate temperature.

According to the observation in a Cu/Co system by Schmid et al.[5], the pinholes are mainly formed in the vicinity of defects on a substrate surface, such as pits, steps and contaminants. The pinholes are formed even at the thickness of approximately 1 monolayer. The density of those pinholes is of the order of a few thousands per . m^2 at the thickness of 2 monolayers and decrease quickly with the increasing thickness of the film, because sequential arriving atoms fill the pinholes. In their case, the pinholes are normally formed in an irregular shape and with wide distribution in size. In the present case, on the other hand, the diameter of the pinholes is nearly the same, and in the same magnitude of Ni island size. Thus the main reason for the formation of uniformly sized pinholes cannot be attributed to the defects of the substrate.

It is well known that the driving force for the formation of periodic or uniform structure in a thin film can be attributed mainly to long-range elastic interaction, which is generated because of the discontinuity of the intrinsic surface stress tensor on periodic structure boundary and by the lattice mismatch between the components[6]. The ordered arrangement of islands can also be interpreted as follows: there would be a minimum in the free energy when the pinholes

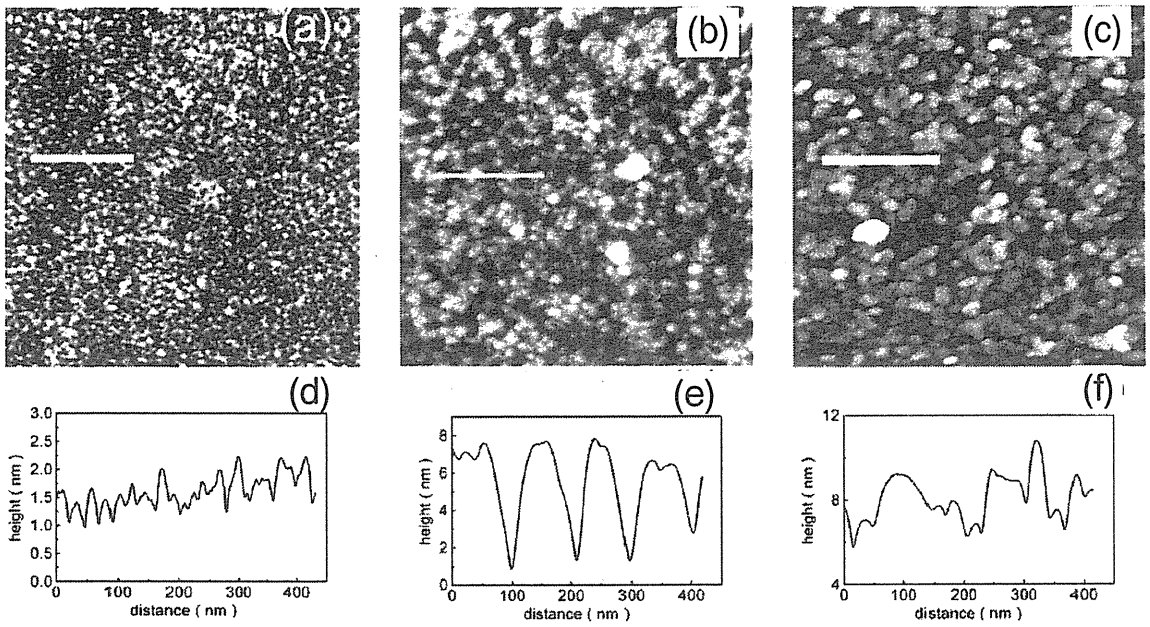

Fig. 2. AFM images of (a) 1-nm, (b) 7.5-nm and (c) 10-nm Ni films deposited onto MgO(100) at 400°C; Image size is 1×1 . m^2. The corresponding height profiles (d), (e) and (f) were taken along the horizontal white lines shown in (a), (b) and (c), respectively.

not only stabilize the uniform size distribution but also exhibit a spatial distribution by interacting each other via substrate[7]. One may notice that the distribution of the pinhole is not perfectly uniform across the film surface. This can be attributed to the irregularity of the substrate surface. Although a polished surface of an MgO single crystal was used in the present study, some defects still remain. The defects with the strain energy propagate unevenly and result in the slight perturbation to pinhole distribution.

The density of the pinholes decreases with the increasing thickness; finally no pinholes are observed for thicker films. This can be ascribed to the filling of the pinholes by atoms deposited later or to the coverage by the sequential upper islands.

In conclusion, a thin Ni film on an MgO(100) substrate shows pinhole structure on the surface in a certain thickness range under the effect of elastic strain. The pinholes have a uniform size distribution and form an array in a film at a certain thickness.

References

1) Z.L. Xiao, C.Y. Han, U. Welp, H.H. Wang, V.K. Vlasko-Vlasov, W.K. Kwok, D.J. Miller, J.M. Hiller, R.E. Cook, G.A. Willing and G.W. Crabtree, Appl. Phys. Lett. **81** (2002) 2869.
2) H. Shi and D. Lederman, J. Appl. Phys. **87** (2000) 6095.
3) K. Reichelt, Vacuum **38** (1988) 1083.
4) E.S. Machlin, An Introduction to Aspects of Thermodynamics and Kinetics Relevant to Materials Science, GIRO Press, New York, 1991, p. 117.
5) A.K. Schmid, D. Atlan, H. Itoh, B. Heinrich, T. Ichinokawa, J. Kirschner, Phys. Rev. B **48** (1993) 2855.
6) G.L. Zhou, M.H. Yang and C.P. Flynn, Phys. Rev. Lett. **77** (1996) 4580.
7) V.A. Shchukin and D. Bimberg, Rev. Modern. Phys. **71** (1999) 1125.

5.5 Effects of Cluster Ion Irradiation in Oxide Superconductors

A. Iwase[*], N. Ishikawa[**], Y. Chimi[**], T. Hashimoto[***],
O. Michikami[***], Y. Saito[****] and A. Chiba[****]
Osaka Prefecture University[*]
Department of Materials Science, JAERI[**]
Faculty of Engineering, Iwate University[***]
Advanced Radiation Technology Center, JAERI[****]

1.Introduction

According to the previous studies[1-3], the stopping power for cluster ion increases almost linearly as increasing the number of constituent atoms. However, the atomic displacements due to cluster ion irradiation are not straight forward.

According to the analogy of monoatomic ion irradiation to inorganic solid materials, the density of defects created via the electronic energy deposition generally increases superlinearly as a function of the electronic stopping power, while the density of defects created via elastic displacements increases linearly as increasing the nuclear stopping power.

As far as the oxide superconductors are concerned, if the electronic stopping power is sufficiently high, the defect creation due to electronic energy deposition is dominant compared with that due to elastic displacements. For example, for oxide superconductors irradiated with 30MeV C_{60} cluster ions, tracks with very large diameter are created along beam paths, reflecting that the defect creation via electronic energy deposition is dominant[4,5], although 0.5MeV C having same velocity never create tracks. Cluster ion irradiation is one of the useful ways to study the nonlinear effect observed for defect creation due to electronic energy deposition. At present, the threshold number of carbons for the defect creation via electronic energy deposition is still unknown. In this study, 0.5MeV C and 4MeV C_8, both having the same velocity, are irradiated to oxide superconductors, and we tried to estimate the effects of elastic displacements and those of electronic energy deposition for 4MeV C_8 irradiation.

2. Experimental Procedure

Thin films of c-axis oriented $EuBa_2Cu_3O_y$ (y=7) were prepared on MgO substrates by a sputtering method. 0.5MeV C and 4MeV C_8 ions are irradiated at room temperature using the 2MV VdG accelerator at JAERI-Tokai and the tandem accelerator at JAERI-Takasaki, respectively. The projected range of those ions is about 0.6μm, but for the molecules (C_8 ions) they become dissociated and have no more spatial correlation as the molecules proceed deeper into the sample. Therefore, the sample thickness was determined to be 0.1μm, which is enough to assure the spatial correlation of molecules during their passage through the sample. The fluence dependence of c-axis lattice parameter was examined by measuring X-ray diffraction pattern.

3.Results and Discussion

Figure 1 shows the fluence dependence of

$\Delta c/c_o$ for the irradiation with 4MeV C_8, where Δc represents the increase in c-axis lattice parameter due irradiation, and c_o the c-axis lattice parameter before irradiation.

The lattice expansion is observed also for 0.5MeV C irradiation, and it is already known to be due to the elastic displacements[6]. If the effects are compared with the unit fluence of carbons/cm^2, the lattice expansion for 4MeV C_8 almost coincide with that for 0.5MeV C. This means that within the error the lattice expansion for 4MeV C_8 is due to the elastic displacements.

According to the systematic study of lattice expansion due to monoatomic ion irradiation, the contribution of elastic displacements and that of electronic energy deposition can be separated[6]. Concerning the effects of cluster ion irradiation, it is debatable that the result for monoatomic ion irradiation is applicable to cluster ion irradiation.

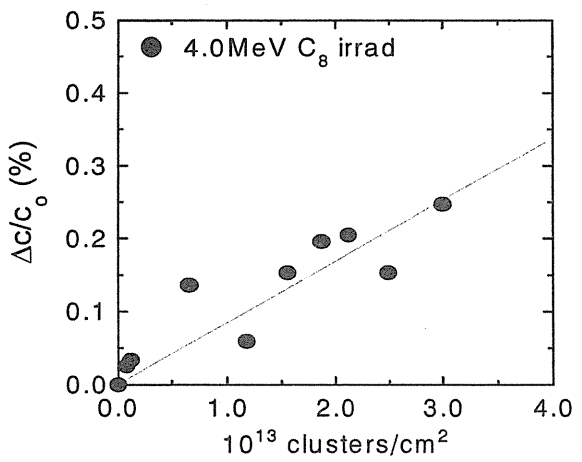

Fig.1 Fluence dependence of c-axis lattice parameter in $EuBa_2Cu_3O_y$ irradiated with 4MeV C_8.

But, if it is assumed to be applicable for 4MeV C_8, then it is expected that its contribution of the electronic energy deposition to lattice expansion is comparable to that of elastic displacements. However, in this study, it is found that the contribution of electronic energy deposition is negligible compared to that of elastic displacements. In other words, the threshold number of carbon constituents for defect creation via electronic energy deposition is expected to be more that n=8.

References

1) K. Baudin, A. Brunelle, M. Chabot, S. Della-Negra, J. Depauw, D. Gardes, P. Hakansson, Y. Le Beyec, A. Billebaud, M. Fallavier, J. Remillieux, J.C. Poizat, J.P. Thomas, Nucl. Instr. and Meth. B 94 (1994) 341.

2) D. Ben-Hamu, A. Baer, H. Feldman, J. Levin, O. Heber, Z. Amitay, Z. Vager, D. Zajfman, Phys. Rev. A 56 (1997) 4786.

3) C. Tomaschko, D. Brandl, R. Krüger, M. Schurr, H. Voit, Nucl. Instr. and Meth. B 103 (1995) 407.

4) J. Jensen, A. Dunlop, S. Della-Negra, M. Toulemonde, Nucl. Instr. and Meth. B 146 (1998) 412.

5) A. Dunlop, G. Jaskierowicz, J. Jensen and S. Della-Negra, Nucl. Instr. and Meth. B 132 (1997) 93.

6) N. Ishikawa, A. Iwase, Y. Chimi, O. Michikami, H. Wakana, T. Hashimoto, T. Kambara, C. Müller, R. Neumann, Nucl. Instr. and Meth. B 193 (2002) 278.

5.6 Simulation of High Energy X-ray Irradiation by Electron Irradiation

N. Ishikawa*, A. Iwase**, Y. Chimi*, T. Hashimoto*** and O. Michikami***
Department of Materials Science, JAERI*
Department of Metallurgy and Materials Science, Osaka Prefecture University**
Faculty of Engineering, Iwate University***

1.Introduction

From the previous studies of electron irradiation effects, increase in electrical resistivity due to high energy (~MeV) electron irradiation is observed for $EuBa_2Cu_3O_y$ (y=6-7)[1], and the increase in electrical resistivity for $EuBa_2Cu_3O_y$ (y=6) is 4 orders of magnitude larger than that for $EuBa_2Cu_3O_y$ (y=7). In this sense, the oxygen-deficient $EuBa_2Cu_3O_y$ (y=6) is appropriate target material to precisely detect small defect concentration. Based on this recognition, using $EuBa_2Cu_3O_y$ (y=6) we have found for the first time that in this oxide material small increase in electrical resistivity reflecting defect creation is observed during irradiation of high energy (9keV) X-ray.

The mechanism of this X-ray induced atomic displacements is still unknown. One of the models to explain this phenomenon is that displacements take place as a result of high energy electrons caused by ionization process during X-ray irradiation. In order to test this model, we have simulated X-ray irradiation by irradiating high energy electrons directly to $EuBa_2Cu_3O_y$ (y=6) target and at the same time electrical resistivity is measured in situ.

2. Experimental procedure

Thin films of c-axis oriented $EuBa_2Cu_3O_y$ (y=7) were prepared on MgO substrates by a dc sputtering method. The thickness of films was about 300 nm. The samples with oxygen content of $y \approx 6$ were prepared by thermal annealing. The annealed samples are estimated to have oxygen content of $y \approx 6$, since their c-axis lattice parameter was larger by 1.2% than that of the sample having oxygen content of $y \approx 7$[2]. The specimens were irradiated at 100K with 9keV X-ray. The X-ray irradiation was performed at Photon Factory of the High Energy Accelerator Research Organization (KEK, Tsukuba). In order to avoid the possible irradiation effect of the electrode, only the specimen part was irradiated. In-situ measurement of change in electrical resistivity during irradiation was performed also at 100K.

In order to simulate the X-ray irradiation, we performed also the irradiation with 0.46MeV electrons from a 3MV single-ended accelerator in TIARA, JAERI-Takasaki. The irradiation temperature and measurement temperature were same as those adopted for the X-ray irradiation experiment. The energy of 0.46MeV was chosen because this is the lowest energy achievable by the accelerator.

3.Results and discussion

In $EuBa_2Cu_3O_y$ (y=6) irradiated with 0.46MeV electrons, increase in resitivity, $\Delta\rho/\rho_o$,

of 1% is observed when electron fluence reachs 4.4×10^{13} e/cm^2, where $\Delta\rho$ is the increase in electrical resistivity due to irradiation and ρ_o the electrical resistivity before irradiation. The fluence necessary for 1% increase in electrical resistivity corresponds to 1×10^{-3}ppm from the estimation using the differential scattering cross section proposed by MacKinley and Feshbach[3]. On the other hand, 1% increase in resitivity, $\Delta\rho/\rho_o$, due to 9keV X-ray irradiation is found to be caused by absorption of photons up to 1.5×10^{13} photons/cm^2. If we make a simple assumption that 1 photon causes one ionization thus creates 1 electron, then 1.5×10^{13} photons/cm^2 corresponds to 1.5×10^{13} electrons/cm^2, which is of same order of magnitude as the electron fluence (4.4×10^{13} e/cm^2) necessary to attain 1% increase in electrical resistivity, although there is still difference in actual value.

It is concluded that the posibility of elecron causing atomic displacements as a result of X-ray irradiation still survive after semiquantitative analysis of X-ray irradiation effects and elecron irradiation effects.

References

1) N. ishikawa, Y. Chimi, A. Iwase, K. Tsuru and O. Michikami, J. Nucl. Mater. 258-263 (1998) 1924.

2) W. R. McKinnon, M. L. Post, L. S. Selwyn, G. Pleizier, J. M. Tarascon, P. Barboux, L. H. Greene, and G. W. Hull, Phys. Rev. B 38 (1988) 6543.

3) W.A. MacKinley, H. Feshbach, Phys. Rev. 74 (1948) 1759.

5.7 High-energy Particle Irradiation Effects in Bi Thin Films

Y. Chimi*, N. Ishikawa* and A. Iwase**
Department of Materials Science, JAERI*
Research Institute for Advanced Science and Technology, Osaka Prefecture University**

1. Introduction

We have studied high-density electronic excitation effects caused by energetic heavy ion irradiation in conductive materials. It makes it clear that atomic displacements can occur due to electronic excitation even in metals, in which a large number of conduction electrons have been considered to screen the electronic excitation effects. Therefore, semiconductors or semimetals, which have much lower carrier density than metals, have been expected to show stronger electronic excitation effects. Based on this concept, we have performed high-energy heavy ion irradiation in Bi thin films, and found a sign of irradiation-induced amorphization as the resistivity change due to re-crystallization of amorphous regions[1]. It is noted here that amorphous Bi thin films show a superconducting transition below ~6.2 K[2], and therefore, the amorphization attributed to electronic excitation may realize a one-dimensional superconducting state. In order to clarify whether the present amorphization is attributed to electronic excitation or not, we have investigated high-energy particle irradiation effects in Bi thin films. In the present report, we show an experimental result for energetic electron irradiation as a reference for irradiation effects.

2. Experimental Procedure

A polycrystalline Bi thin film (370 Å thick) was deposited on an α-Al_2O_3 single crystal substrate by vacuum evaporation at room temperature in a vacuum below ~3×10^{-8} Torr with a mask for a four-probe electrical resistivity measurement. Since the crystallization temperature of amorphous Bi thin films depends on the film thickness, the thickness of the present specimen was chosen so as not to induce crystallization at the irradiation temperature. The specimen was irradiated below ~17 K with 2.0-MeV electrons from a 3-MV single-ended accelerator in TIARA, JAERI-Takasaki. The change in electrical resistivity of the specimen was measured *in situ* at ~12 K as a function of electron fluence.

3. Results and Discussion

Figure 1 shows the change in electrical resistivity of the specimen, $\Delta\rho$, as a function of electron fluence, Φ. In the case of semi-metallic Bi, not only the change in carrier mobility but also that in carrier density contributes to $\Delta\rho$ due to accumulation of the irradiation-produced defects. Therefore, $\Delta\rho$ is not always proportional to the concentration of irradiation-produced defects. As compared with the results for similar experiments on bulk Bi specimens[3], the resistivity change rate for thin film specimen is about four-orders of magnitude higher than that for bulk specimen. Such a high resistivity change rate may be ascribed to a high defect production rate for thin film specimen. It seems to be qualitatively reasonable, because amorphous state in Bi can be realized only for thin film specimen, so that defects may exist more stable in thin film specimen than in bulk specimen.

Moreover, as compared with the results for

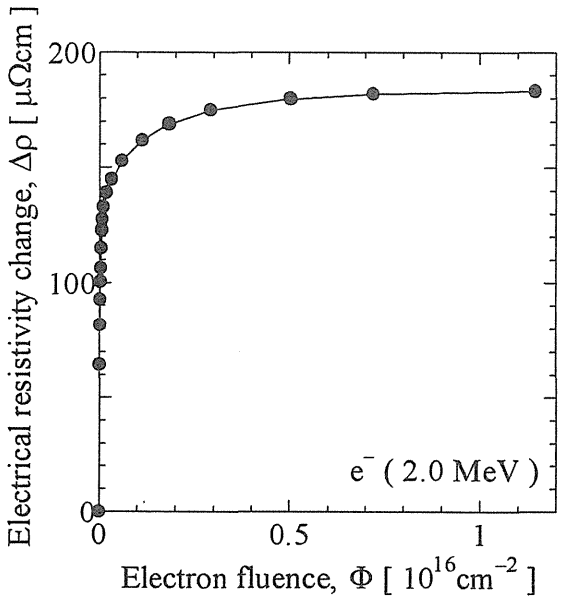

Fig. 1. Change in electrical resistivity of specimen, Δρ, as a function of electron fluence, Φ.

ion irradiations[1], saturation resistivity for high-energy heavy ion irradiation appears to be larger than that for electron irradiation. This means that high degree of disorder is induced by high-energy heavy ion irradiation, implying the amorphization due to electronic excitation.

References

1) Y. Chimi, N. Ishikawa, A. Iwase, Mat. Res. Soc. Symp. Proc. 792 (2004) 379.
2) W. Buckel, R. Hilsch, Z. Phys. 138 (1954) 109.
3) F. Beuneu, P. Bois, Phys. Rev. B 37 (1988) 6041.

5.8 Interaction between Irradiation-produced Defects and Solute Cu Atoms in Fe-Cu Model Alloys for Pressure Vessel Steels of Light Water Reactors

Y. Chimi[*], T. Tobita[**], N. Ishikawa[*], M. Suzuki[**], A. Iwase[***] and S. Ishino[****]
Department of Materials Science, JAERI[*]
Department of Reactor Safety Research, JAERI[**]
Research Institute for Advanced Science and Technology, Osaka Prefecture University[***]
Department of Applied Science, Tokai University; Central Research Institute of Electric Power Industry[****]

1. Introduction

Fe-Cu alloys are well-known as model alloys for studying a mechanism of irradiation embrittlement in pressure vessel steels of light water reactors. One of the major reasons of the irradiation embrittlement is a radiation-enhanced segregation of solute Cu atoms. The radiation-enhanced segregation can be caused by neutron irradiation and energetic electron irradiation via Compton scattering of γ-rays in the pressure vessel steels. To study the mechanism of radiation-enhanced segregation of Cu atoms in Fe-Cu alloys, we have performed electron irradiation in Fe-Cu alloys at room temperature, and observed the electrical resistivity change as a function of electron fluence[1]. Except for an early stage of irradiation, the electrical resistivity shows a monotonic decrease with increasing fluence, which can be ascribed to the clustering and/or precipitation of Cu atoms. The decreasing rate strongly depends on the Cu concentration of Fe-Cu alloys, and the quantitative evaluation gives a conclusion that more than one Cu atom are removed from solid solution by one irradiation-produced Frenkel pair. Since such a high clustering efficiency cannot be explained by the ordinary vacancy mechanism, the contribution of interstitial atoms to the processes of radiation-enhanced segregation should be considered. In the present work, in order to study the interaction between irradiation- produced interstitial atoms and solute Cu atoms, we have performed electron irradiation of Fe-Cu alloys with several Cu concentrations at low temperature, and observed the dependence of the thermal recovery of defects on Cu concentration.

2. Experimental procedure

Four kinds of Fe-Cu alloys with different Cu concentration (0.02, 0.1, 0.6 and 1.2 wt.%) were used as specimens. The chemical composition of the specimens is shown in Table 1. The specimens were solution-annealed at 1123 K for 10 min under a vacuum, and then quenched into helium gas. This process made Cu atoms dissolve supersaturatedly in the iron lattice. The size of the specimen was 1 mm × 10 mm × 30

Table 1. Chemical composition of specimens in wt.%.

Specimen	Cu	C	Si	O	N	Fe
Fe-0.02wt.%Cu	0.022	0.003	0.003	0.015	0.0006	Balance
Fe-0.1wt.%Cu	0.1	0.002	0.003	0.014	0.0005	Balance
Fe-0.6wt.%Cu	0.61	0.002	0.002	0.015	0.0006	Balance
Fe-1.2wt.%Cu	1.19	0.002	0.001	0.013	0.0006	Balance

μm. Fe-Cu alloy ribbons, which had the same Cu concentration as the specimens, were spot-welded to the specimens as lead wires for electrical resistivity measurement. The specimens were mounted on aluminum substrates by using epoxy resin (Araldite) in order to insulate the specimens from the substrates. The specimens were irradiated below 20 K with 2.0-MeV electrons from a 3-MV single-ended accelerator in TIARA, JAERI-Takasaki. The change in electrical resistivity of each specimen, $\Delta\rho$, was measured *in situ* at 12 K during irradiation as a function of electron fluence. After irradiation, the thermal recovery of $\Delta\rho$ was observed by means of isochronal annealing.

3. Results and discussion

Figure 1 shows the change in electrical resistivity of the specimens as a function of electron fluence. For each specimen, $\Delta\rho$ increases linearly with fluence, but the increasing rate depends on the Cu concentration. This result indicates that the defect production cross-section, σ_d, and/or the Frenkel pair resistivity, ρ_F, become larger for higher Cu concentration. From electron energy dependence of the resistivity increasing rate, we can estimate the displacement threshold energy, E_d, and then σ_d for Fe-Cu alloys with different Cu concentration. The estimated value of σ_d for Fe-0.6wt.%Cu is a little larger than that for Fe-0.02wt.%Cu, which is not enough to explain the difference in the resistivity increasing rate. Therefore, the difference comes mainly from the difference in ρ_F.

Isochronal recovery behavior of $\Delta\rho$ is shown in Fig. 2. The value of $\Delta\rho$ normalized by $\Delta\rho$ before annealing, $\Delta\rho_0$, means the fraction of defects surviving at the annealing temperature. Several peaks in the recovery behavior correspond to the defect recovery stages from I_A to I_E for pure Fe[2)], in which Frenkel pairs recombine through the migration of interstitial atoms. For the stages I_A-I_D, which is related to the correlated recovery of Frenkel pairs, the peaks decrease with increasing Cu concentration, but the peak temperatures do not seem to shift. These results suggest that an interstitial atom is trapped by a neighboring Cu atom, or that there is high possibility of clustering among

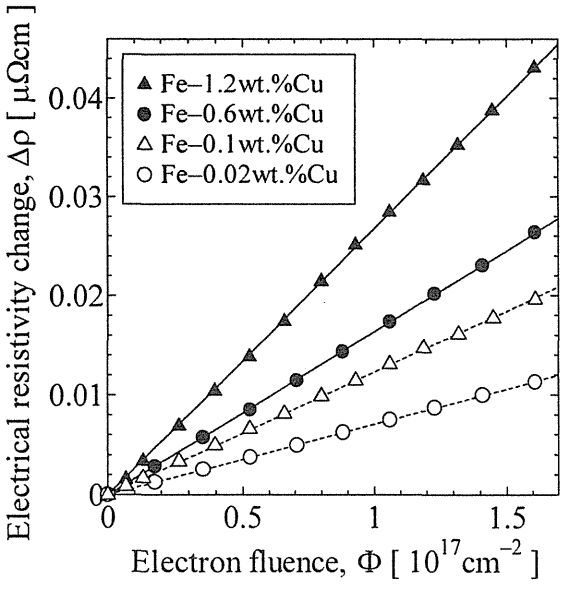

Fig. 1. Change in electrical resistivity of specimens as a function of electron fluence.

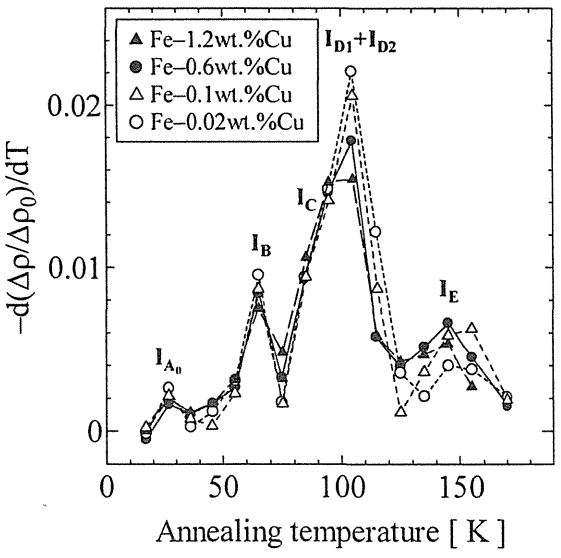

Fig. 2. Isochronal recovery behavior of $\Delta\rho$. $\Delta\rho_0$ represents $\Delta\rho$ before annealing.

interstitial atoms due to increasing defect concentration. On the other hand, for the stage I_E, which is related to the uncorrelated recovery of Frenkel pairs, the peak tends to increase and shift to lower temperature with increasing Cu concentration. It implies that an interstitial atom trapped by a Cu atom is dissociated from the Cu atom and recombine with a vacancy, or that an interstitial atom encounters easier with a vacancy for higher defect concentration.

From the results for the present work, we can conclude that solute Cu atoms contribute to stabilization of interstitial atoms, and therefore, interstitial atoms may play an important role in the processes of radiation-enhanced segregation.

References

1) S. Ishino, Y. Chimi, Bagiyono, T. Tobita, N. Ishikawa, M. Suzuki, A. Iwase, J. Nucl. Mater. **323** (2003) 354.
2) S. Takaki, J. Fuss, H. Kugler, U. Dedek, H. Schultz, Radiat. Eff. **79** (1983) 87.

5.9 Anelasticity of Nanocrystalline FCC Metals after Low-temperature Irradiation

H. Tanimoto*, N. Yagi*, Y. Ishibashi*, A. Ueki*, T. Hinuma*,
H. Mizubayashi*, N. Ishikawa** and Y. Chimi**
Institute of Materials Science, University of Tsukuba *
Department of Materials Science, JAERI**

1. Introduction

Polycrystalline materials with an ultrafine crystallite size less than 100 nm have a unique structure in which the ultrafine crystallites are connected by grain boundaries (GBs), and are called as nanocrystalline (n-) materials. When the ultrafine particles are mechanically consolidated, the highly disordered GBs may be formed to accommodate the neighboring ultrafine crystallites. It is expected that the n-material possesses a novel property which is different from that of the (p-) crystalline and amorphous solids or the ultrafine particles.[1] We found that fully-dense FCC n-metals shows a quite large anelastic strain due to probable relaxation at GBs. Since GBs can act as a sink of point defects, n-metals are expected to show a decreased irradiation effect. In order to pursue these issues, we investigated the anelasticity of high-density n-Au and n-Cu after low-temperature irradiation.

2. Experimental procedure

High-density n-Au and n-Cu specimens were prepared by the gas-deposition (GD) method.[2] Ultra-fine metal particles formed by an inert gas condensation process in the evaporation chamber were sucked by a thin pipe and transferred to the deposition chamber, then directly deposited on a cooled glass substrate. The purity of the helium gas used as the atmosphere was kept as high as 99.9999 % in order to obtain contamination-free and fully-dense specimens. By controlling the position of the substrate, ribbon like specimens of about 20 mm long, 1 mm wide and 40 μm thick were prepared. The specimens were carefully removed from the glass substrate, where no bending and breaking of the specimens were found.

The resonant frequency (f, where $f^2 \sim E$; Young's modulus) and internal friction (Q^{-1}) measurements were performed by the flexural vibrating reed method at $f \sim 200$ Hz and the strain amplitude of $\sim 10^{-6}$.[2,3] The 2 MeV electron or 20 MeV proton irradiation below 40 K were carried out by using the single-end accelerator of JEARI, Takasaki, or the tandem accelerator of University of Tsukuba, respectively.

3. Results and conclusion

The mean grain size estimated from the broadening of X-ray diffraction peaks was 20 ~ 40 nm for n-Au and 10 ~ 30 nm for n-Cu, respectively. The density relative to that of the polycrystalline counterpart was >

99 % for n-Au and > 96 % for n-Cu.

For n-Au, as shown in Fig.1, a broad relaxation peak and small shoulders accompanied by modulus defects were observed at around 95 K ($Q^{-1}_{p,95K}$, hereafter), 20 K and 50 K in the Q^{-1} spectrum.[4] Above 200 K, Q^{-1} showed a rapid increase ($Q^{-1}_{>200K}$, hereafter) and f a large decrease. Both $Q^{-1}_{p,95K}$ (including their shoulders) and $Q^{-1}_{>200K}$ almost diminished after annealing where the grain growth was observed.[5,6] $Q^{-1}_{>200K}$ and the corresponding decrease in f were similarly observed for n-Cu. It is noted the Young's modulus of n-Au and n-Cu in the tensile tests at the stress above ~ 20 MPa showed a large decrease from that of the polycrystalline counterpart above 200 K and the amount of the decrease increased with temperature and stress.[5] These observations indicate that the large anelastic strain observed for the FCC n-metals is due to some relaxation process at the GBs. The activation enthalpy of the stress relaxation of n-Au is found to be 0.2 eV[3] which is much lower than the activation enthalpy of 0.88 eV reported for the GB diffusion in p-Au. The quite low activation enthalpy suggests that the process responsible for the large anelastic strain of FCC n-metals is due to cooperative motions of many atoms at the GBs.

After the low-temperature irradiation with the Frenkel-defect concentration (C_{FP}) up to ~ 200 ppm, $Q^{-1}_{>200K}$ of n-Au and n-Cu showed almost no change. For n-Au, $Q^{-1}_{p,95K}$ including their shoulders remained unchanged (Fig.1). In contrast, a large decrease in Q^{-1} and an increase in f (dislocation pinning phenomena) were simultaneously observed for p-Au after irradiation with C_{FP} < 1 ppm. These observations also support that $Q^{-1}_{>200K}$ and $Q^{-1}_{p,95K}$ are not due to dislocations but to some relaxation processes in the GBs.[3,5]

From Fig. 1, the anelasticity becomes negligible with decreasing the temperature below 200 K so that f at 6 K reflects the intrinsic modulus of the specimen. During the irradiation experiments, a monotonous increase in f at 6 K was observed with the

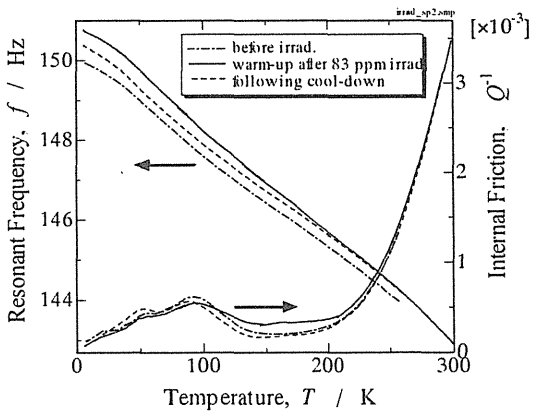

Figure 1 Temperature dependences of resonant frequency (f) and internal friction (Q^{-1}) observed for n-Au before and after 2MeV e⁻ irradiation below

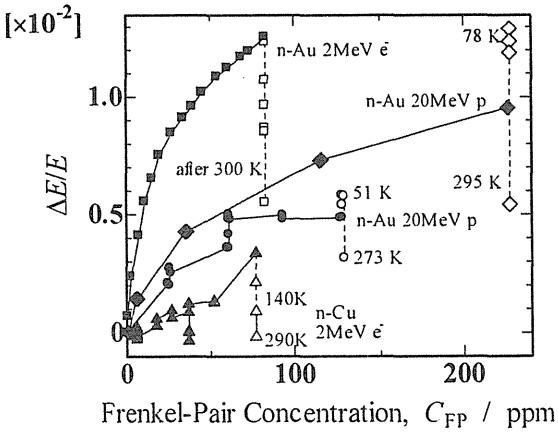

Figure 2. Relative change in the dynamic Young's modulus ($\Delta E/E_0$) observed for n-Au and n-Cu at 6K during low-temperature irradiation and after the following annealing. E_0 is E

accumulation of C_{FP}. Figure 2 shows a relative change in the Young's modulus observed at 6 K ($\Delta E/E_0$, E_0 ; the Young's modulus before irradiation) for the accumulated C_{FP}. We found that the single crystal refractory BCC metals showed a small decrease in the Young's modulus by irradiation, i.e. $(\Delta E/E_0)/(C_{FP}) \sim -10^7$, which is attributed to the paraelastic effect of irradiation-induced defects. Since the free migration temperature of self-interstitial atoms (SIAs) in Au and Cu is reported to be below 1.5 K and at around 40 K, respectively[8], the large increase in $\Delta E/E_0$ by irradiation suggests some modification of the GBs by SIAs trapped at GBs during irradiation. The increased $\Delta E/E_0$ by irradiation showed a recovery after annealing up to the stage III, indicating the recombination of the trapped SIAs with the vacancies.

We tentatively surmise that there exist at least two different types of relaxation process in the GBs of FCC n-metals. One is the process responsible for $Q^{-1}{}_{>200K}$ and hardly modified by the point defects. The other is for the large positive $(\Delta E/E_0)/(C_{FP})$ at 6 K and strongly modified by the point defects.

References

1) H. Gleiter, Prog. Mater. Sci., 33(1989)223-315.
2) S. Sakai, H. Tanimoto and H. Mizubayashi, Acta Mater., 47(1999), pp. 211-217.
3) S. Sakai, Thesis, University of Tsukuba, (2001).
4) H. Tanimoto, H. Mizubayashi, H. Fujita and S. Okuda, J. de Phys., 6(1996)C8-199-202.
5) H. Tanimoto, S. Sakai, and H. Mizubayashi, Mat. Sci. Eng. A, 370(2004) 135-141.
6) H. Tanimoto, S. Sakai, K. Otsuka, E. Kita and H. Mizubayashi, Mat. Sci. Eng. A, 370(2004)177-180.
7) H. Tanimoto, H. Mizubayashi and S. Okuda, Proc. Int. Conf. of Ultra High Purity Base Metals UHPM-94, (1995), 359～364.
8) P. Jung, "Landolt-Börnstein New Series Group III : Crystal and Solid State Physics Vol.25", ed. by Ullmaier H., (Springer-Verlag, Berlin, 1991)

5.10 Electron-paramagnetic-resonance Characterization of Phosphorus Doping to Silicon Carbide by Ion Implantation

T. Umeda*, M. Katagiri*, Y. Ishitsuka*, N. Mizuochi*, J. Isoya*,
T. Ohshima**, A. Ohi**, N. Morishita** and T. Kamiya**
Graduate School of Library, Information and Media Studies, University of Tsukuba*
Department of Material Development, JAERI**

1. Introduction

Silicon Carbide (SiC) is a promising wide-band-gap semiconductor for high-power, high-frequency, and low-energy-loss electronic devices, superior to the current Si- or GaAs-based devices. One major advantage of this material is a controllability of both *p* and *n*-doping by ion implantation. This makes it possible to create a variety of device structures by a selective area doping. To fabricate SiC devices, n^+-doping is crucially important for creating source/drain or contact regions. Among various *n*-type dopants, phosphorus (P) was recognized as the best dopant for n^+-doping[1]. It was demonstrated that optimized P-doped layers show the highest activation of dopants and the lowest sheet resistance[1]. However, the activation process and physical limits of P doping have not been well established yet. Generally, the dopant activation is strongly limited by point or extended defects that are also generated by ion implantation itself. Therefore, we tried to study directly the relationship between the defect formation/annihilation and the dopant activation by means of electron paramagnetic resonance (EPR). This method can reveal point defects and dopants, and thus provide us with a powerful characterization tool for the doping process.

Last year, we reported EPR characterization of P ion implantation to 6*H*-SiC crystals. We for the first time detected EPR signals of ion-implanted P donors[2]. This year, we carried out the same ion implantation to 4*H*-SiC which is more important for device applications because of its wider band gap (3.3 eV) than 6*H*-SiC (3.0 eV). This paper describes a microscopic characterization of the P doping to SiC by EPR. Also using EPR, we point out a novel application of P donors in SiC to the quantum computing[3].

2. Experimental

Starting wafers were 1.5-mm-thick 4*H*-SiC wafers of Nippon Steel Corporation (room-temperature carrier concentration = 1×10^{17} cm^{-3}). These wafers included N donors which were unintentionally incorporated in the crystal growth. P ions were implanted with a total dose of 4.5×10^{14} cm^{-2} at 9 ~ 21 MeV by TIARA tandem accelerator. This process was adjusted to produce a box-like profile (2-μm in depth) of P dopants with a concentration of 1×10^{18} cm^{-3}. Those implantations were carried out at room temperature, 400°C, and 800°C along either the [0001] or [11$\bar{2}$0] directions. After the implantation, the activation anneal of 1650°C (in Ar ambient) was subjected to the samples.

All EPR measurements were carried out by the standard X-band spectrometer (Bruker E500 model) at 40 ~ 60 K. The low-temperature measurements were necessary for observing shallow donors. Also we used pulsed EPR (Bruker E580 spectrometer) to directly measure time-resolved phenomena of donor electron spins, which will be described in Sec. 3.2.

3. Results and Discussion

3.1 P ion implantation to 4*H*-SiC

Figures 1(a) and (b) show EPR spectra of the P-implanted samples before and after 1650°C activation annealing, respectively. In all the spectra, N donors were clearly observed, which was evidenced by a triplet splitting due to the hyperfine (HF) interaction between a ^{14}N atom (nuclear spin I = 1, natural abundance = 99.6 %) and a donor electron spin. In principle, a nuclear spin causes ($2I$+1)-fold splitting, giving us a clear identification of the dopant atom. N donors showed the same signal intensities in all the samples, naturally because they were incorporated with the same density.

After implantation [Fig. 1(a)], two types of point defects were observed, as indicated by arrows in the figure. The amount of these defects decreased with higher implantation temperature, which is in line with a general expectation.

After 1650°C annealing [Fig. 1(b)], however, these point defects were completely annihilated, and the post-anneal samples were stabilized to a similar state independent of the implantation temperatures. All the samples exhibited a new EPR signal "P" (indicated by arrows). We measured the magnetic-field angular dependence of the observed signals and determined their spin-Hamiltonian parameters, as shown in Table I. Our N donors are consistent with N at k sites reported in the literature[4]. On the other hand, "P" signal has not been reported in any literatures, and thus we speculate that this signal originates from P donors in 4*H*-SiC. So far, P donors have been observed only in 6*H*-SiC[2,4], in which a doublet splitting due to ^{31}P (I=1/2, natural abundance = 100 %) gave us a clear evidence for P donors. Our new signal did not show such a splitting. However, N donors at h sites also show no appreciable HF

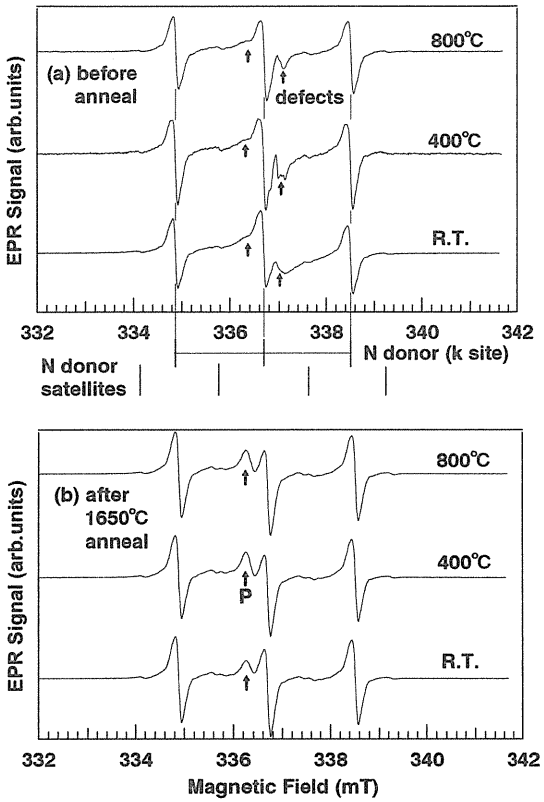

Fig. 1 EPR spectra of P-implanted 4*H*-SiC measured for $\mathbb{B}$ (magnetic field) ∥ c, 60 K, microwave of 9.452 GHz and 0.02 mW. Implantations were carried out along [11$\bar{2}$0] direction. The N donor satellites originate from forbidden lines and HF satellites of the N donor signal.

Table I. Spin-Hamiltonian parameters. $g_{\parallel}$ and $g_{\perp}$ are principal values of the g tensor, A_{iso} is a isotropic HF splitting constant, ΔE is an ionization energy for N or P donors at k or h sites in 4*H*-SiC.

Signal	$g_{\parallel}$	$g_{\perp}$	A_{iso} (mT)	ΔE (meV)
present				
N	2.0042	2.0013	1.82	92
P	2.0063	2.0010	≤0.2	53(h), 93(k)
Ref. 4				
N(k)	2.0043	2.0013	1.82	92
N(h)	2.0055	2.0010	0.10	60

splitting, because of too small splitting width (see A_{iso} in Table I). In SiC, donors at *h* sites show smaller ionization energy (see Table I) and less localization of a donor electron on the dopant atom, resulting in very small HF splitting constants[4]. In future, we will try to measure ENDOR (electron nuclear double resonance) of "P" signal, which enables us to detect the unresolved HF splitting of ^{31}P. Then we will reach to a final conclusion.

3.2 P donor in SiC – potential application to quantum computing

Basically, a donor has an unpaired electron and an electron spin (*S*) of 1/2. This simple spin system has potential as a good quantum bit (qubit) for the quantum computer[3]. Thus far, P donors in Si have been intensively studied for this application, because they were easily produced in Si microstructures and their properties were already well known. However, P donors in Si showed a short coherence time of the electron spin precession, making it difficult to carry out a practical computation. We here show that P donors in SiC have much longer coherence time than those in Si at high temperatures, and thus they become a good candidate for qubits in the solid-state quantum computers.

Figure 2 shows spin-lattice relaxation times (T_1) of N and P donors in 6*H*-SiC, measured by the 3-pulse inversion recovery sequence of pulsed EPR[3]. The P-doped sample was created by P-ion implantation in TIARA[2]. Also shown in the figure are T_1 data for P donors in Si reported previously[5]. Obviously, T_1 values are much longer in SiC than in Si at temperatures higher than 40 K. The computation time of electron-spin-based quantum computers is limited to T_1 and T_M (phase memory time)[3]. For a practical application, the computation time should be at least longer than 100 μsec. This border line can be easily cleared using donors in SiC. Also we measured their T_M by the 2-pulse echo sequence of pulsed EPR. The temperature dependence of T_M was more complicated and depended on samples, however, 100-μsec border line could be also cleared at $T \leq 50$ K[3]. These observations suggest a novel potential of SiC.

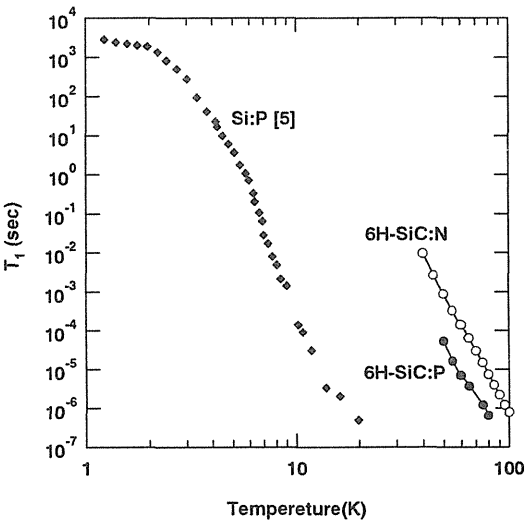

Fig. 2. T_1 (spin-lattice relaxation time) of donor electron spins in Si and SiC.

References

1) Y. Negoro, N. Miyamoto, T. Kimoto, H. Matsunami, Mater. Sci. Forum 389-393 (2002) 783; M. Laube, F. Schmid, G. Pensl, G. Wagner, Mater. Sci. Forum 389-393 (2002) 791.

2) J. Isoya, T. Ohshima, A. Ohi, N. Morishita, H. Itoh, Nuclear Instruments and Methods in Phys. Res. B 206 (2003) 965.

3) J. Isoya, T. Ohshima, N. Morishita, T. Kamiya, H. Itoh, S. Yamasaki, Physica B 340-342 (2003) 903.

4) S. Greulich-Weber, Phys. Stat. Sol. (b) 210 (1998) 415.

5) T. G. Castner, Phys. Rev. 155 (1967) 816; G. Feher, E. A. Gere, Phys. Rev. 114 (1959) 1245.

5.11 Identification of Ion-implantation-induced Defects with the Use of Hydrogen-doped Si Crystals

M. Suezawa,* A. Kawasuso** and M. Maekawa**
Institute for Materials Research, Tohoku University*
Department of Materials Development, JAERI/Takasaki**

1. Introduction

Hydrogen is useful to identify defects from the detection of complexes of hydrogen and point defects in silicon crystals with the measurement of optical absorption spectrum[1, 2]. Vibrational fre-quencies of hydrogen atoms included in those complexes are very high because of its light mass, and the line widths are very small. Hence the sensitivity of detection with optical absorption method is high.

Ion implantation method plays a crucial role for device fabrication process. Implantation-induced damages, however, are not well understood.

As reported last year, we studied defects generated by carbon-implantation of hydrogen-doped Si crystals. We did not find any new peaks. In this year, we studied annealing behavior of those specimens, expecting generation of new complexes due to reactions among hydrogen, carbon and implantation-induced defects. After annealing at 150°C, we observed a new peak at about 1260 cm^{-1}. The intensity of this peak was constant even after annealing at 450°C. Probably this peak is not due to hydrogen since the vibrational frequency is too low and thermal stability is too high.

As a subsidiary study, we performed electron-irradiation of hydrogen-doped p-type Si crystals.

2. Experimental

Specimens were prepared from a boron- or gallium-doped floating-zone grown Si crystal. The concentrations B and Ga were $2.3x10^{15}$, and $5.0x10^{15}$ cm^{-3}, respectively. After mechanical shaping and chemical polishing, they were doped with hydrogen. Hydrogen doping was performed by annealing specimens in hydrogen gas at 1300°C for 1 h followed by quenching in water. Hydrogen atoms form molecules (H_2) in Si crystals at room temperature. H_2 concentration is around $1x10^{16}$ cm^{-3} [3]. Then, specimens were irradiated with 3-MV electrons at room temperature.. Irradiation doses were between $2x10^{16}$ and $4x10^{17}$ cm^{-2}. We measured optical absorption spectra of those specimens with a Fourier transform infrared spectrometer at about 5 K with resolution of 0.25 cm^{-1}.

3. Results and discussion

In the case of boron-doped specimens, the intensity of 1905-cm^{-1} peak, which is due to BH pairs, increased with the increase of electron dose. On the other hand, the intensity of 2171-cm^{-1} peak, which is due to GaH pairs, does not increase. These results clearly shows that the increase of BH pairs is due to migration of B to hydrogen molecule and not due to diffusion of hydrogen molecules to B atoms since if the latter is the case, the intensity of GaH pairs should also increase.

Why does diffusion of boron atom occur? It is due to interaction between B and self-interstitials which are generated by electron-irradiation. A self-interstitial kicks out B from substitutional site to interstitial site, and interstitial B diffuses. Ga atoms also interact with self-interstitials but an interstitial Ga does not diffuse at room temperature.

As is well-known[4], solar cells fabricated from B-doped CZ. Si crystal degrade. It is due to formation of pairs of interstitial B and oxygen. If we dope hydrogen to B-doped CZ. Si crystal, hydrogen effectively trap B atoms as shown above. Hence, the degradation of solar cell is probably diminished.

Summary

To study properties of implantation-induced defects, we performed optical absorption measurement after annealing of carbon-implanted Si crystals. We have not been successful in detection of optical absorption peaks due to complexes of hydrogen and simple point defects, such as vacancies. In subsidiary experiment, we found formation of BH pairs, but not GaH pairs.

References

1) M. Suezawa, Physical Review B 63 (2000) 035201-1 ~ -7.

2) M. Suezawa, Physical Review B 63 (2000) 035203-1 ~ -6.

3) R. E. Pritchard, M. J. Ashwin, J. H. Tucker, R. C. Newman, E. C. Lightowlers, M. J. Binns, S. A. McQuaid and R. Falster, Physical Review B 56 (1997) 13118- 13125.

4) S. W. Glunz, S. Rein, W. Warta, J. Knobloch and W. Wettling, Proc. of the 2nd World Conf. on Photovoltaic Energy Conversion, 1998, p. 1343.

5.12 Fabrication and Evaluation of Micrometer-scale Optical Elements using Three-dimensional Irradiation Effects Localized in Micro and Nanometer-scale Regions

H. Nishikawa*, K. Fukagawa*, T. Yanagi**, T. Nakamura**, Y. Ohki**,
E. Watanabe***, M. Oikawa****, K. Arakawa****, T. Kamiya*****
Department of Electrical Engineering, Shibaura Institute of Technology *
Department of Electrical Engineering and Bioscience, Waseda University **
Department of Electrical Engineering, Tokyo Metropolitan University ***
Advanced Radiation Technology Center, JAERI****
Department of Material Development, JAERI*****

1. Introduction

Irradiation on silica glass with high-energy ions can induce micro- or nano-scale structure changes. Our research project focuses on both the basic mechanisms involving microbeam irradiation effects in silica glass and applications of this phenomenon to the fabrication of micrometer-sized modified silica surface with increased refractive index with a relatively high aspect ratio.

The purpose of this study is to investigate the micro- and nano-scale irradiation effects in silica glass induced by ion microbeam. We also discuss possible application of this phenomenon for the micro-meter scale optical elements on photonics materials such as silica glass.

2. Experimental Procedures

Ion microbeam irradiation was performed by using a microbeam line at a 3MV single-ended or tandem accellerator in TIARA facility in JAERI Takasaki.

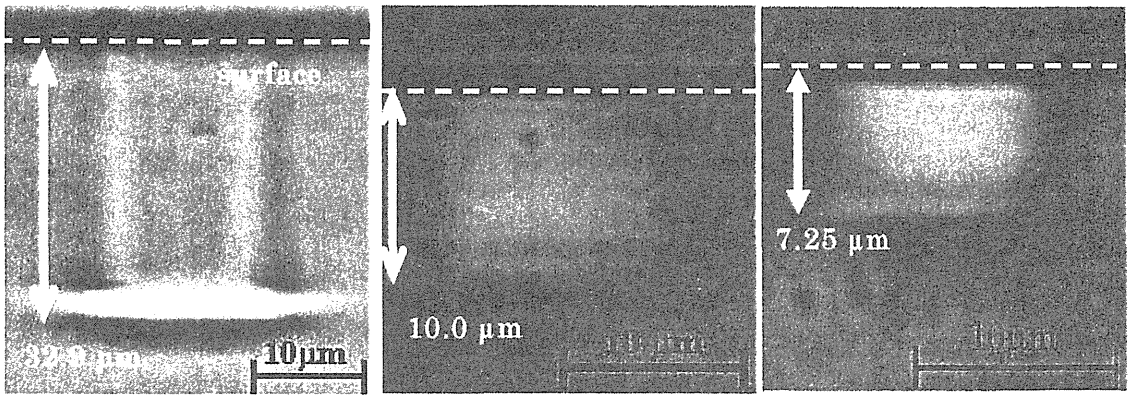

(a) H^+ (b) O^{4+} (c) Si^{5+}

Fig.1 Transmission optical microscope images observed on the side surfaces of silica glass scanned over the width of 10 μm. (a) H^+ (1.7 MeV, 1×10^{17} ions/cm^2), (b) O^{4+} (15 MeV, 1×10^{14} ions/cm^2), and (c) Si^{5+} (18 MeV, 1×10^{14} ions/cm^2)

Focused ion microbeam of H^+ (1.7 MeV), Si^{5+} (18 MeV), or O^{4+} (15 MeV) with diameter of 1 μm was scanned over the surfaces of synthetic silica glass (Nippon Quartz, Co, Ltd., [OH]:1300 ppm) in dimensions of $3\times3\times10$ mm^3 with mirror-polished front and side surfaces, up to a fluence of 1×10^{17} ions/cm^2.

Microbeam irradiation effects on silica glass were studied by optical microscopy of refractive index changed region on the side surfaces of silica glass, and by μ-photoluminescence (PL) and atomic force microscopy (AFM) on the side surface.

3. Results and discussion

Shown in Fig.1 are the transmission optical microscope images on the side surface of silica irradiated with different ion species. Irradiation effects induced by ion microbeam are visualized by the refractive index change shown as bright regions in Fig.1. Depending on the acceleration energy and ion species, the depth of irradiation effects on silica glass varies from 7 μm to 33 μm. The depth distribution of the irradiation effects can be controlled by the energy of ions, based on the predicted ion ranges from SRIM simulation.

Figure 2 shows the PL spectra (a) and PL intensity (b) as a function of the fluence of 18 MeV Si^{5+} ions obtained under excitation at 488 nm and at room temperature. The two PL centers were induced by energy deposition processes to silica glass due to electronic and nuclear stopping powers. One of the PL centers associated with the 650 nm band is ascribed to the nonbridging oxygen hole center (NBOHC, ≡Si-O ・)[1]. The PL intensity begins to increase at the fluence of 10^{13} ions/cm^2, and it saturates at the fluence of 10^{15} ions/cm^2. The micrometer-scale distribution of irradiation effects is revealed by means of the three dimensional mapping of the PL intensity on the microbeam-scanned area[2].

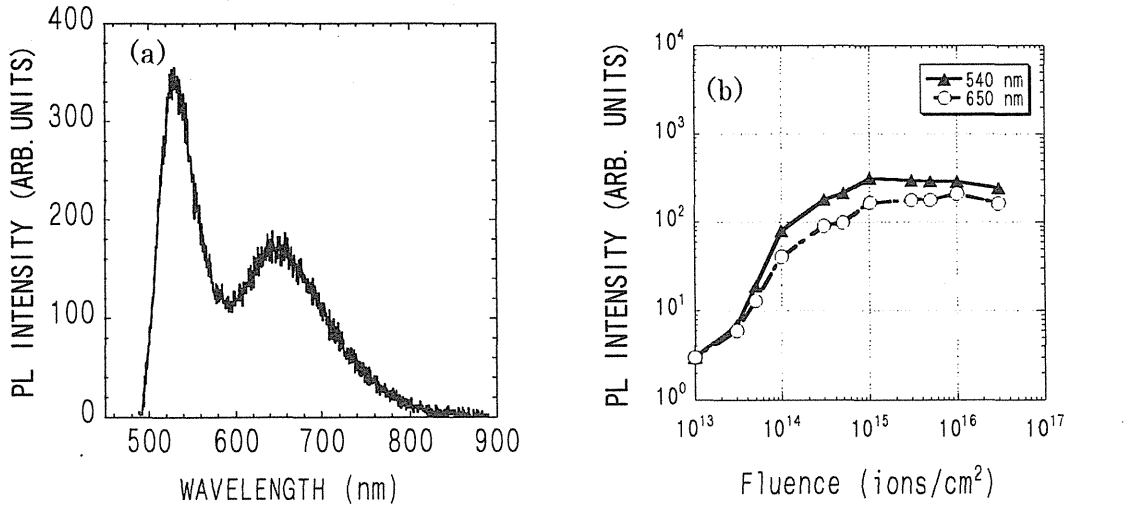

Fig.2 (a) Photoluminescence spectrum observed for silica glass irradiated by ion microbeam (Si^{5+}, 18MeV, fluence: 3×10^{16} ions/cm^2) and (b) the intensity of PL bands as a function of the fluence.

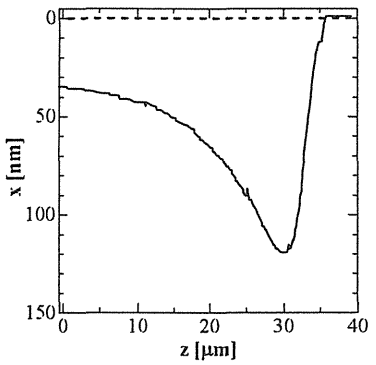

(a) H^+ (1.7 MeV, 1×10^{17} ions/cm^2)

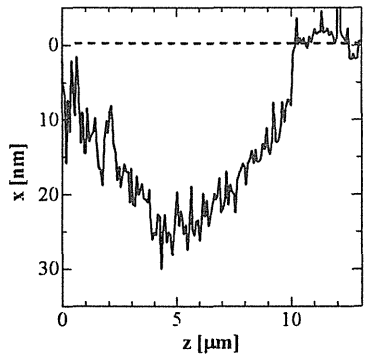

(b) O^{4+} (15 MeV, 1×10^{14} ions/cm^2)

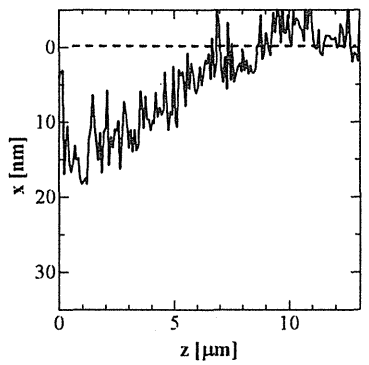

(c) Si^{5+} (18 MeV, 1×10^{14} ions/cm^2)

Fig. 3 Side surface profiles measured by AFM, which is perpendicular to microbeam-scanned surface.

Figures 3 show the deformed surface profiles due to internal compaction of silica glass, which was measured on the side surface by AFM. Depending on irradiation conditions, the depth of the grooves ranges from a few nm to more than 100 nm. The side surface profile reflects the distribution of energy deposition due to the electronic and nuclear processes. Similar surface deformation was also observed on the microbeam-scanned front surface of silica glass [3].

Since the spatial distribution of radiation effects such as the compaction and resulting refractive index changes greatly differ between the 1.7 MeV H^+, 15 MeV O^{4+}, and 18 MeV Si^{5+} as shown in Figs. 1 and 3, the proper choice of irradiation condition is important to apply the microbeam irradiation effects to the fabrication of micro-meter scale optical elements, depending on the forms of target materials such as optical fibers and planar circuits.

References

1) H. Nishikawa et al., Transactions of the Materials Research Society of Japan 29, (2004), 603-606
2) T. Souno et al., Nucl. Instrum. Meth. B 210, (2003), 277-280
3) M. Hattori et al., Nucl. Instrum. Meth. B 210, (2003), 272-276

6. Nuclear Science and RI Production

This is a blank page.

6.1 Excitation Functions of the $^{nat}Br(p,x)^{73,75}Se$ Nuclear Reactions

B. Fateh*, N. S. Ishioka*, S. Watanabe*, T. Sekine** and T. Kume*

Department of Ion-beam-applied Biology, JAERI*
Department of Irradiation Technology and Public Relation, RADA**

1. Introduction

^{73}Se ($T_{1/2}$= 7.1 h) is a positron emitter (β^+=65%, EC=35%) and utilized as a sulphur analogue radiotracer for application in positron emission tomography (PET) [1,2]. ^{75}Se ($T_{1/2}$=120 d) decays via electron capture (EC=100%) and has been the most widely used radioisotope of selenium for radiotracer studies. However, because of its long physical half-life and decay characteristics, clinical application of ^{75}Se labeled compounds is severely limited [3].

No experimental data for the selenium forming channels of $^{nat}Br(p,x)^{73,75}Se$ could be found in the literature except for the experimental cross-section data reported by Faßbender *et al.*[2]. In this paper, the excitation functions of $^{nat}Br(p,x)^{73,75}Se$ reactions have been measured to verify previously reported data [2] up to 65 MeV.

2. Materials and methods

The excitation functions were measured by the activation method using the stacked foil technique. Stacks consisted of the sandwiched NaBr pellets, each followed by monitor foils of 0.00324 g/cm^2 Al (for >40 MeV) and 0.00892 g/cm^2 Cu (for <40 MeV). Figure 1 shows the scheme of NaBr stack. The anhydrous NaBr powder was pressed into the pellets at 600 kg/cm^2 with a thickness of 0.7-0.8 mm and 1 cm diameter. Each stack was covered by 10μm Al foil. Irradiations were performed at proton energies of 42.9 ± 0.43 and 63.5 ± 0.63 MeV, to avoid the possible error in the energy along a thick stack, for 75-90 minutes. Figure 2 shows the irradiation system.

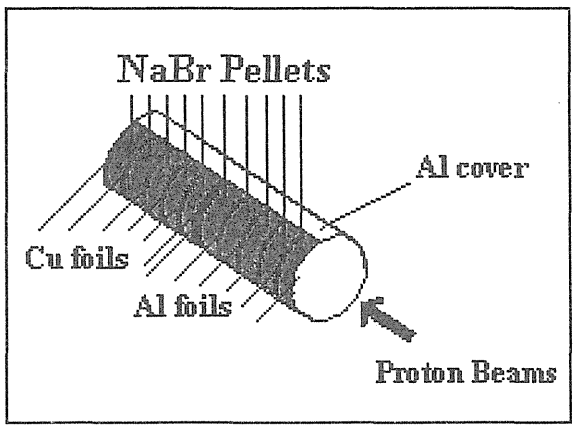

Fig.1 Stack consisted of NaBr pellets and monitor foils

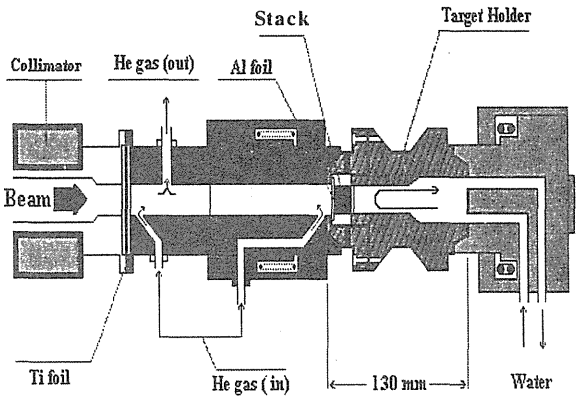

Fig. 2 Irradiation system

The energy degradations along the stacks were calculated according to Ziegler's formula [4] using the SRIM-2000 code. The beam current was monitored by a Faraday-cup and determined via the monitor reactions of $^{27}Al(p,3pn)$ ^{24}Na and $^{nat}Cu(p,xn)^{62}Zn$. The produced activity in the foils and the pellets were measured with HPGe-Spectrometer without chemical separation.

3. Results and discussion

Figure 3 shows the excitation function of the $^{nat}Br(p,x)^{73}Se$ obtained in the present work together with the previously reported one [2] and the theoretical (Alice-91) cross section data. The figure shows that:

Our data shows slightly lower cross section values compare to Faßbender *et al.* data and the Alice-91 code, but considering the systematic errors, they are in good agreement.

Figure 4 presents the experimental and theoretical excitation functions for the $^{nat}Br(p,x)^{75}Se$ nuclear reaction. Our results show considerable discrepancies in magnitude of cross section, having lower values in comparison with Faßbender *et al.* results [2]. We suppose the following sources of errors in their work:

a) According to their original paper, ^{75}Se activity has been measured by considering of 136.0 keV gamma ray energy peak in each pellet. ^{79}Kr has the same gamma energy of 136.0 kev and can be produced via $^{nat}Br(p,xn)$ nuclear reaction simultaneously, especially in lower proton energies (up to 50 MeV). In monitoring it is necessary to wait until the ^{79}Kr totally decays to its stable daughter. Therefore, the excitation function of the $^{nat}Br(p,x)^{75}Se$ process must be measured precisely after 2-3 weeks. Such a several weeks decay time has not been considered by Faßbender *et al.* Therefore, a part of ^{75}Se activities, which has been measured by them, it is belong to ^{79}Kr.

b) ^{75}Se also can be produced indirectly by the decay of ^{75}Br ($T_{1/2}$= 1.6 h), which formed by $^{nat}Br(p,pxn)$ reaction. For measuring the excitation function of $^{nat}Br(p,x)^{75}Se$ reaction, the activity of indirectly produced ^{75}Se must be considered and subtracted from the total ^{75}Se activities. The amount of indirectly produced ^{75}Se must be considered and calculated by measuring the activity of ^{75}Br in each pellet and applying the decay equations.

Acknowledgment:

The authors wish to express appreciation to Japan Society for the Promotion of Science (JSPS) for supporting this research activity.

References

1) Blessing G., Lavi N. and Qaim S. M., Int. J. Appl. Radiat. Isot., **43** (1992), 455-461.
2) Faßbender M., De Villiers D., Nortier M. and van der Walt N., Appl. Radiat. Isot., **54** (2001), 905-913.
3) Plenevaux A., Guillaume M., Brihaye C., Lemaire C. and Cantineau R., Int. J. Appl. Radiat. Isot., **41** (1990), 829-838.
4) Ziegler J. F., Biersack J. P. and Littmark L., The stopping and range of ions in solids, Volume 1 of the stopping and ranges of ions in matter, Pergamon Press (1985).

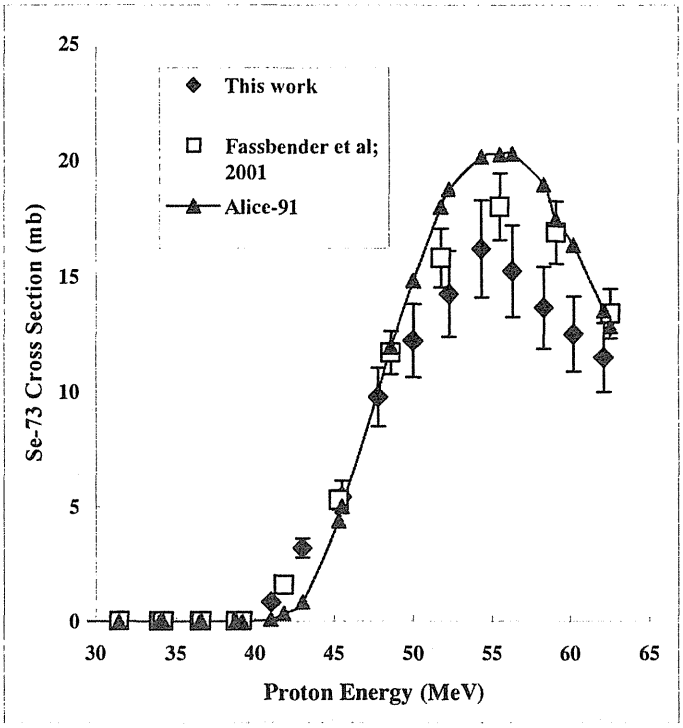

Fig.3 Experimental excitation functions for the formation of ^{73}Se via the $^{nat}Br(p,x)^{73}Se$ reaction and theoretical (Alice-91) calculations

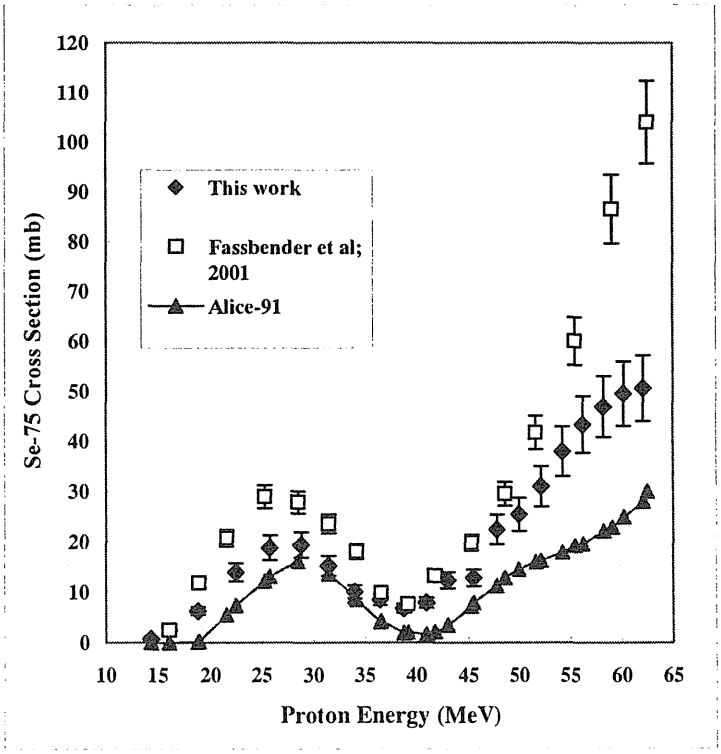

Fig.4 Experimental excitation functions for the formation of ^{75}Se via the $^{nat}Br(p,x)^{75}Se$ reaction and theoretical (Alice-91) calculations

6.2 Four Elemental Profiles of Time-activity Curves Obtained from PETIS Experiments

S. Fujimaki[*,**], K. Sakamoto[**], N. S. Ishioka[**], S. Matsuhashi[**] and A. Miyashita[*]

Theoretical Analysis Group for Radiation Application, JAERI[*]

Department of Ion-beam-applied Biology, JAERI[**]

1. Introduction

Today, The Positron Emitting Tracer Imaging System (PETIS) is getting popular as the unique tool for capturing the movie of radioactive tracer fed in a plant body. However, the obtained images have not been sufficiently analyzed. It has been only "visualization" of the moving tracer, but not analysis of the "dynamics".

Our conclusive purpose is to establish a method of mathematical analysis which leads to quantitative understanding of physiological conditions. The concrete subject to be analyzed is "time-activity curve (TAC)", a time course of activity within a selected region of interest (ROI) on a moving image. The TACs should have great information about the dynamics of tracer, at the same time, and the structural conditions which determine the dynamics.

A plant vascular bundle consists of xylem vessels and sieve tubes as flow paths, and of surrounding tissues absorbing various substances from them. How a TAC reflects natures of the flow path and the surrounding structure? To answer this question, we started this present study.

We prepared two models for the structure of a vascular bundle. Model A has a path with impermeable wall, and the other model B with tracer-absorbing wall. TACs would also depend on the manner of feeding of the tracer. We subjected the models to PETIS with (1) pulse feeding or (2) constant feeding of tracer. The TACs obtained in these four combined cases, A-1, A-2, B-1 and B-2, were compared.

2. Experimental procedure

2.1 Models

A plastic string two millimeters in diameter and a plastic tube two millimeters in internal diameter were set on the centers of acrylic pipes. Two percent agarose gel (LO3, TAKARA, Japan) was melt and poured in the pipes around the string or tube. The string was pulled out after the gel solidified to make straight path throughout the gel. The completed models were illustrated in Figure 1.

Fig. 1 Models with different structure surrounding the flow paths.

The pale colored parts indicate agarose gel.
(A) Impermeable wall of plastic.
(B) Tracer-absorbing wall of agarose gel.

This agarose gel is widely used for electrophoresis of DNA, a macromolecule. The tracer ions can enter the gel wall easily off from the flow path by simple diffusion. In addition, the gel layer completely captures the

positrons emitted from tracer and prevents loss of detection by PETIS.

2.2 Production of tracer

$^{13}NH_4^+$ was produced in the $^{16}O(p, \alpha)^{13}N$ reaction by bombarding water with a 20 MeV proton beam from the TIARA AVF cyclotron. From 42 to 89 MBq of $^{13}NH_4^+$ in water was used for the experiments.

2.3 PETIS experiments

The models were set in the view of the PETIS, and were connected to peristaltic pump to flow tracer solution or water at a constant rate (56 – 91 μl min^{-1}). After the PETIS measurement started, the tracer solution (3.8 – 5.9 MBq ml^{-1} at the starting time) was loaded onto the top of the models for 30 seconds (case A-1) or for 20 seconds (case B-1), or continuously (case A-2 and B-2). For the pulse-feeding cases (A-1 and B-1), pure water was loaded to follow the tracer.

The PETIS measurement was carried out by refreshing frames of image by every 10 seconds.

2.4 Data processing

A computer program we specially made was used for extracting the TACs in the selected ROIs from the obtained image data. The ROIs were placed from upstream to downstream at even intervals.

3. Results and Discussion

Figure 2 shows the TACs from the four cases. In the first case A-1, impermeable wall / pulse feeding, the TACs showed lower and broader peaks in downstream ROIs (Fig. 2a). The group velocity of tracer was approximately 2.4 cm min^{-1} and the tip speed was approximately 5.1 cm min^{-1}, about two times of the former. This "dispersion" would be caused by laminar flow in the tube. We estimated the laminar flow condition was satisfied in this experiment (data not shown).

In the case A-2, impermeable wall / constant feeding, the TACs reached a constant level (Fig. 2b).

In the case B-1, absorbing wall / pulse feeding, the TACs showed combination of a peak and an almost steady state (Fig. 2c). They mostly reproduced those in experiments with plants fed pulsed $^{11}CO_2$ gas (Fig. 3a). The ^{11}C-labeled assimilates produced by photosynthesis would be transported through sieve tubes and partially taken up by surrounding stem tissue.

In the last case B-2, absorbing wall / constant feeding, the beginnings of TACs showed short but steep rising, and then continuous linear increase followed (Fig. 2d). The former profile indicates that concentration of tracer in the flow path rapidly reached a certain level at each ROI, like the case A-2. The latter one indicates that tracer entered the gel wall at a constant rate depending on the concentration in the flow path. Similar TACs have often been obtained in PETIS experiments with plants fed tracers from hydroponic culture (Fig. 3b). The beginning part is very shorter than the subsequent linear part in the TACs. This profile demonstrates that the flow speed in the xylem vessels was very high, and unloading of the tracer from the vessels into the surrounding stem tissue continued vigorously and constantly.

In this present study, qualitative interpretation of TAC has been done through classifying the TACs. If only partially, nature or function of plant tissues now can be realized from TACs obtained from PETIS experiments as described above. We started developing mathematical analysis methods to make the description quantitative.

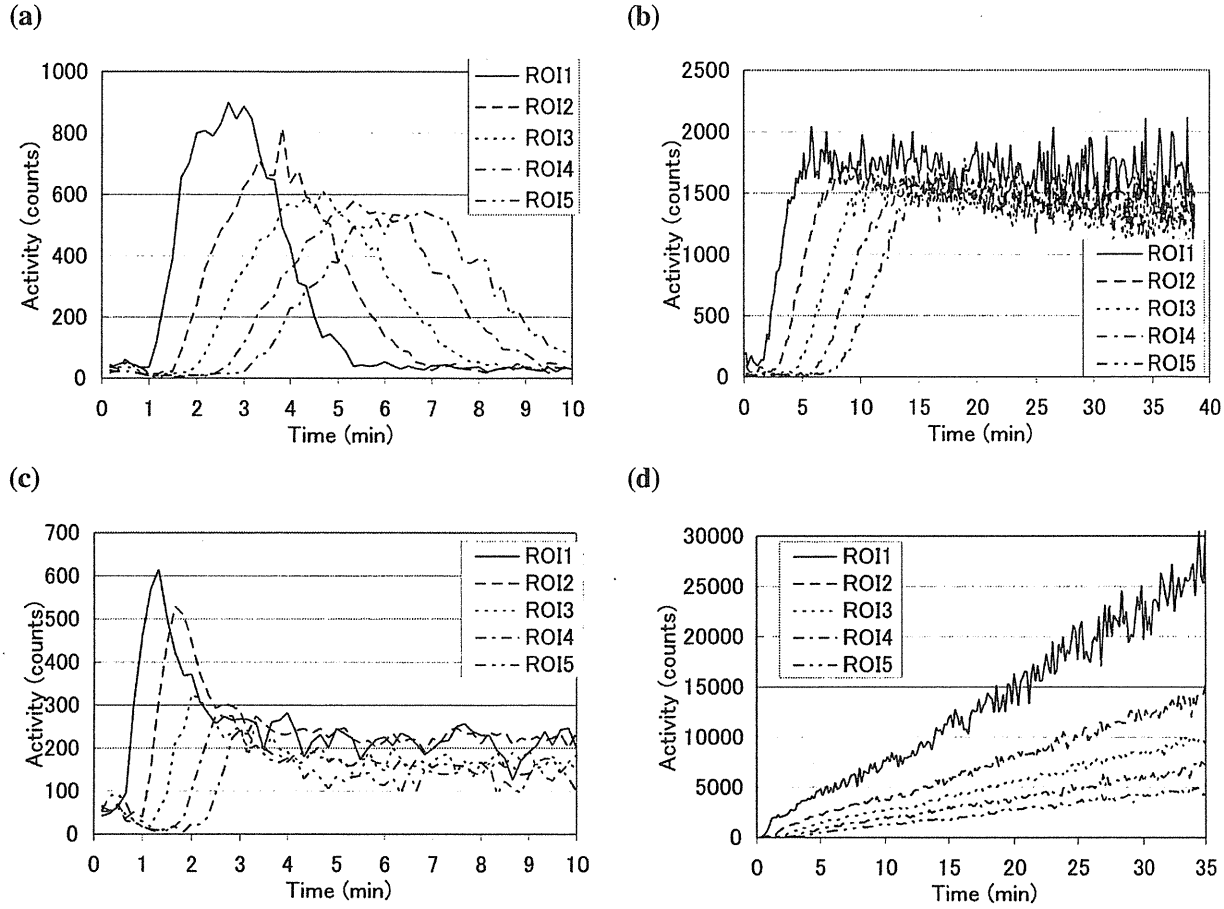

Fig. 2 TACs obtained from four models. (a) case A-1, impermeable wall / pulse feeding; (b) case A-2, impermeable wall / constant feeding; (c) case B-1, absorbing wall / pulse feeding; (d) case B-2, absorbing wall / constant feeding.

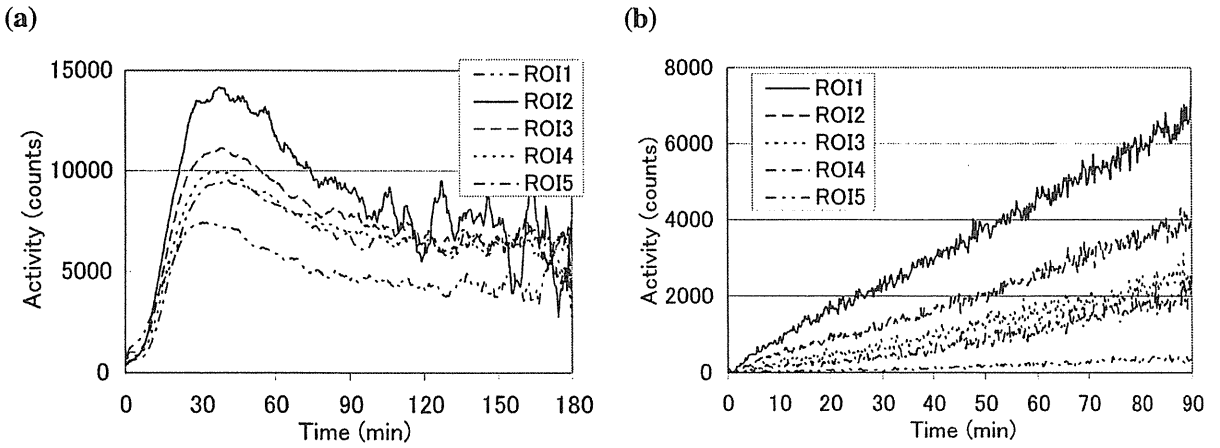

Fig. 3 TACs obtained from plants. The ROIs were placed towards downstream. (a) Transportation of photoassimilates in the stem of a broad bean plant fed pulsed $^{11}CO_2$ gas onto its leaf.
(b) Transportation of a tracer in the stem of a hemp plant from hydroponic culture.

6.3 Measurements of Deuteron-induced Activation Cross Sections for IFMIF Accelerator Structural Materials in 22-40 MeV Region

M. Nakao*, J. Hori*, K. Ochiai*, S. Sato*, M. Yamauchi*, N. S. Ishioka**, T. Nishitani*
Department of Fusion Engineering Research, JAERI*
Department of Ion-beam-applied Biology, JAERI**

1. Introduction

The IFMIF is an accelerator-based D-Li neutron source designed to produce an intense neutron field for testing fusion reactor candidate materials. In the design of IFMIF, long-term operation with the total facility availability is conceived to be at least 70 %. However, activation of the structural materials along the beam transport lines by deuteron beam loss limits maintenance and makes long-term operation difficult. To estimate the activation, activation cross sections are necessary. But, there is few deuteron-induced activation cross section data. So measurements of this data were performed for aluminum, copper and tungsten in this work. Aluminum is the main component of the beam duct and electrode. Copper is used in the cavity walls, electrodes and magnetic conductors. Tungsten is candidate material for beam slits and coating to protect the beam facing components.

2. Experiment and Data processing

Activation cross sections were measured by using a stacked-foil technique. The stacked-foils consisted of natural composition aluminum, copper and tungsten. The stacked-foils were wrapped in aluminum sheet with a thickness of 10 μm and irradiated with deuteron beam accelerated by the AVF cyclotron at TIARA. After cooling, the decayed gamma rays emitted from the irradiated foils were measured by a calibrated Ge detector and the induced activities were obtained for ^{24}Na, ^{27}Mg, ^{61,64}Cu. ^{62,63,65}Zn, $^{181\text{-}184,186}$Re, ^{187}W.

The energy degradation along the stack and the effective deuteron energy at the middle position of each foil were estimated by IRACM code[1]. The number of incident deuteron on each stacked-foil was determined from ^{65}Zn activities observed by the ^{nat}Cu(d,x)^{65}Zn reaction cross section data reported by Takács et al.[2]. The cross sections for the twelve radioactive nuclei were derived from the induced activities and the number of incident deuterons.

3. Results and Conclusion

The present cross sections with other experimental ones and the data in ACSELAM library for ^{27}Mg and ^{24}Na are shown in Figures 1 and 2. For ^{27}Mg, the data in ACSELAM were smaller than the present data by a factor of 1.3-2.0. For ^{24}Na, the present data were in agreement with other experimental one within experimental error. On the other hand the data in ACSELAM were about 1 order lower than the experimental ones.

Figures 3-6 show the present data for the ^{nat}Cu(d,x)^{61}Cu($T_{1/2}$=3.33h), ^{64}Cu($T_{1/2}$=12.7h), ^{62}Zn($T_{1/2}$=9.19h) and ^{63}Zn($T_{1/2}$=38m) reactions with other experimental data and the data in ACSELAM library. The data reported by Flumer and ACSELAM resembled the present data in shape. In the case of ^{61}Cu and ^{62}Zn, these data become higher than the present data by a factor of 2-4. In the case of ^{64}Cu and ^{63}Zn, these

data and the present data were in agreement within 40 %.

Figures 7-12 show the present data for the $^{nat}W(d,x)^{181}Re(T_{1/2}=19.9h)$, $^{182g}Re(T_{1/2}=2.67d)$, $^{182m}Re(T_{1/2}=12.7h)$, $^{183}Re(T_{1/2}=70d)$, $^{184g}Re(T_{1/2}=38d)$, $^{184m}Re(T_{1/2}=169d)$, $^{186}Re(T_{1/2}=3.78d)$ and $^{187}W(T_{1/2}=23.72h)$ reactions with other experimental data and the data in ACSELAM library. In the energy region of 22-40MeV, there is no experimental data. For ^{181}Re, $^{182m+g}Re$ and ^{183}Re, the present data and the data in ACSELAM were about same shapes and in agreement within 30 %. For $^{184m+g}Re$, the present data were different from ACSELAM in shape and became higher than ACSELAM by a factor of 1.5-7. For ^{186}Re, the present data showed decreasing tendency above 24 MeV and were 3 times as low as values in ACSELAM at the maximum though the experimental one were close to ACSELAM below 10 MeV. For ^{187}W, the present data and other experimental data were different from the data in ACSELAM in shape. The reason of this difference is that ^{187}W could be produced by not only $^{186}W(d,p)$ but also $^{186}W(n, \gamma)$ reaction which was occurred by secondary low-energy neutron. The measurements of activation cross section for other accelerator structural materials (Ta, Fe, Ni) will be performed next year.

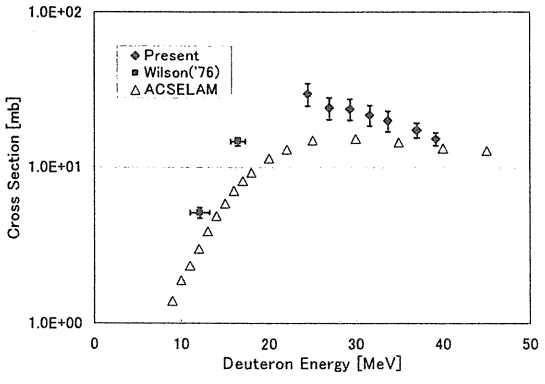

Fig. 1 Cross sections for the $^{27}Al(d,2p)^{27}Mg$

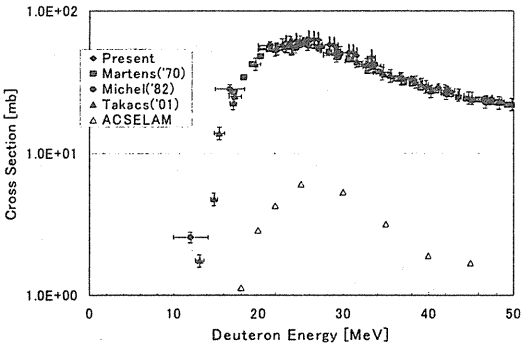

Fig. 2 Cross sections for the $^{27}Al(d,x)^{24}Na$

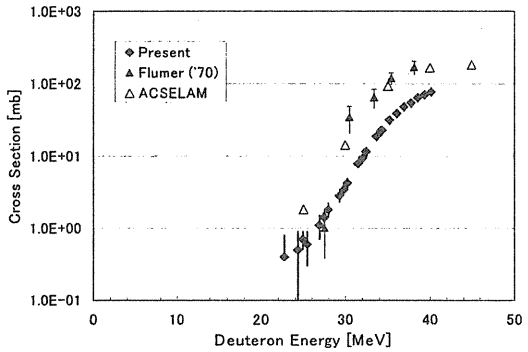

Fig. 3 Cross sections for the $^{nat}Cu(d,x)^{61}Cu$

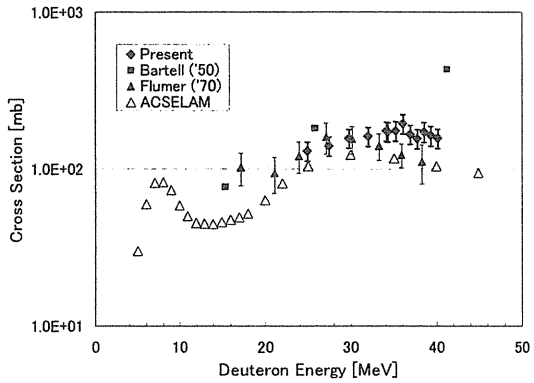

Fig. 4 Cross sections for the $^{nat}Cu(d,x)^{64}Cu$

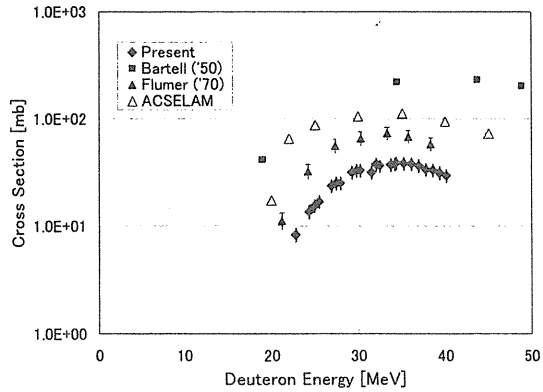

Fig.5 Cross sections for the $^{nat}Cu(d,x)^{62}Zn$

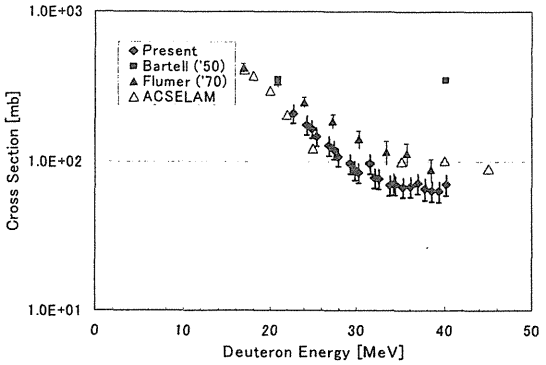

Fig.6 Cross sections for the $^{nat}Cu(d,x)^{63}Zn$

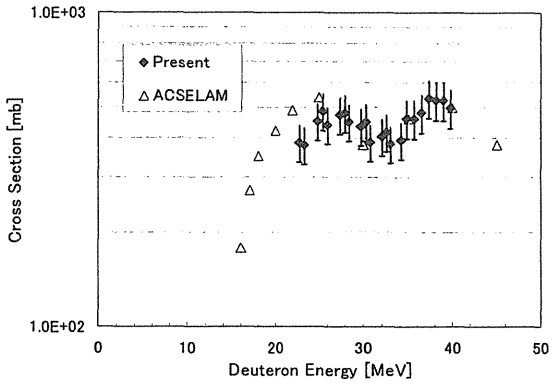

Fig.7 Cross sections for the $^{nat}W(d,x)^{181}Re$

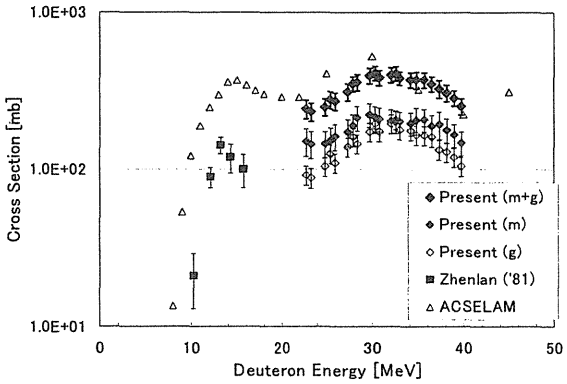

Fig.8 Cross sections for the $^{nat}W(d,x)^{182}Re$.

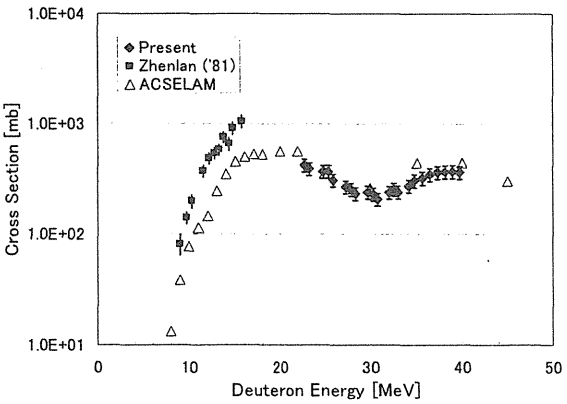

Fig.9 Cross sections for the $^{nat}W(d,x)^{183}Re$

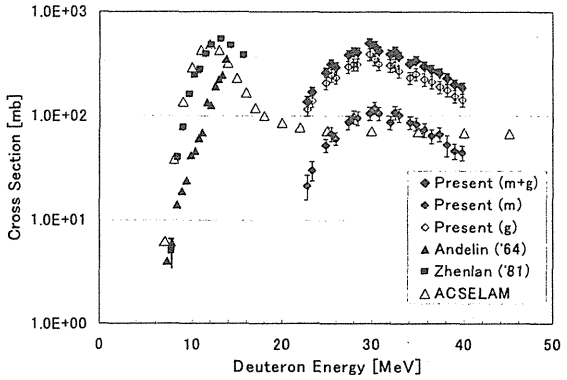

Fig.10 Cross sections for the $^{nat}W(d,x)^{184}Re$

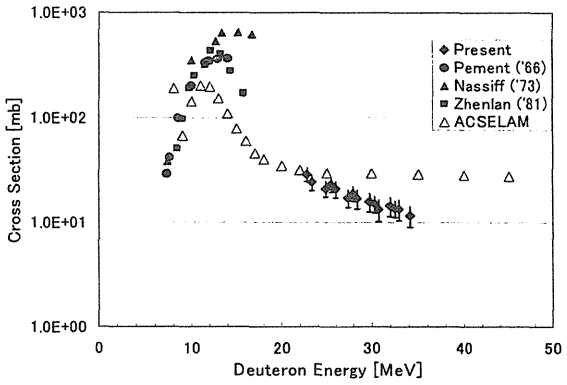

Fig.11 Cross sections for the $^{nat}W(d,x)^{186}Re$

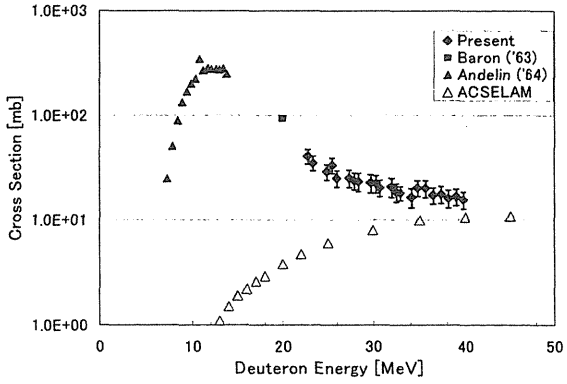

Fig.12 Cross sections for the $^{nat}W(d,x)^{187}W$

References

1) S. Tanaka, M. Fukuda, K. Nishimura, *et al.*, "IRACM: A Code System to Calculate Induced Radioactivity Produced by Ions and Neutrons," JAERI-Data/Code 97-019 (1997).

2) S. Takács, et al., Nucl. Inst. Meth., B 174, 235-258 (2001).